Optical and near-infrared observations of SN 2011dh - The first 100 days.

M. Ergon[1], J. Sollerman[1], M. Fraser[2], A. Pastorello[3], S. Taubenberger[4], N. Elias-Rosa[5], M. Bersten[6], A. Jerkstrand[2], S. Benetti[3], M.T. Botticella[7], C. Fransson[1], A. Harutyunyan[8], R. Kotak[2], S. Smartt[2], S. Valenti[3], F. Bufano[9,10], E. Cappellaro[3], M. Fiaschi[3], A. Howell[11], E. Kankare[12], L. Magill[2,13], S. Mattila[12], R. Naves[14], P. Ochner[3], J. Ruiz[15], K. Smith[2], L. Tomasella[3], and M. Turatto[3]

[1] The Oskar Klein Centre, Department of Astronomy, AlbaNova, Stockholm University, 106 91 Stockholm, Sweden
[2] Astrophysics Research Center, School of Mathematics and Physics, Queens University Belfast, Belfast, BT7 1NN, UK
[3] INAF, Osservatorio Astronomico di Padova, vicolo dell'Osservatorio n. 5, 35122 Padua, Italy
[4] Max-Planck-Institut für Astrophysik, Karl-Schwarzschild-Str. 1, D-85741 Garching, Germany
[5] Institut de Ciències de l'Espai (IEEC-CSIC), Facultat de Ciències, Campus UAB, E-08193 Bellaterra, Spain.
[6] Kavli Institute for the Physics and Mathematics of the Universe, Todai Institutes for Advanced Study, University of Tokyo, 5-1-5 Kashiwanoha, Kashiwa, Chiba 277-8583, Japan
[7] INAF-Osservatorio Astronomico di Capodimonte, Salita Moiariello, 16 80131 Napoli, Italy
[8] Fundación Galileo Galilei-INAF, Telescopio Nazionale Galileo, Rambla José Ana Fernández Pérez 7, 38712 Breña Baja, TF - Spain
[9] INAF, Osservatorio Astrofisico di Catania, Via Santa Sofia, I-95123, Catania, Italy
[10] Departamento de Ciencias Fisicas, Universidad Andres Bello, Av. Republica 252, Santiago, Chile
[11] Las Cumbres Observatory Global Telescope Network, 6740 Cortona Dr., Suite 102, Goleta, CA 93117
[12] Tuorla Observatory, Department of Physics and Astronomy, University of Turku, Väisäläntie 20, FI-21500 Piikkiö, Finland
[13] Isaac Newton Group, Apartado 321, E-38700 Santa Cruz de La Palma, Spain
[14] Observatorio Montcabrer, C Jaume Balmes 24, Cabrils, Spain
[15] Observatorio de Cántabria, Ctra. de Rocamundo s/n, Valderredible, Cantabria, Spain

ABSTRACT

We present optical and near-infrared (NIR) photometry and spectroscopy of the Type IIb supernova (SN) 2011dh for the first 100 days. We complement our extensive dataset with SWIFT ultra-violet (UV) and Spitzer mid-infrared (MIR) data to build a UV to MIR bolometric lightcurve using both photometric and spectroscopic data. Hydrodynamical modelling of the SN based on this bolometric lightcurve have been presented in Bersten et al. (2012). We find that the absorption minimum for the hydrogen lines is never seen below ~11000 km s^{-1} but approaches this value as the lines get weaker. This suggests that the interface between the helium core and hydrogen rich envelope is located near this velocity in agreement with the Bersten et al. (2012) He4R270 ejecta model. Spectral modelling of the hydrogen lines using this ejecta model supports the conclusion and we find a hydrogen mass of 0.01-0.04 M$_\odot$ to be consistent with the observed spectral evolution. We estimate that the photosphere reaches the helium core at 5-7 days whereas the helium lines appear between ~10 and ~15 days, close to the photosphere and then move outward in velocity until ~40 days. This suggests that increasing non-thermal excitation due to decreasing optical depth for the γ-rays is driving the early evolution of these lines. The Spitzer 4.5 μm band shows a significant flux excess, which we attribute to CO fundamental band emission although further work using late time data is needed. The distance and in particular the extinction, where we use spectral modelling to put further constraints, is discussed in some detail as well as the sensitivity of the hydrodynamical modelling to errors in these quantities. We also provide and discuss pre- and post-explosion observations of the SN site which shows a reduction by 60-75 percent in flux at the position of the yellow supergiant coincident with SN 2011dh. The V band decline between Jan 20 and Apr 14 2013 is 0.76 mag which is consistent with the remaining flux being emitted by the SN. Hence we find that the star was indeed the progenitor of SN 2011dh as previously suggested by Maund et al. (2011) and which is also consistent with the results from the hydrodynamical modelling.

Key words. supernovae: general — supernovae: individual (SN 2011dh) — galaxies: individual (M51)

1. Introduction

Core-collapse (CC) supernovae (SNe) are caused by the gravitational collapse of the core in massive stars. The diversity of the events that we observe reflects the diversity of the progenitor stars and their surrounding circumstellar media (CSM). In particular, the extent to which the star has lost its hydrogen envelope has a profound impact on the observed properties of the SN. Through the presence or absence of hydrogen lines in their spectra these SNe are classified as Type II or Type I, respectively. The ejecta mass of Type I SNe tends to be smaller and thus the diffusion time shorter and the expansion velocity higher. The designation IIb is used for SNe which show a spectral transition from Type II (with hydrogen) at early times to Type Ib (without hydrogen but with helium) at later times. These SNe are thought to arise from stars that have lost most, but not all, of their hydrogen envelope. The prime example of such a SN is 1993J, where the progenitor star was a yellow (extended) supergiant proposed

to have lost most of its hydrogen envelope through interaction with its blue (compact) companion star (Podsiadlowski et al. 1993; Maund et al. 2004; Stancliffe & Eldridge 2009). As Type IIb SNe are surprisingly common given the brief period single stars spend in the appropriate state, binary stars have been suggested as the main production channel - but the issue remains unsolved. Bright and nearby Type IIb SNe are rare but detection of the progenitor star in archival pre-explosion images and, when the SN has faded, a search for the companion star is feasible. By comparison of the magnitude and colour of the progenitor star to predictions from stellar evolutionary models, basic properties such as the initial mass can be estimated (Smartt et al. 2009). High quality multi-wavelength monitoring of these SNe followed by detailed modelling of the data is crucial to improve our understanding of Type IIb SNe and their progenitor stars. This paper presents the first 100 days of the extensive optical and NIR dataset we have obtained for such a SN, the Type IIb 2011dh. Detailed hydrodynamical modelling of the SN using these data have been presented in Bersten et al. (2012, hereafter B12) and identification and analysis of the plausible progenitor star in Maund et al. (2011, hereafter M11). The remaining data and further modelling will be presented in forthcoming papers.

1.1. Supernova 2011dh

SN 2011dh was discovered by A. Riou on 2011 May 31.893 UT (Griga et al. 2011) in the nearby galaxy M51 at a distance of about 8 Mpc (Sect. 1.2). The latest non-detection reported in the literature is by Palomar Transient Factory (PTF) from May 31.275 UT (Arcavi et al. 2011, hereafter A11). In this paper we adopt May 31.5 UT as the epoch of explosion and the phase of the SN will be expressed relative to this date throughout the paper.

The host galaxy M51, also known as the Whirlpool galaxy, was the first galaxy for which the spiral structure was observed (Rosse 1850) and is frequently observed. Thus it is not surprising that excellent pre-explosion data were available in the Hubble Space Telescope (HST) archive. In M11 we used these data to identify a yellow (extended) supergiant progenitor candidate which, by comparison to stellar evolutionary models, corresponds to a star of 13 ± 3 $M_\odot$ initial mass. A similar analysis by Van Dyk et al. (2011) estimated an initial mass between 17 and 19 $M_\odot$, the difference mainly stemming from the different method used to identify the evolutionary track in the HR-diagram. Recent HST (Van Dyk et al. 2013) and Nordic Optical Telescope (NOT) (Ergon et al. 2013, this paper) observations show that the yellow supergiant is now gone and indeed was the progenitor of SN 2011dh. We discuss this issue in Sect. 5.4 and provide details of the NOT observations in Appendix B.

The SN has been extensively monitored from X-ray to radio wavelengths by several teams. Optical and NIR photometry and spectroscopy, mainly from the first 50 days, have been published by A11, M11, Tsvetkov et al. (2012, hereafter T12), Vinkó et al. (2012, hereafter V12) and Marion et al. (2013, hereafter M13). Radio and millimeter observations have been published by Martí-Vidal et al. (2011), Krauss et al. (2012), Bietenholz et al. (2012), Soderberg et al. (2012) and Horesh et al. (2012) and X-ray observations by Soderberg et al. (2012), Sasaki & Ducci (2012) and Campana & Immler (2012). The SN has been monitored in UV using SWIFT, in mid-infrared (MIR) using Spitzer and at sub-millimeter wavelengths using Herschel. In this paper we will focus on the UV to MIR emission.

The nature of the progenitor star is an issue of great interest and there has been some debate in the literature. Using approxi-mate models A11 argued that the SN cooled too fast and Soderberg et al. (2012) that the speed of the shock was too high to be consistent with an extended progenitor. However, in B12 we have used detailed hydrodynamical modelling to show that a 3.3-4 $M_\odot$ helium core with an attached thin and extended hydrogen envelope well reproduces the early photometric evolution and is also consistent with the temperature inferred from early spectra. The findings in B12 are in good agreement with those in M11 and the issue now seems to be settled by the disappearance of the yellow supergiant. See also Maeda (2012) for a discussion of the assumptions made in Soderberg et al. (2012).

The presence of a companion star (as for SN 1993J) or not is another issue of great interest. As shown in Benvenuto et al. (2013) a binary interaction scenario that reproduces the observed and modelled properties of the yellow supergiant is certainly possible. Furthermore, the prediction of a blue (compact) companion star would be possible to confirm using HST observations, preferably in the ultraviolet (UV) where the star would be at its brightest.

The paper is organized as follows. In Sections 1.2 and 1.3 we discuss the distance and extinction, in Sect. 2 we present the observations and describe the reduction and calibration procedures, in Sect. 3 we analyse the observations and calculate the bolometric lightcurve, in Sect. 4 we compare the observations to other SNe and in Sect. 5 we provide a discussion, mainly related to the hydrodynamical modelling in B12 and the disappearance of the progenitor. Finally, we conclude and summarize the paper in Sect. 6. In Appendix A we provide details on the calibration of the photometry and in Appendix B we provide details on the progenitor observations.

1.2. Distance

In Table 1 we list all estimates for the distance to M51 we have found in the literature. As the sample is reasonably large and as it is not clear how to judge the reliability of the individual estimates we will simply use a median and the 16 and 84 percentiles to estimate the distance and the corresponding error bars. This gives a distance of $7.8^{+1.1}_{-0.9}$ Mpc which we will use throughout this paper.

1.3. Extinction

The interstellar line-of-sight extinction towards SN 2011dh within the Milky Way as given by the extinction maps presented by Schlegel et al. (1998, hereafter S98) and recently recalibrated by Schlafly & Finkbeiner (2011, hereafter SF11) is $E(B\text{-}V)_{MW}$=0.031 mag. Here and in the following the extinction within the Milky Way, the host galaxy and in total will be subscripted "MW", "H" and "T" respectively and, except where otherwise stated, refer to the interstellar line-of-sight extinction towards the SN. The extinction within host galaxies is generally difficult to estimate. One class of methods used are empirical relations between the equivalent widths of the interstellar Na I D absorption lines and $E(B\text{-}V)$. Relations calibrated to the extinction within other galaxies as the one by Turatto et al. (2003) are based on low resolution spectroscopy and as demonstrated by Poznanski et al. (2011) the scatter is very large. Relations based on high or medium resolution spectroscopy as the ones by Munari & Zwitter (1997, hereafter MZ97) and Poznanski et al. (2012, hereafter P12) show a surprisingly small scatter but are calibrated to the extinction within the Milky Way. Nevertheless, given the line of sight nature of the method and the rough sim-

Table 1. Distance to M51. Literature values.

Distance (Mpc)	Method	Reference
9.60 ±0.80	Size of HII regions	Sandage & Tammann (1974)
6.91 ±0.67	Young stellar clusters	Georgiev et al. (1990)
8.39 ±0.60	Planetary nebula luminosity function	Feldmeier et al. (1997)
7.62 ±0.60	Planetary nebula luminosity function	Ciardullo et al. (2002)
7.66 ±1.01	Surface brightness fluctuations	Tonry et al. (2001)
7.59 ±1.02	Expanding photosphere method (SN 2005cs)	Takáts & Vinkó (2006)
6.36 ±1.30	Type IIP SN standard candle method (SN 2005cs)	Takáts & Vinkó (2006)
8.90 ±0.50	Spectral expanding photosphere method (SN 2005cs)	Dessart et al. (2008)
6.92	Type Ic SN properties (SN 1994I)	Iwamoto & Iwamoto et al. (1994)
7.90 ±0.70	Spectral expanding photosphere method (SN 2005cs)	Baron et al. (2007)
6.02 ±1.92	Spectral expanding photosphere method (SN 1994I)	Baron et al. (1996)
8.36	Type IIP SN standard candle method (SN 2005cs)	Poznanski et al. (2009)
9.30	Tully-Fisher relation	Tully (1988)
8.40 ±0.7	Expanding photosphere method (SNe 2005cs and 2011dh)	Vinkó et al. (2012)

ilarity between M51 and the Milky Way we will use these for an estimate of the extinction within M51. Ritchey & Wallerstein (2012) presented high-resolution spectroscopy of SN 2011dh resolving 8 Na I D components near the M51 recession velocity. The total widths of the Na I D_2 and D_1 lines were 180.1 ± 5.0 and 106.2 ± 5.1 mÅ respectively. Using the MZ97 relations and summing the calculated extinction for all individual components (see discussions in MZ97 and P12) we get $E(B-V)_H$=0.05 mag. Using the P12 relations for the total equivalent widths we get $E(B-V)_H$=0.03 mag. Taking the average of these two values and adding the extinction within the Milky Way (see above) gives $E(B-V)_T$=0.07 mag. Such a low extinction is supported by estimates from X-rays (Campana & Immler 2012) and the progenitor Spectral Energy Distribution (SED) (M11) and we will use this value throughout the paper. The stellar population analysis done by Murphy et al. (2011) suggests a somewhat higher extinction ($E(B-V)_T$=0.14 mag). We will adopt that value and the extinction within the Milky Way as our upper and lower error bars giving $E(B-V)_T$=$0.07^{+0.07}_{-0.04}$ mag. Further constraints on the extinction from the SN itself and comparisons to other SNe is discussed in Sect. 5.1. To calculate the extinction as a function of wavelength we have used the reddening law of Cardelli et al. (1989) and R_V=3.1. For broad-band photometry the extinction was calculated at the mean energy wavelength of the filters. In this paper we will consequently use the definitions from Bessell & Murphy (2012, hereafter BM12) for the mean energy wavelength and other photometric quantities.

2. Observations

2.1. Software

Two different software packages have been used for 2-D reductions, measurements and calibrations of the data. The IRAF based QUBA pipeline (Valenti et al. 2011, hereafter V11) and another IRAF based package developed during this work which we will refer to as the SNE pipeline. This package has been developed with the particular aim to provide the high level of automation needed for large sets of data.

2.2. Imaging

An extensive campaign of optical and NIR imaging was initiated for SN 2011dh shortly after discovery using a multitude of different instruments. Data have been obtained with the Liverpool Telescope (LT), the Nordic Optical Telescope (NOT), Telescopio Nazionale (TNG), Telescopio Carlos Sanchez (TCS), the Calar Alto 3.5m and 2.2m telescopes, the Faulkes Telescope North (FTN), the Asiago 67/92cm Schmidt and 1.82m Copernico telescopes, the William Herschel Telescope (WHT), the Large Binocular Telescope (LBT) and Telescopi Joan Oro (TJO). Amateur observations obtained at the Cantabria and Montcabrer observatories have also been included. The major contributors were the LT, the NOT, the TCS and the TNG. The dataset includes 85 epochs of optical imaging and 22 epochs of NIR imaging for the first 100 days and have been obtained thanks to a broad collaboration of European observers.

2.2.1. Reductions and calibration

The optical raw data were reduced with the QUBA pipeline except for the LT data for which the automatic telescope pipeline reductions have been used.

The NIR raw data were reduced with the SNE pipeline except for UKIRT data for which the reductions provided by CASU have been used. Except for the standard procedures the pipeline has support for second pass sky subtraction using an object mask, correction for field distortion and unsharp masking. Correction for field distortion is necessary to allow co-addition of images with large dithering shifts and has been applied to the TNG data. Unsharp masking removes large scales structures (e.g. the host galaxy) in the images to facilitate the construction of a master sky in the case of large scale structure overlap. Given the (usually) small fields of view and the large size of the host galaxy this technique has been applied to all data where separate sky frames were not obtained.

Photometry was performed with the SNE pipeline. We have used aperture photometry on the reference stars as well as the SN using a relatively small aperture (1.5−2.0 times the FWHM). A mild (>0.1 mag error) rejection of the reference stars as well as a mild (3 σ) rejection of the calculated zero points were also used. Both measurement and calibration errors were propagated using standard formulae. To ensure that the photometry is free

from background contamination we have, as a test, template-subtracted the NOT and LT data sets using a hotpants[1] based tool provided by the sne pipeline and late-time (∼200 days) SN subtracted images. The contamination was negligible in all bands which is not surprising as the SN is still bright compared to the background at ∼100 days.

The optical and NIR photometry was calibrated to the Johnson-Cousins (JC), Sloan Digital Sky Survey (SDSS) and 2 Micron All Sky Survey (2MASS) systems using reference stars in the SN field in turn calibrated using standard fields. The calibration procedure is described in detail in Appendix A where we also discuss the related uncertainties. The photometry was transformed to the standard systems using S-corrections (Stritzinger et al. 2002) except for the JC U and SDSS u bands which were transformed using linear colour-terms. We find the calibration to be accurate to within five percent in all bands. Comparisons to S-corrected SWIFT JC photometry as well as the photometry published in A11, V12 and T12 supports this conclusion although the A11 WISE 1m and M13 photometry differs systematically by ∼20 percent. Note that we have used JC-like $UBVRI$ filters and SDSS-like gz filters at NOT whereas we have used JC-like BV filters and SDSS-like $ugriz$ filters at LT and FTN. The JC-like URI and SDSS-like uri photometry were then tied to both the JC and SDSS systems to produce full sets of JC and SDSS photometry.

2.2.2. Space Telescope Observations

We have also performed photometry on the Spitzer 3.6 and 4.5 μm imaging[2] and the SWIFT optical and UV imaging.

For the Spitzer imaging we performed aperture photometry using the sne pipeline and the zero points and standard aperture provided in the IRAC Instrument Handbook to calculate magnitudes in the natural (energy flux based) Vega system of IRAC. The Spitzer images were template subtracted using a hotpants based tool provided by the sne pipeline and templates constructed from archive images. Comparing with photometry on the original images, the background contamination was less than five percent in all bands.

For the SWIFT imaging we performed aperture photometry using the uvotsource tool provided by the heasoft package and the standard aperture of 5 arcsec to calculate magnitudes in the natural (photon count based) Vega system of UVOT. Observations were combined using the uvotimsum tool provided by the heasoft package and after day 5 subsequently combined in sequences of three to increase the signal-to-noise ratio (SNR). The SWIFT UV images were template subtracted using a hotpants based tool provided by the sne pipeline and templates constructed from archive images ($UVW1$) and SN subtracted late-time (∼80 days) images ($UVM2$ and $UVW2$). Comparing with photometry on the original images, the background contamination was negligible in the $UVW1$ band whereas the $UVM2$ and $UVW2$ bands were severely affected, differing by more than a magnitude at late times. Our SWIFT photometry is in good agreement with that published in M13 exept after ∼10 days in the $UVM2$ and $UVW2$ bands, which is expected since M13 did not perform template subtraction. The SWIFT photometry published in A11, on the other hand, differs systematically by $1-2$ magnitudes at all times. Given the agreement between our S-corrected SWIFT JC U band photometry and JC U band photometry obtained with other telescopes (Sect. 2.2.1) and between

our SWIFT photometry and that published in M13 we find significant systematic errors in our SWIFT photometry to be unlikely.

2.2.3. Results

The S-corrected optical (including SWIFT JC) and NIR magnitudes and their corresponding errors are listed in Tables 3, 4, 5 and 6 and the JC $UBVRI$, SDSS gz and 2MASS JHK magnitudes shown in Fig. 1. The Spitzer 3.6 and 4.5 μm magnitudes and their corresponding errors are listed in Table 7 and shown in Fig. 1. The SWIFT UV magnitudes and their corresponding errors are listed in Table 8 and the SWIFT $UVM2$ magnitudes shown in Fig. 1. As discussed in Appendix A, because of the red tail of the filters and the strong blueward slope of the SN spectrum, the $UVW1$ and $UVW2$ lightcurves do not reflect the evolution of the spectrum at their mean energy wavelengths. These bands will therefore be excluded from any subsequent discussion and the calculation of the bolometric lightcurve in Sect. 3.3. Figure 1 also shows cubic spline fits using 3-5 point knot separation, error weighting and a 5 percent error floor. The standard deviation around the fitted splines is less than 5 percent and mostly less than a few percent except for the SWIFT $UVM2$ band for which the standard deviation is between 5 and 10 percent on the tail. All calculations in Sect. 3, including the bolometric lightcurve, are based on these spline fits. In these calculations the errors have been estimated as the standard deviation around the fitted splines and then propagated.

2.3. Spectroscopy

An extensive campaign of optical and NIR spectroscopic observations was initiated for SN 2011dh shortly after discovery with data obtained from a multitude of telescopes. Data have been obtained with the NOT, the TNG, the WHT, the Calar Alto 2.2m telescope, the Asiago 1.82m Copernico and 1.22m Galileo telescopes and the LBT. The major contributors were the NOT and the TNG. Details of all spectroscopic observations, the telescope and instrument used, epoch and instrument characteristics are given in Table 9. The dataset includes 55 optical spectra obtained at 26 epochs and 18 NIR spectra obtained at 10 epochs for the first 100 days.

2.3.1. Reductions and calibration

The optical and NIR raw data were reduced using the quba and sne pipelines respectively. Flats for NOT Grisms 4 and 5 were spatially shifted, typically by one pixel, to minimize the fringing in the reduced data.

The flux of optical and NIR spectra was extracted using the quba and sne pipelines respectively. A large aperture and error weighting was used to reduce the wavelength dependent effect on the size of the PSF in the spatial direction. No corrections were done for this effect in the dispersion direction. The slit was always (initially) vertically aligned so the position of the PSF in the dispersion direction should not vary much.

The optical spectra were flux calibrated using the quba pipeline. A sensitivity function was derived using a spectroscopic standard star and corrected for the relative atmospheric extinction using tabulated values for each site. Telluric absorption was removed using a normalized absorption profile derived from the standard star. The significant second order contamination present in NOT Grism 4 spectra was corrected for using the

---

[1] http://www.astro.washington.edu/users/becker/hotpants.html
[2] Obtained through the DDT program by G. Helou.
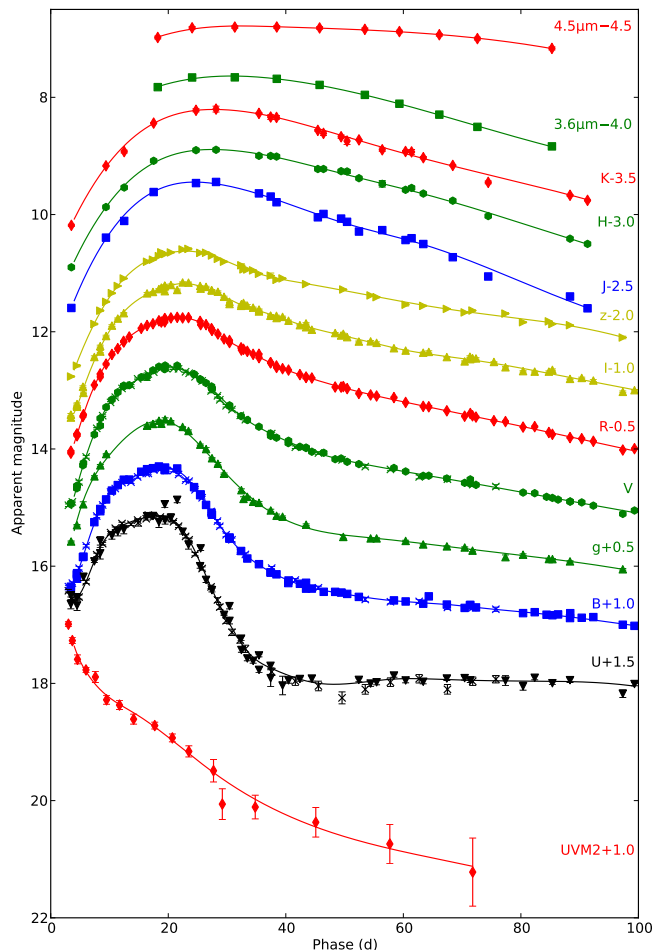
Fig. 1. Photometric evolution of SN 2011dh in the UV, optical, NIR and MIR. For clarity each band have been shifted in magnitude. Each lightcurve have been annotated with the name of the band and the shift applied. We also show the S-corrected SWIFT JC photometry (crosses) and cubic spline fits (solid lines).

method presented in Stanishev (2007). The optical spectra were wavelength calibrated using arc lamp spectra.

The NIR spectra were flux calibrated and the telluric absorption removed with the SNE pipeline. A sensitivity function was derived using solar or Vega analogue standard stars selected from the Hipparcos catalogue and spectra of the sun and Vega. The interstellar extinction of the standards have been estimated from Hipparcos *BV* photometry and corrected for when necessary. The NIR spectra were wavelength calibrated using arc lamp spectra.

Finally, the absolute flux scale of all spectra has been calibrated against interpolated photometry using a least square fit to all bands for which the mean energy wavelength is at least half an equivalent width within the spectral range.

2.3.2. Results

All reduced, extracted and calibrated spectra will be made available for download from the Weizmann Interactive Supernova data REPository[3] (WISeREP) (Yaron & Gal-Yam 2012). Figure 3 shows the sequence of observed spectra where those obtained on the same night using the same telescope and instrument

---
[3] http://www.weizmann.ac.il/astrophysics/wiserep/

have been combined. For clarity, and as is motivated by the frequent sampling of spectra, all subsequent figures in this and the following sections are based on time-interpolations of the spectral sequence. Interpolated spectra separated more than half the sampling time from observed spectra are displayed in shaded colour and should be taken with some care whereas interpolated spectra displayed in full colour are usually more or less indistinguishable from observed spectra. To further visualize the evolution, the spectra have been aligned to a time axis at the right border of the panels. The interpolations were done as follows. First all spectra were re-sampled to a common wavelength dispersion. Then, for each interpolation epoch the spectra closest in time before and after the epoch were identified resulting in one or more wavelength ranges and associated pre- and post-epoch spectra. For each wavelength range the pre- and post-epoch spectra were then linearly interpolated and finally scaled and smoothly averaged using a 500 Å overlap range. Spectra interpolated using this method were also used in the calculations of the bolometric lightcurve (Sect. 3.3) and S-corrections (Appendix A). Figure 2 shows the interpolated optical and NIR spectral evolution of SN 2011dh for days 5−100 with a 5-day sampling. All spectra in this and subsequent figures spectra have been corrected for redshift and interstellar extinction.

3. Analysis

3.1. Photometric evolution

Absolute magnitudes were calculated as $M_i = m_i - \mu - A_i$, where m_i is the apparent magnitude in band i, μ the distance modulus and A_i the interstellar absorption at the mean energy wavelength of band i. The systematic errors stemming from this approximation (as determined from synthetic photometry) is less than a few percent and can be safely ignored. The systematic errors stemming from the uncertainty in distance (Sect. 1.2) and extinction (Sect. 1.3) on the other hand are at the 30 percent level and this should be kept in mind in the subsequent discussions. All bands except the SWIFT *UVM2* band show a similar evolution (the Spitzer MIR imaging did not start until day 20) with a strong initial increase from day 3 to the peak followed by a decrease down to a tail with a roughly linear decline rate. The maximum occurs at increasingly later times for redder bands. The drop from the maximum down to the tail is more pronounced for bluer bands and is not seen for bands redder than *z*. Both these trends are reflections of the strong decrease in temperature seen between 10 and 40 days (Fig. 5). The tail decline rates are highest for the reddest bands and almost zero for the bluest bands. It is interesting to note that the Spitzer 4.5 μm band breaks this pattern and shows a markedly slower decline than the 3.6 μm and the NIR bands. Warm dust or CO fundamental band emission are two possible explanations (Sect. 5.5). The times and absolute magnitudes of the maximum as well as the tail decline rates at 60 days are listed in Table 2 as measured from cubic spline fits (Fig. 1).

Early time data for the first three days have been published in A11 and T12 and show a strong decline in the *g*, *V* and *R* bands. This initial decline phase ends at about the same time as our observations begins.

3.2. Colour evolution and blackbody fits

Figure 4 shows the intrinsic *U-V*, *B-V*, *V-I* and *V-K* colour evolution of SN 2011dh given the adopted extinction. Initially we see a quite strong blueward trend in the *V-I* and *V-K* colours

Table 2. Times and absolute magnitudes of the maximum and tail decline rates at 60 days as measured from cubic spline fits.
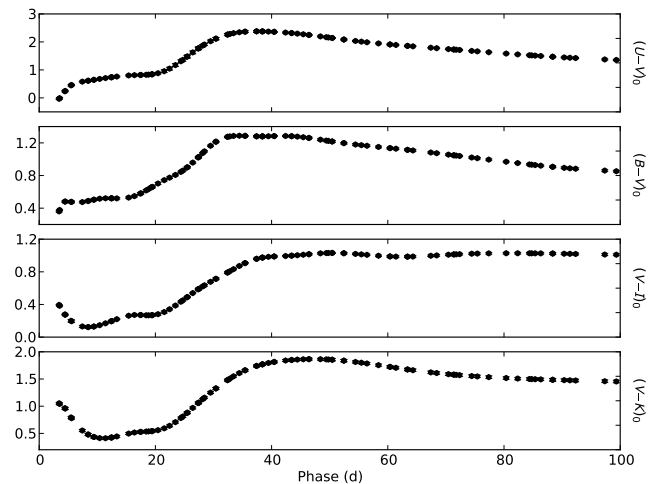
Band	Maximum (days)	Absolute magnitude (mag)	Decline rate (mag day^{-1})
UVM2	...	...	0.019
U	18.30	-16.16	-0.002
B	18.88	-16.43	0.007
V	20.22	-17.08	0.018
R	21.86	-17.38	0.021
I	22.62	-17.41	0.020
J	24.45	-17.58	0.027
H	27.42	-17.61	0.025
K	27.71	-17.78	0.027
3.6 μm	31.55	-17.83	0.028
4.5 μm	39.62	-18.18	0.009

Fig. 4. *U-V*, *B-V*, *V-I* and *V-K* intrinsic colour evolution for SN 2011dh for the adopted extinction.

Fig. 5. Evolution of the blackbody temperature for SN 2011dh as inferred from fits to the *V*, *I*, *J*, *H* and *K* bands for the adopted extinction (black dots). We also show the evolution of the blackbody temperature for two higher extinction scenarios, $E(B-V)_T=0.2$ mag (red crosses) and $E(B-V)_T=0.3$ mag (blue pluses), discussed in Sect. 5.1.

reaching a minimum at ~10 days which is not reflected in the *U-V* and *B-V* colours. Subsequently all colours redden reaching a maximum at ~40 days for the *U-V* and *B-V* colours and ~50 days for the *V-I* and *V-K* colours followed by a slow blueward trend for all colours. Figures 5 and 6 show the evolution of blackbody temperature and radius as inferred from fits to the *V*, *I*, *J*, *H* and *K* bands given the adopted extinction. As discussed in Sect. 3.4, the flux in bands blueward of *V* is strongly reduced by the line opacity in this region, in particular between 10 and 30 days. Therefore we have excluded these bands from the fits whereas the *R* band has been excluded to avoid influence from Hα emission at early times. Note that the temperature and radius obtained correspond to the surface of thermalization rather than the photosphere (total optical depth ~1) and lose physical meaning when the ejecta become optically thin in the continuum. The evolution of the *V-I* and *V-K* colours is reflected in the evolution of the blackbody temperature, initially increasing from ~7000 K at 3 days to a maximum of ~9000 K at 8 days, subsequently decreasing to a minimum of ~5000 K at ~50 days followed by a slow increase. The blackbody radius shows an almost linear increase from ~0.4 ×10^{15} cm to a maximum of ~1.2 ×10^{15} cm and a subsequent almost linear decrease. In Fig. 6 we also show the radius corresponding to the P-Cygni minimum of the Fe II 5169 Å line. Interpreting this (Sect. 3.4) as the photospheric radius and the blackbody radius as the thermalization radius we see a fairly consistent evolution between 8 and 40 days corresponding to a dilution factor of ~0.8. The figure also suggests that such an interpretation breaks down for later epochs.
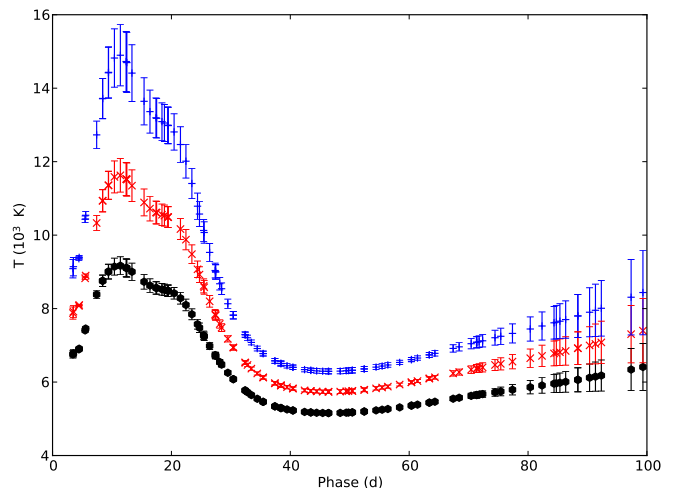
3.3. Bolometric evolution

To calculate the pseudo-bolometric lightcurve of SN 2011dh we have used a combination of two different methods. One, which we will refer to as the spectroscopic method, for wavelength regions with spectral information and one, which we will refer to as the photometric method, for wavelength regions without. The prefix pseudo here refers to the fact that a true bolometric lightcurve should be integrated over all wavelengths. We do not assume anything about the flux in wavelength regions not covered by data but discuss this issue at the end of the section.

When using the spectroscopic method we divide the wavelength region into sub-regions corresponding to each photomet-

ric band. For each epoch of photometry in each of the sub-regions a bolometric correction $BC_i = M^{syn}_{bol,i} - M^{syn}_i$ is determined. Here M^{syn}_i and $M^{syn}_{bol,i}$ are the absolute and bolometric magnitudes respectively, as determined from synthetic photometry and integration of the sub-region flux per wavelength using observed spectra. The bolometric magnitude in the region $M_{bol} = -2.5 \log \sum 10^{-0.4(M_i+BC_i)}$ is then calculated as the sum over all sub-regions, where M_i is the absolute magnitude as determined from observed photometry. Spectra are linearly interpolated to match each epoch of photometry as described in Sect. 2.3.2. This method makes use of both spectral and photometric information and is well motivated as long as the spectral sampling is good.

When using the photometric method we log-linearly interpolate the flux per wavelength between the mean energy wavelengths of the filters. This is done under the constraint that the synthetic absolute magnitudes as determined from the interpolated SED equals the absolute magnitudes as determined from observed photometry. The solution is found by a simple itera-
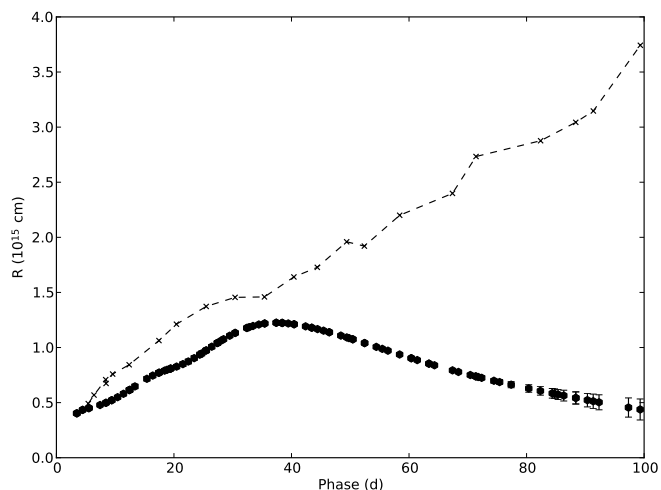
Fig. 6. Evolution of blackbody radius for SN 2011dh as inferred from fits to the *V, I, J, H* and *K* bands for the adopted extinction. The radius corresponding to the P-Cygni minimum of the Fe II 5169 Å line is also shown (dashed line).

Fig. 7. Pseudo-bolometric UV-MIR lightcurve for SN 2011dh calculated with the spectroscopic (black dots) and photometric (red dots) method. The upper and lower error bars for the systematic error arising from extinction and distance (black dashed lines) is also shown.

tive scheme. The total flux in the region is then calculated by integration of the interpolated flux per wavelength.

The absolute magnitudes in each band were calculated using cubic spline fits (Fig. 1) as is justified by the frequent sampling in all bands. When necessary, as for the SWIFT UV and Spitzer MIR magnitudes, extrapolations were done assuming a constant colour. The filter response functions and zeropoints used to represent the different photometric systems are discussed in Appendix A.

For SN 2011dh we have optical and NIR spectra with good sampling between 3 and 100 days and we have used the spectroscopic method in the *U-K* region and the photometric method in the UV and MIR regions. The pseudo-bolometric UV-MIR (1900-50000 Å) lightcurve of SN 2011dh is shown in Fig. 7 and listed in Table 10 for reference. This data together with the photospheric velocity as estimated in Sect. 2.3.2 provide the observational basis for the hydrodynamical modelling of SN 2011dh presented in B12. For comparison we also show the pseudo-bolometric lightcurve calculated using the photometric method only. The difference is small but, as expected, increases slowly when the spectrum evolves to become more line dominated. The bolometric lightcurve shows the characteristics common to Type I and Type IIb SNe with a rise to peak luminosity followed by a decline phase and a subsequent tail phase with a roughly linear decline rate (Sect. 5.2). The maximum occurs at 20.8 days at a pseudo-bolometric luminosity of $17.15 \pm 0.06^{+6.78}_{-3.78} \times 10^{41}$ ergs s^{-1}, where the second error bars give the systematic error arising from the distance and extinction. The tail decline rates are 0.033, 0.021, 0.022 and 0.020 mag day^{-1} at 40, 60, 80 and 100 days respectively.

Figure 8 shows the fractional luminosity in the UV (1900-3300 Å), optical (3300-10000 Å), NIR (10000-24000 Å) and MIR (24000-50000 Å) regions respectively. The optical flux dominates and varies between ~75 and ~60 percent whereas the NIR flux varies between ~15 and ~30 percent. The UV flux initially amounts to ~10 percent, decreasing to ~1 percent at the beginning of the tail and onwards. The MIR flux initially amounts to ~1 percent, increasing to ~5 percent at the beginning of the tail and onwards. The evolution of the fractional luminosities mainly reflects the evolution of the temperature (Fig. 5)
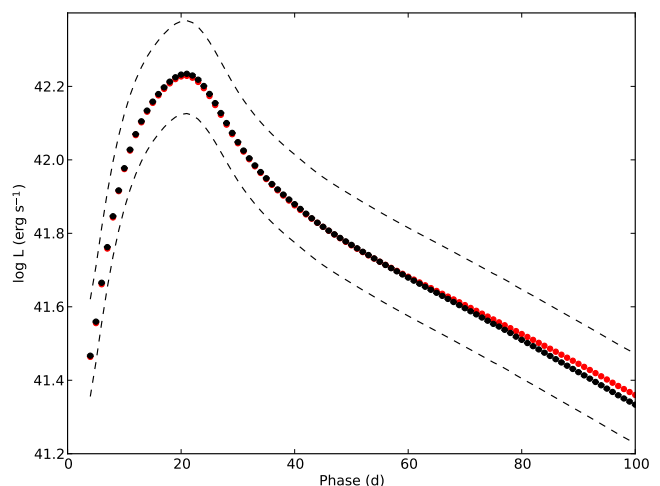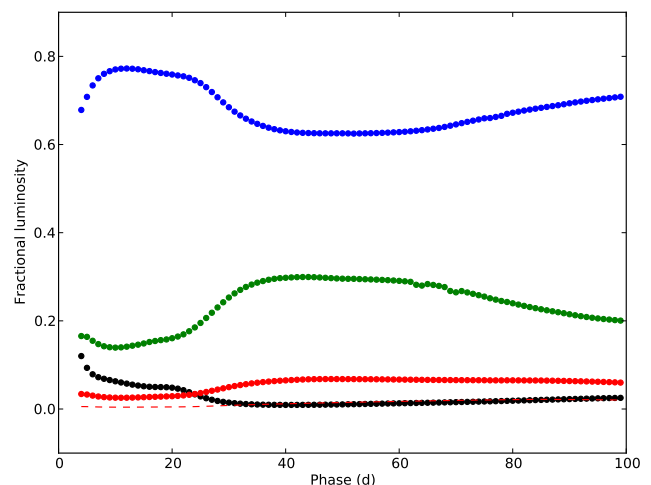
Fig. 8. Fractional UV (black dots), optical (blue dots), NIR (green dots) and MIR (red dots) luminosity for SN 2011dh. The fractional Rayleigh-Jeans luminosity redwards of 4.5 μm (red dashed line) is also shown for comparison.

although we expect the UV to be quite sensitive to the evolution of the line opacity (Sect. 3.4).

Figure 9 shows the evolution of the SED as calculated with the photometric method overplotted with the blackbody fits discussed in Sect. 3.2 as well as the observed spectra interpolated as described in Sect. 2.3.2. The strong blueward slope in the UV region (except for the first few days) suggests that the flux bluewards of the *UVM*2 band is negligible. The flux redwards of 4.5 μm could be approximated with a Rayleigh-Jeans tail or a model spectrum. As shown in Fig. 8 the fractional Rayleigh-Jeans luminosity redwards of 4.5 μm is at the percent level. Note again the excess at 4.5 μm that develops between 50 and 100 days. Whereas the other bands redward of *V* are well approximated by the blackbody fits the flux at 4.5 μm is a factor of ~5 in excess at 100 days. Note also the strong reduction of the flux as compared to the fitted blackbodies in bands blueward of *V* between 10 and 30 days (Sect. 3.4).
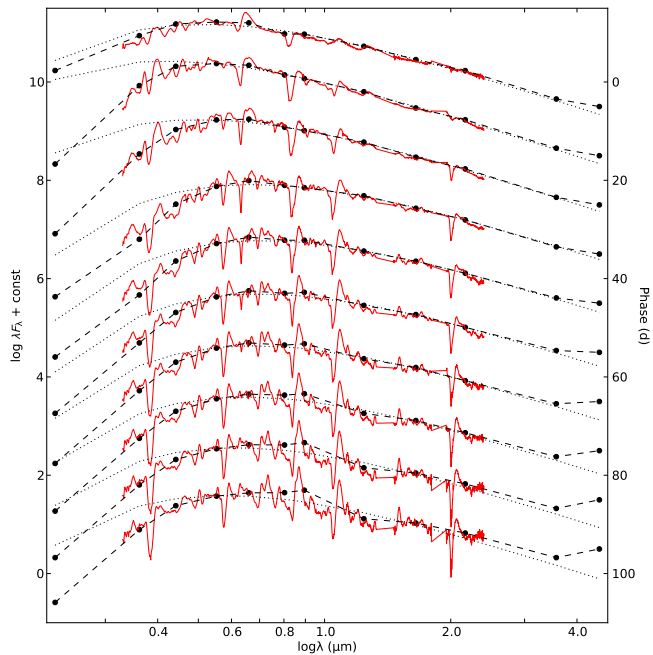
Fig. 9. The evolution of the SED as calculated with the photometric method (black dots and dashed lines) overplotted with the blackbody fits discussed in Sect. 3.2 (black dotted lines) as well as the observed spectra interpolated as described in Sect. 2.3.2 (red solid lines).

Fig. 10. Modelled and observed optical spectrum at 15 days. Lines identified by their optical depth being $\gtrsim 1$ have been marked at their rest wavelength. We also show model spectra for two higher extinction scenarios, $E(B-V)_T = 0.2$ mag and $E(B-V)_T = 0.3$ mag, discussed in Sect. 5.1.

3.4. Spectroscopic evolution

We have used a SN atmosphere code implementing the method presented by Mazzali & Lucy (1993) and the B12 He4R270 ejecta model with all elements expect hydrogen and helium replaced with solar abundances to aid in identification of lines and some qualitative analysis of the spectra. The Monte-Carlo based method treats line and electron scattering in the nebular approximation where the ionization fractions and level populations of bound states are determined by the radiation field approximated as a diluted blackbody parametrized by a radiation temperature. Line emission will be underestimated as the contribution from recombination is not included whereas line absorption is better reproduced. Following Mazzali & Lucy (1993), for each epoch we have determined the temperature for the blackbody emitting surface from fits to the V, I, J, H and K bands and iterated the radius until the observed luminosity was achieved. Note that, except for the temperature peak between $\sim$10 and $\sim$20 days, the He I lines cannot be reproduced by the model as non-thermal excitation from the ground state is needed to populate the higher levels (Lucy 1991). For a quantitative analysis a NLTE-treatment solving the rate equations is necessary, in particular with respect to non-thermal excitations and ionizations. Figure 10 shows a comparison between model and observed spectra at 15 days where we also have marked the rest wavelengths of lines identified by their optical depth being $\gtrsim 1$. The atmosphere model is appropriate at early times when the approximation of a blackbody emitting surface is justified and we do not use it for phases later than $\sim$30 days. To aid in line-identifications at later times we use preliminary results from NLTE spectral modelling of the SN spectrum at 100 days to be presented in Jerkstrand et al. 2013 (in preparation). The details of this code have been presented in Jerkstrand et al. (2011, 2012). Both the atmosphere and NTLE code uses the same atomic data as described in these papers. The lines identified by the atmo-

sphere modelling, the NLTE modelling or both are discussed below and have been marked in Fig. 2.
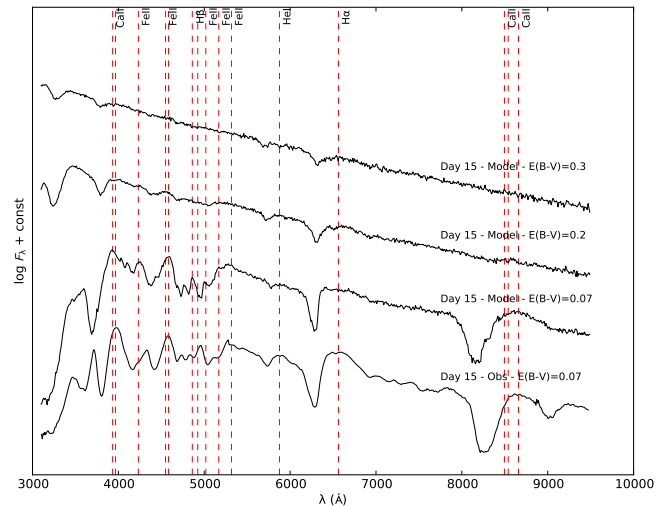
The transition of the spectra from hydrogen (Type II) to helium (Type Ib) dominated starts at $\sim$10 days with the appearance of the He I 5876 and 10830 Å lines and ends at $\sim$80 days with the disappearance of the Hα line. This transition is likely determined by the photosphere reaching the helium core, the ejecta gradually becoming optically thin to the γ-rays and eventually to the hydrogen lines. At 3 days the hydrogen signature in the spectrum is strong and we identify the Balmer series α–γ, Paschen series α–γ as well as Bracket γ using the atmosphere modelling. Hα shows a strong P-Cygni profile, extending in absorption to at least $\sim$25000 km s^{-1}, which gradually disappears in emission but stays strong in absorption until $\sim$50 days. Most other hydrogen lines fade rather quickly and have disappeared at $\sim$30 days. Weak absorption in Hα and Hβ remains until $\sim$80 days. Figure 11 shows closeups of the evolution centred on the hydrogen Balmer lines. Note that the absorption minimum for Hα as well as Hβ is never seen below $\sim$11000 km s^{-1} but approaches this value as the lines get weaker (see also Fig. 13). This suggests that a transition in the ejecta from helium core to hydrogen rich envelope material occurs at this velocity. Atmosphere modelling of the hydrogen lines using the B12 He4R270 ejecta model with all elements except hydrogen and helium replaced with solar abundances well reproduce the observed evolution of the absorption minima and the minimum velocity coincides with the model interface between the helium core and hydrogen rich envelope at $\sim$11500 km s^{-1}. The good agreement with the observed minimum velocity gives further support to the B12 ejecta model. M13 estimated hydrogen to be absent below $\sim$12000 km s^{-1} by fitting a SYNOW (Branch et al. 2003) model spectrum to the observed spectrum at 11 days. We find the behaviour of the hydrogen lines in the weak limit to provide a better constraint and conclude that the interface between the helium core and hydrogen rich envelope is likely to be located at $\sim$11000 km s^{-1}. By varying the fraction of hydrogen in the envelope we find a hydrogen mass of 0.01-0.04 M$_\odot$, in agreement with the 0.02 M$_\odot$ in the original model, to be consistent with the observed evolution of the hydrogen lines. A11 used spectral modelling similar
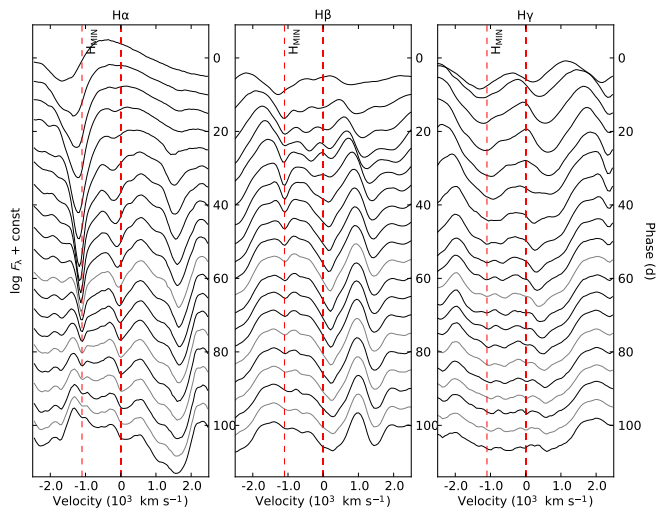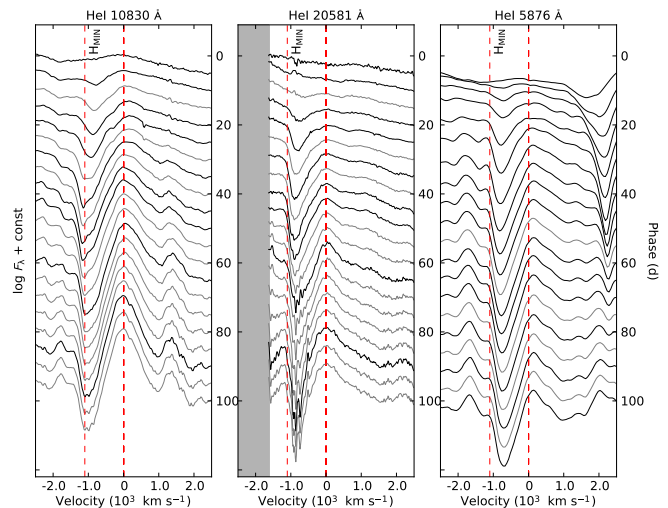
Fig. 11. Closeup of (interpolated) spectral evolution centred on the Hα (left panel), Hβ (middle panel) and Hγ (right panel) lines. All panels in this and the following figure show the minimum velocity for the Hα absorption minimum (marked H_{MIN}) interpreted as the interface between the helium core and hydrogen envelope.

Fig. 12. Closeup of (interpolated) spectral evolution centred on the He I 10830 Å (left panel), He I 20581 Å (middle panel) and He I 5876 Å (right panel) lines.

to the one in this paper, but with a NLTE treatment of hydrogen and helium, to estimate the hydrogen mass to 0.024 $M_\odot$.

The He I lines appears in the spectra between ∼10 (He I 10830 and 5876 Å) and ∼15 (He I 6678, 7065 and 20581 Å) days. Later on we see the 5016 and 17002 Å lines emerge as well. As mentioned the atmosphere modelling does not well reproduce the He I lines but those identified here are present in the model spectrum with optical depths of 0.1−5 during the temperature peak between ∼10 and ∼20 days. Increasing the He I excitation fraction to mimic the non-thermal excitation reproduce the He I lines and their relative strengths reasonably well. At 100 days, all He I lines, except He I 17002 Å, are present and identified by the NLTE modelling. Given the low ionization potential of Na I and the high temperatures we find it unlikely that He I 5876 is blended with Na I 5890/5896 at early times. Using the atmosphere modelling we find a very low ion fraction of Na I ($<10^{-7}$) and the optical depth for Na I 5890/5896 to be negligible during the first 30 days. Using the NLTE modelling at 100 days we find emission to arise primarily from Na I 5890/5896 and absorption to be a blend. He I 10830 is likely to be blended with Paschen γ at early times and He I 5016 Å is likely to be blended with Fe I 5018 Å. Figure 12 shows a closeup of the evolution centred on the He I lines. Helium absorption is mainly seen below the ∼11000 km s^{-1} attributed to the interface between the helium core and the hydrogen rich envelope although He I 10830 Å absorption extends beyond this velocity and also shows a narrow dip close to it between ∼30 and ∼60 days (see also Fig. 13). We may speculate that this dip is caused by a denser shell of material close to the interface as was produced in explosion modelling of SN 1993J (e.g. Woosley et al. 1994). Whereas the fading and disappearance of the hydrogen lines are driven by the decreasing density and temperature of the envelope the appearance and growth of the helium lines is likely to be more complex. M13 suggest that the helium lines appear because the photosphere reaches the helium core. However, Fig. 13 (see below) suggests that the photosphere reaches the helium core at 5-7 days whereas the helium lines appear later, at lower velocities, close to the region where we expect the continuum photosphere to be located and then move outwards in velocity until ∼40 days. This rather

suggest the appearance and subsequent evolution to be driven by increasing non-thermal excitation due to the decreasing optical depth for the γ-rays. For the line optical depth at a given velocity we have $\tau \propto t^{-2}x_l$, where x_l is the fraction of He I in the lower state. As the temperature decreases after ∼10 days and the ion fraction of He I is high according to the modelling, we would expect the line optical depth at a given velocity to decrease if non-thermal excitation was not important. Detailed modelling including a treatment of non-thermal excitation of the helium lines is needed to better understand the behaviour of the He I lines.

Except for H I and He I we also identify lines from Ca II, Fe II, O I, Mg I and Na I in the spectra. The Ca II 3934/3968 Å and 8498/8542/8662 Å lines are present throughout the evolution showing strong P-Cygni profiles and are identified by both the atmosphere and NLTE modelling whereas the [Ca II] 7291/7323 Å line is identified by the NLTE modelling at 100 days. The O I 5577, 7774, 9263, 11300, and 13164 Å lines are all identified by the NLTE modelling at 100 days. The atmosphere modelling does not reproduce the O I lines at early times but the O I 7774 Å line seems to appear already at ∼25 days and the other lines between ∼30 and ∼50 days. The NLTE modelling also identifies the emerging [O I] 6300/6364 lines at 100 days. The Mg I 15040 Å line is identified by the NLTE modelling at 100 days and seem to emerge at ∼40 days. As mentioned above we identify the Na I 5890/5896 Å lines in emission and blended in absorption with the He I 5876 Å line at 100 days using the NLTE modelling. In the region 4000−5500 Å, we identify numerous Fe II lines using the atmosphere modelling, the most prominent being Fe II 4233, 4549, 4584, 4924, 5018, 5169 and 5317 Å. These lines are present already at ∼5 days and most of them persist to at least 50 days. As mentioned in Sect. 3.3 and as can be seen in Fig. 9 there is a strong reduction of the flux bluewards of 5000 Å between ∼10 and ∼30 days. This well known behaviour, which is also reproduced by the modelling, is caused by an increased line opacity from a large number of metal ion (e.g. Fe II and Cr II) lines. This explains the initial redward trend in the U-V and B-V colours contrary to the blueward trend in V-I and V-K caused by the increasing temperature (see Fig. 4). Judging from Fig. 9 the reduction of the flux is considerably reduced after ∼30 days.
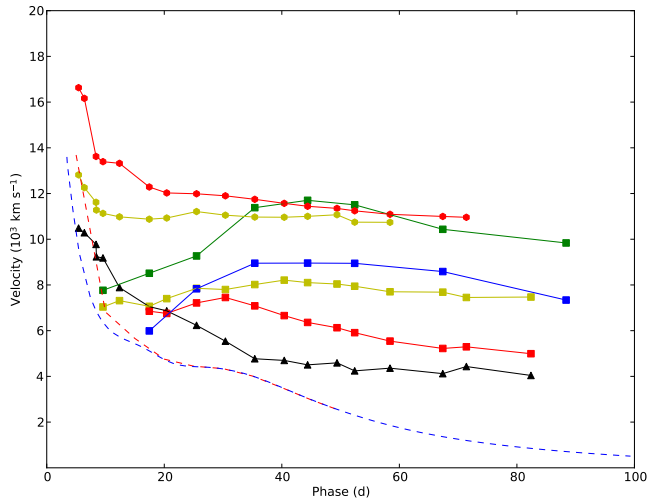
Fig. 13. Velocity evolution of the absorption minimum of the Fe II 5169 Å (black triangles), He I 5876 Å (yellow squares), He I 6678 Å (red squares), He I 10830 Å (green squares), He I 20581 Å (blue squares), Hα (red circles) and Hβ (yellow circles) lines as automatically measured from the spectral sequence. For comparison we also show the velocity corresponding to the blackbody radius as determined from fits to the photometry (blue dashed line) and as iteratively determined by the atmosphere modelling (red dashed line).

Figure 13 shows the evolution of the absorption minimum for a number of lines as determined from the spectral sequence. These were measured by a simple automatic centring algorithm where the spectra were first smoothed down to 500 km s^{-1} and the absorption minimum then traced through the interpolated spectral sequence and evaluated at the dates of observation. We also show the velocity corresponding to the blackbody radius as determined from fits to the photometry and as iteratively determined by the atmosphere modelling. Because of backscattering, the model blackbody radius is larger than the fitted. It is reasonable to expect that the photosphere is located somewhere between the blackbody surface and the region where the line with the lowest velocity is formed. This line is the Fe II 5169 Å line which was used in B12 to estimate the photospheric velocities. This means that the photospheric velocities might be overestimated with up to 50 percent and in section 5.3 we will discuss how such an error would effect the results in B12.

4. Comparison to other SNe

In this section we compare the observations of SN 2011dh to the well observed Type IIb SNe 1993J and 2008ax. In order to do this we need to estimate the distance and extinction. This will be done without assuming similarity among the SNe and in analogy with SN 2011dh we will use high-resolution spectroscopy of the Na I D and K I 7699 Å interstellar absorption lines to estimate the extinction. In the end of the section we will investigate what difference an assumption of similarity among the SNe will make.

4.1. SN 1993J

SN 1993J which occurred in M81 is one of the best observed SNe ever and the nature of this SN and its progenitor star is quite well understood. Shigeyama et al. (1994) and Woosley et al. (1994) used hydrodynamical modelling to show that a progenitor star with an initial mass of 12−15 $M_\odot$ with an extended (not

specified) but low mass (0.2−0.9 $M_\odot$) hydrogen envelope reproduces the observed bolometric lightcurve. This was confirmed by the more detailed modelling of Blinnikov et al. (1998). Progenitor observations were presented in Maund et al. (2004) while Stancliffe & Eldridge (2009) used stellar evolutionary models to show that a progenitor star with an initial mass of 15−17 $M_\odot$ with an extended but low mass hydrogen envelope, stripped through mass transfer to a companion star, reproduces the observed progenitor luminosity and effective temperature. Photometric and spectroscopic data for SN 1993J were taken from Lewis et al. (1994), Richmond et al. (1996), Matthews et al. (2002), Wada & Ueno (1997) and IAU circulars.

The distance to M81 is well constrained by Cepheid measurements, the mean and standard deviation of all such measurements listed in the NASA/IPAC Extragalactic Database (NED) being 3.62±0.22 Mpc, which we will adopt. The extinction within the Milky Way as given by the S98 extinction maps recalibrated by SF11 is $E(B\text{-}V)_{\rm MW}$=0.07 mag. Richmond et al. (1994) discuss the extinction in some detail and suggest a total $E(B\text{-}V)_{\rm T}$ between 0.08 and 0.32 mag. High-resolution spectroscopy of the Na I D lines was presented in Bowen et al. (1994). Given the rough similarity between M81 and the Milky Way we will use the MZ97 and P12 relations to estimate the extinction within M81. Bowen et al. (1994) resolve a system of components near the M81 recession velocity and another one near zero velocity. There is also a third system which the authors attribute to extragalactic dust in the M81/M82 interacting system. The individual components of all three systems are quite heavily blended. As it is not clear whether the third system belongs to the Milky Way or M81, we calculate the extinction for all the three systems with the MZ97 and P12 relations and sum to get estimates of the total extinction. The MZ97 relation gives $E(B\text{-}V)_{\rm T}$=0.28 mag and the P12 relations $E(B\text{-}V)_{\rm T}$=0.17 mag (on average). Given that each system clearly consists of multiple components the MZ97 relation rather provides an upper limit (see discussion in MZ97) and we will adopt the lower value given by the P12 relations. Adopting the higher value given by the MZ97 relation and the extinction within the Milky Way as upper and lower error limits we then get $E(B\text{-}V)_{\rm T}$=0.17$^{+0.11}_{-0.10}$ mag.

4.2. SN 2008ax

SN 2008ax is another well observed Type IIb SN but the nature of this SN and its progenitor star is not as well understood as for SN 1993J. Tsvetkov et al. (2009) used the hydrodynamical code STELLA (Blinnikov et al. 1998) to show that a progenitor star with an initial mass of 13 $M_\odot$ with an extended (600 $R_\odot$) and low mass (not specified) hydrogen envelope well reproduces the $UBVRI$ lightcurves except for the first few days. Progenitor observations were presented in Crockett et al. (2008) but the conclusions about the nature of the progenitor star were not clear. Photometric and spectroscopic data for SN 2008ax were taken from Pastorello et al. (2008), Roming et al. (2009), Tsvetkov et al. (2009), Taubenberger et al. (2011) and Chornock et al. (2011, hereafter C11).

The distance to the host galaxy NGC 4490 is not very well known. We have found only three measurements in the literature (Tully 1988; Terry et al. 2002; Theureau et al. 2007). Taking the median and standard deviation of these and the Virgo, Great Attractor and Shapley corrected kinematic distance as given by NED we get 9.38±0.85 Mpc which we will adopt. The extinction within the Milky Way as given by the S98 extinction maps recalibrated by SF11 is $E(B\text{-}V)_{\rm MW}$=0.02 mag. High resolution
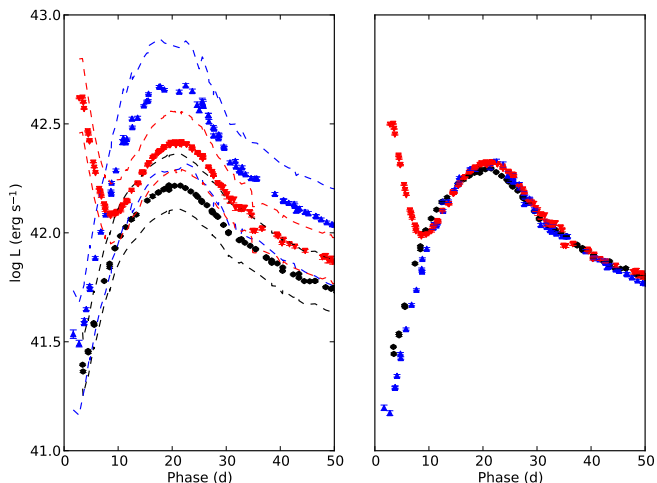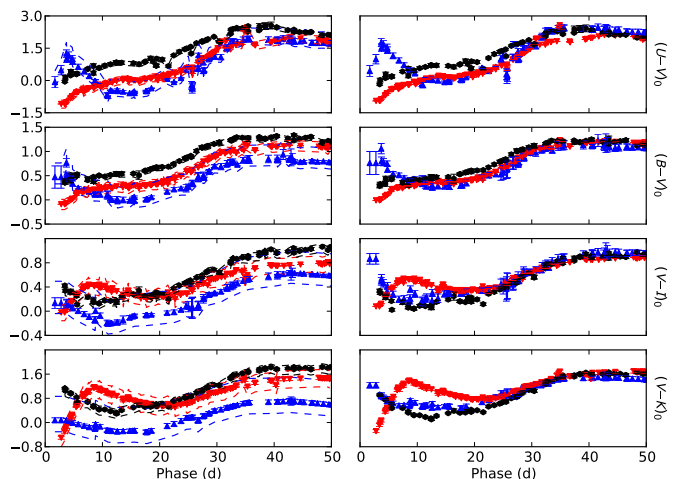
Fig. 14. Pseudo-bolometric *U-K* lightcurve for SN 2011dh (black) as compared to SNe 1993J (red) and 2008ax (blue) for the adopted extinctions (left panel) and for a revised scenario where we have set $E(B-V)_T$ to 0.14, 0.09 and 0.27 mag for SNe 2011dh, 1993J and 2008ax respectively (right panel). In the left panel we also show the systematic error arising from the distance and extinction (dashed lines).

Fig. 15. Colour evolution of SN 2011dh (black) as compared to SNe 1993J (red) and 2008ax (blue) for the adopted extinctions (left panel) and for a revised scenario where we have set $E(B-V)_T$ to 0.14, 0.09 and 0.27 mag for SNe 2011dh, 1993J and 2008ax respectively (right panel). In the left panel we also show the systematic error arising from the extinction (dashed lines).

spectroscopy of the Na I D and K I 7699 Å lines were presented in C11. The host galaxy NGC 4490 is a quite irregular galaxy so it is not clear if relations calibrated to the Milky Way are applicable. However, as we have no alternative, we will use the MZ97 relations to estimate the extinction within NGC 4490. The C11 spectra show blended multiple components of the Na I D_2 line most of which are clearly saturated. We measure the total equivalent width to 1.0 Å which using the linear (unsaturated) part of the MZ97 relation corresponds to a lower limit of $E(B-V)_H > 0.25$ mag. As the Na I D_2 lines are saturated we cannot use these to derive a useful upper limit. C11 measures the total equivalent width of the K I 7699 Å line components to 0.142 Å which using the corresponding MZ97 relation gives $E(B-V)_H = 0.54$ mag. Adding the extinction within the Milky way and adopting the lower limit from the MZ97 Na I D_2 relation and the extinction corresponding to the bluest SN colours allowed for a blackbody (Sect. 5.1) as the lower and upper error limits we then get $E(B-V)_T = 0.56^{+0.14}_{-0.29}$ mag.

4.3. Comparison

The left panel of Fig. 14 shows the pseudo-bolometric *U-K* (3000-24000 Å) lightcurves of SNe 2011dh, 1993J and 2008ax as calculated with the photometric method (Sect. 3.3). Magnitudes have been linearly interpolated in colour and extrapolated assuming constant colour. Except for the first few days the shape is similar and they all show the characteristics common to Type I and IIb SNe lightcurves (Sect. 5.2). As shown in B12 the differences during the first few days could be explained by differences in the radius and mass of the hydrogen envelope. Given the adopted distances and extinctions SN 2011dh is fainter than SN 1993J which, in turn, is fainter than SN 2008ax. The peak luminosity occurs at similar times but the peak-to-tail luminosity ratio for SN 2011dh is smaller than for SN 1993J which, in turn, is smaller than for SN 2008ax.

The left panel of Fig. 15 shows the colour evolution for the three SNe. Magnitudes have been linearly interpolated in colour. As for the lightcurves, the shape is quite different for the first few

days which could again be explained by differences in the radius and mass of the hydrogen envelope. The shape of the subsequent evolution is quite similar with a blueward trend in the *V-I* and *V-K* colours (corresponding to increasing temperature) during the rise to peak luminosity and then a redward trend in all colours (corresponding to decreasing temperature) to a colour maximum at 40–50 days and a subsequent slow blueward trend. Given the adopted extinction, SN 2011dh is redder than SN 1993J which, in turn, is redder than SN 2008ax.

In Figures 16 and 17 we show closeups of the spectral evolution centred on the Hα and the He I 10830 Å lines. The minimum velocity for the Hα absorption minimum has been marked and occurs at ∼9000, ∼11000 and ∼13000 km s^{-1} for SNe 1993J, 2011dh and 2008ax respectively. As discussed in Sect. 3.4 this velocity likely corresponds to the interface between the helium core and the hydrogen envelope for SN 2011dh. The Hα line disappears at ∼50 days for SN 2008ax, at ∼80 days for SN 2011dh and is still strong at 100 days for SN 1993J. Figure 18 shows the evolution of the absorption minimum for the Fe II 5169 Å, He I 5876 and 6678 Å and Hα lines measured as described in Sect. 3.4. Interpreting the Fe II 5169 Å absorption minimum as the photosphere and the minimum velocity for the Hα absorption minimum as the interface between the helium core and the hydrogen envelope the photosphere reaches the helium core at ≲10, ∼5 and ≲10 days for SNe 1993J, 2011dh and 2008ax respectively. The helium lines appear at ∼20, ∼10 and ∼5 days for SNe 1993J, 2011dh and 2008ax respectively, at lower velocities close to the region where we expect the continuum photosphere to be located. The initial evolution is different among the SNe but after ∼30 days the helium lines have increased in strength, moved outward as compared to the photosphere and show a quite similar evolution for all three SNe. The evolution of the Fe II 5169 Å line is very similar for SNe 1993J and 2011dh but a bit different for SN 2008ax. In general, lines originating closer to the photosphere seem to have similar velocities for the three SNe whereas lines originating further out in the ejecta seem to have progressively higher velocities for SNe 1993J, 2011dh and 2008ax respectively.
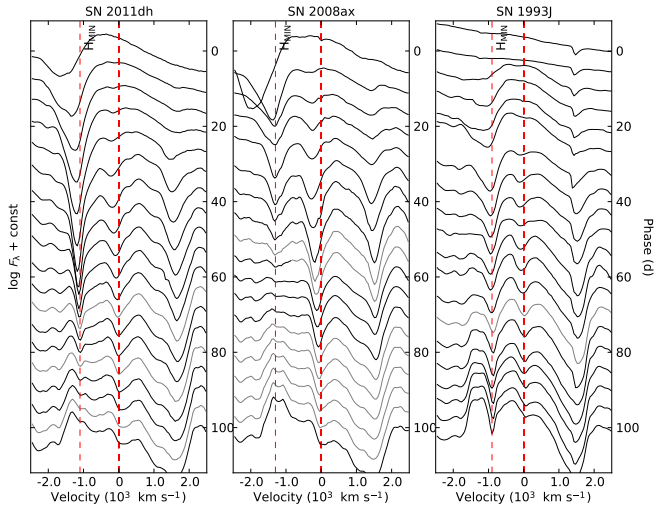
Fig. 16. The (interpolated) evolution of the Hα line for SN 2011dh (left panel) as compared to SNe 2008ax (middle panel) and 1993J (right panel). All panels in this and the following figure show the minimum velocity for the Hα absorption minimum (marked H_{MIN}) interpreted as the interface between the helium core and hydrogen envelope.
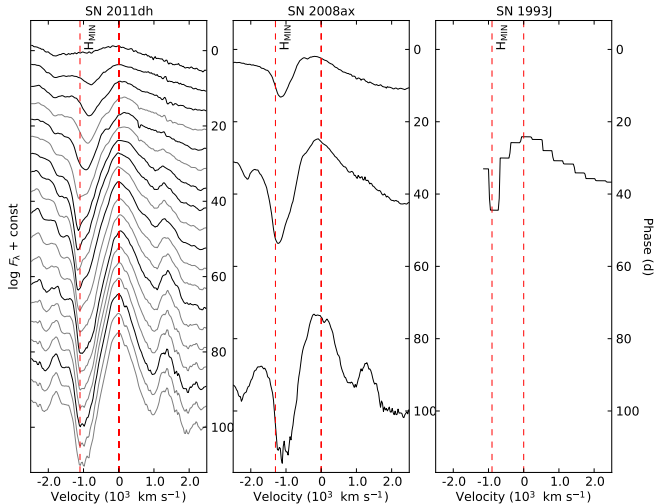
Fig. 17. The (interpolated) evolution of the He I 10830 Å line for SN 2011dh (left panel) as compared to SNe 2008ax (middle panel) and 1993J (right panel). Given the sparse data available for SNe 1993J and 2008ax we show observed spectra for these SNe.

The differences in peak and tail luminosities suggest differences in the mass of ejected ^{56}Ni (Sect. 5.2). The differences in peak-to-tail luminosity ratios suggest differences in the ejecta mass, explosion energy and/or distribution of ^{56}Ni (Sect. 5.2). However, as seen in the left panels of Figures 14 and 15 the systematic errors in the luminosity and colour arising from the distance and extinction is large so similarity among the SNe cannot be excluded. M13 find both the luminosities and the colours to be similar, mainly due to differences in the adopted distances and extinctions. The similar velocities of lines originating closer to the photosphere and the times at which peak luminosity occurs, both of which are independent of the distance and extinction, suggests similar ejecta masses and explosion energies (Sect. 5.2). Although the differences in the bolometric lighcurves could possibly be explained by differences in the mass and distribution of ejected ^{56}Ni this is not fully satis-
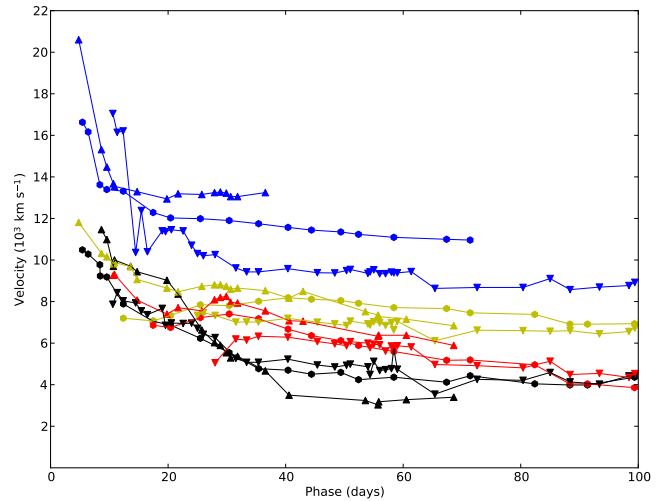
Fig. 18. Velocity evolution of the absorption minimum for the Fe II 5169 Å (black), He I 5876 Å (yellow), He I 6678 Å (red) and Hα (blue) lines for SNe 2011dh (circles), 2008ax (upward triangles) and 1993J (downward triangles) measured as described in Sect. 3.4.

factory as the mass of ejected ^{56}Ni is known from observations to be correlated with initial mass and expansion velocity (Fraser et al. 2011; Maguire et al. 2012). In all the observed characteristic of the SNe does not seem entirely consistent and we have to consider the possibility that the adopted distances and extinctions are in error.

Interestingly enough, it is possible to revise the extinctions alone, within the adopted error bars, in such a way that it brings the colour evolution, the bolometric luminosities and the peak-to-tail luminosity ratios in good agreement. This is shown in the right panels of Figures 14 and 15 where we have set $E(B-V)_T$ to 0.14, 0.09 and 0.27 mag for SNe 2011dh, 1993J and 2008ax respectively. Intrinsic differences among the SNe can not be excluded and the arguments used are only suggestive so we can not make a definite conclusion. It is clear, however, that a scenario where all three SNe have similar ejecta masses, explosion energies and ejected masses of ^{56}Ni is possible. As shown in B12 the differences in the early evolution and the velocities of lines originating further out in the ejecta could be explained by differences in the mass and radius of the hydrogen envelope. The progressively higher minimum velocities for the Hα absorption minimum, if interpreted as the interface between the helium core and the hydrogen envelope, would naively suggest progressively lower masses of this envelope for SNe 1993J, 2011dh and 2008ax respectively. Such a conclusion is supported by early photometric evolution, the strength and persistence of the Hα line, the hydrodynamical modelling of SNe 1993J and 2011dh in B12, the spectral modelling of SN 2011dh in this paper and by A11 and the spectral modelling of SN 2008ax by Maurer et al. (2010).

5. Discussion

In Sect. 5.1 we revisit the issue of extinction and discuss constraints from the SN itself and the comparisons to SNe 1993J and 2008ax made in Sect. 4.3. In Sect. 5.2 we discuss the physics of Type IIb lightcurves as understood from approximate models, in particular in relation to the hydrodynamical modeling made in B12. In Sect. 5.3 we discuss the sensitivity of the SN and progenitor parameters derived in B12 to errors in the distance,

extinction and photospheric velocity and also revise these parameters to agree with the distance and extinction adopted in this paper. In Sect. 5.4 we discuss the results on the disappearance of the progenitor star and what consequences this have for the results in M11 and B12 and our understanding of this star and Type IIb progenitors in general. Finally, in Sect. 5.5, we discuss the excess in the Spitzer 4.5 μm band and possible explanations.

5.1. Extinction revisited

In Sect. 1.3 we discussed different estimates of the extinction for SN 2011dh. Most estimates suggested a low extinction and we adopted $E(B\text{-}V)=0.07^{+0.07}_{-0.04}$ mag as estimated from the equivalent widths of the Na I D lines. The near simultaneous V and R band observations from day 1 presented in A11 and T12 corresponds to an intrinsic $V\text{-}R$ colour of about -0.2 mag for the adopted extinction. The bluest $V\text{-}R$ colour allowed for a blackbody, which can be calculated from the Rayleigh-Jeans law, is -0.16 mag so this suggests a very high temperature. In higher extinction scenarios this colour would be even bluer and, even taking measurement and calibration errors into account, in conflict with the bluest $V\text{-}R$ colour allowed for a blackbody. Figure 5 shows the evolution of the blackbody temperature for two higher extinction scenarios where we have increased $E(B\text{-}V)_{\mathrm{T}}$ in ~0.1 steps to 0.2 and 0.3 mag. As seen the blackbody temperature would become quite high between 10 and 20 days and we would expect lines from low ionization potential ions such as Ca II and Fe II to be quite sensitive to this. As shown in Fig. 10, the SN atmosphere code described in Sect. 3.4 can neither reproduce the Ca II 8498/8542/8662 Å lines, nor the the Fe II lines, between 10 and 20 days for these higher extinction scenarios. Even though NLTE effects may change the ion fractions, this again suggests a low extinction scenario for SN 2011dh. Comparisons to SNe 2008ax and 1993J provides another source of information. As discussed in Sect. 4 an assumption of similarity in luminosity and colour among the SNe requires a revision of the extinctions adopted in this paper and suggest a revision of the extinction for SN 2011dh towards the upper error bar. However, as pointed out, intrinsic differences among the SNe cannot be excluded and as such a revision would be within our error bars we do not find this argument sufficient to revise our adopted value.

5.2. Physic of Type IIb SNe lightcurves

The bolometric lightcurves of SN 2011dh and other Type IIb SNe can be divided in two distinct phases depending on the energy source powering the lightcurve. The first phase is powered by the thermal energy deposited in the ejecta by the explosion. The second phase is powered by the energy deposited in the ejecta by the γ-rays emitted in the radioactive decay chain of ^{56}Ni. In B12 we used the ^{56}Ni powered phase to estimate the ejecta mass, explosion energy and ejected mass of ^{56}Ni whereas the explosion energy powered phase was used to estimate the radius of the progenitor star.

The explosion energy powered phase ends at ~3 days when our observations begin but V R and g band data have been published in A11 and T12. These data are insufficient to construct a bolometric lightcurve but it is clear that this phase corresponds to a strong decline of the bolometric luminosity. As discussed in B12 the decline is caused by cooling, both by expansion and radiative diffusion, depends on the mass and radius of the hydrogen envelope and requires detailed hydrodynamical modelling.

The subsequent ^{56}Ni powered phase is well covered by our data and the bolometric lightcurve (Fig. 7) shows the characteristics common to all Type I and IIb SNe; a rise to peak luminosity followed by a decline phase and a subsequent tail phase with a roughly linear decline rate. These characteristics can be qualitatively understood by approximate models such as the ones by Arnett (1982) or Imshennik & Popov (1992). The rising phase is caused by radiative diffusion of the energy deposited in the ejecta by the γ-rays. The radioactive heating decreases with time and so does the diffusion time because the ejecta are expanding. As shown by Arnett (1982) the luminosity peak is reached when the radioactive heating equals the cooling by radiative diffusion. During the subsequent decline phase the diffusion time continues to decrease until the SN reaches the tail phase where the diffusion time is negligible and the luminosity equals the radioactive heating (instant diffusion). The shape of the tail is not exactly linear but is modulated by a term determined by the decreasing optical depth for γ-rays as the ejecta continue to expand.

From approximate models the qualitative dependence of the bolometric lightcurve in the ^{56}Ni powered phase on basic parameters as the explosion energy, ejecta mass and mass of ejected ^{56}Ni can be understood. Increasing the explosion energy will increase the expansion velocities which will decrease the diffusion time for thermal radiation and the optical depth for γ-rays. Increasing the ejecta mass will have the opposite effect but, as the optical depth $\tau \propto (M^2/E)$ and the diffusion time $t_{\mathrm{d}} \propto (M^3/E)^{1/4}$ (Arnett 1982), the bolometric lightcurve depends stronger on the ejecta mass than on the explosion energy. Either an increase of the explosion energy or a decrease of the ejecta mass will result in an earlier and more luminous peak of the bolometric lightcurve whereas the tail luminosity will be decreased. Increasing the mass of ^{56}Ni will increase the radioactive heating and thus result in an overall increase of the luminosity and in fact corresponds to a pure scaling in the approximate models. The distribution of ^{56}Ni also affects the lightcurve and if the ^{56}Ni is distributed further out in the ejecta the lightcurve will rise faster to the peak because of the decreased diffusion time for thermal radiation and have a lower luminosity on the tail because of the decreased optical depth for γ-rays. As shown in figures 2, 4, 5 and 6 in B12 all these qualitative dependencies are well followed by the hydrodynamical models.

If the optical depth for γ-rays in the tail phase is high the shape of the bolometric lightcurve in the ^{56}Ni powered phase depends exclusively on the diffusion time for thermal radiation, which determines the quantity (M^3/E), and the ejecta mass and explosion energy become degenerate. In this case knowledge of the expansion velocity, which determines the quantity (M/E), is needed to determine the SN parameters. However, as seen in Fig. 19, the optical depth for γ-rays becomes $\lesssim 1$ at ~40 days for SN 2011dh. The bolometric lightcurve in the tail phase then depends on the optical depth for γ-rays, which determines the quantity (M^2/E), and provides the constraint needed to break the degeneracy. However, as the bolometric lightcurve also depends on the distribution of ^{56}Ni the problem is not necessarily well-conditioned. In our experience, knowledge of the expansion velocity, which corresponds to the fitting of photospheric velocities in B12, is needed to robustly determine the SN parameters.

5.3. Error sensitivity and revisions of the B12 modelling

What was not discussed in B12 was the sensitivity of the results to errors in the adopted distance and extinction. A change in the distance corresponds to a scaling of the bolometric lightcurve
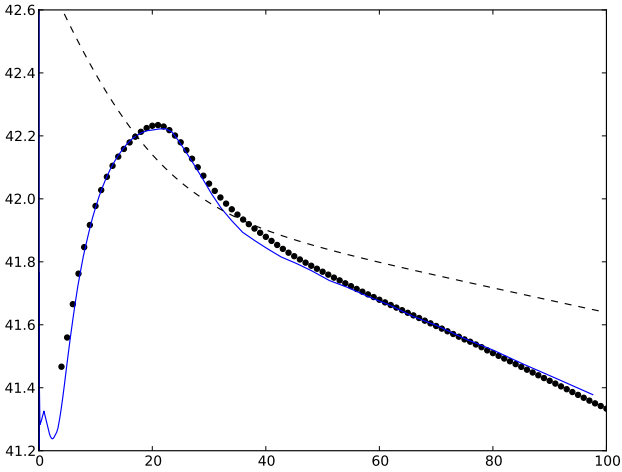
Fig. 19. Revised B12 He4 model bolometric lightcurve with the ^{56}Ni mass increased to 0.075 M$_\odot$ (blue solid line) compared to the pseudo-bolometric UV-MIR lightcurve for SN 2011dh calculated with the spectroscopic method (black dots). For comparison we also show the total γ-ray luminosity corresponding to this amount of ^{56}Ni (black dashed line).

whereas a change in the extinction is more complicated as the change in luminosity also depends on the colour. However, as seen in Fig. 7, the change in luminosity for SN 2011dh due to the combined errors in distance and extinction does not differ significantly from a scaling. As the adopted distance and extinction have been revised as compared to B12 we also need to investigate the effect of this change on the derived quantities.

In the ^{56}Ni powered phase, according to approximate models, the luminosity is proportional to the mass of ejected ^{56}Ni (Sect. 5.2). Therefore, ignoring possible degeneracy among the parameters, we expect the derived ejecta mass and explosion energy to be insensitive to the errors in the distance and extinction and the error in the derived mass of ejected ^{56}Ni to be similar to the error in the luminosity. We have re-run the He4 model with the ^{56}Ni mass increased to 0.075 M$_\odot$ to account for the revisions in the adopted distance and extinction. The model bolometric lightcurve is shown in Fig. 19 and well reproduces the bolometric lightcurve presented in this paper. Estimating the errors arising from the distance and extinction as described the revised mass of ejected ^{56}Ni becomes 0.05-0.10 M$_\odot$ whereas the ejecta mass and explosion energy remains the same as in B12, 1.8-2.5 M$_\odot$ and 0.6-1.0$\times10^{51}$ erg respectively.

In the explosion energy powered phase, according to approximate models, the luminosity is proportional to the radius. However, the lightcurve in this phase is not well described by approximate models and detailed hydrodynamical modelling is needed (Sect. 5.2). As discussed in B12 the sensitivity of the estimated radius to changes in the luminosity is modest. Examining the range of envelope models consistent with the A11 g band observations, the distance and extinction adopted in this paper and the systematic error arising from these we find a revised progenitor radius of 200-300 R$_\odot$.

As discussed in Sect. 3.4 the region where the Fe II 5169 Å line is formed rather provides an upper limit for the location of the photosphere and the photospheric velocities used in the hydrodynamical modelling might therefore be overestimated. The dependence of the derived quantities on the photospheric velocity is complicated and a full scan of the model parameter space is probably needed to make a quantitative estimate. This is a po-

tential problem and further work is needed to well constrain the photospheric velocities.

5.4. Disappearance of the proposed progenitor star

In Ergon et al. (2013) we presented observations of the SN site obtained on Jan 20 2013 (V and r) and Mar 19 2013 (B), 601 and 659 days past explosion respectively. Additional V band imaging was obtained on Apr 14 2013, 685 days past explosion. In Appendix B we give the details on these observations and the photometric measurements and calibration. Subtraction of pre-explosion images shows that the flux from the yellow supergiant proposed as the progenitor by M11 have been reduced with at least 58±3, 73±5 and 60±3 percent in the B, V and r bands respectively. The HST observations obtained on Mar 2 2013 and presented by Van Dyk et al. (2013) corresponds to a reduction of the flux of 71±1 and 70±1 in the $F555W$ and $F814W$ bands respectively. Szczygieł et al. (2012) find the progenitor to be variable at the five percent level so variability of the star is unlikely to explain the flux reduction. We find a 0.76 mag decline in the V band between Jan 20 and Apr 14 2013 which is consistent with the remaining flux being emitted by the SN. As can be derived from the approximate models discussed in Sect. 5.2, in the limit of low optical depth for the γ-rays and if all positrons are trapped, the decline rate is $(1 + (1 - f_{e^+}(t))\,223/t)\,0.0098$ mag day^{-1}, where $f_{e^+}(t)$ is the fractional positron contribution to the luminosity and t is given in days. This gives an expected decline of 0.8-1.1 mag between 601 and 685 days for SN 2011dh, depending on the contribution from positrons, in reasonable agreement with the observed value. Given all this, although we can not exclude a minor contribution to the pre-explosion flux from other sources, we find that the yellow supergiant has disappeared. The only reasonably explanation is that the star was the progenitor of SN 2011dh as originally proposed in M11.

The disappearance of the yellow supergiant confirms the results in B12 in which we showed that an extended progenitor with the observed properties of the yellow supergiant could well reproduce the early optical evolution. This shows that the duration of the initial cooling phase for a SN with an extended progenitor can be significantly shorter than commonly thought and that approximate models as the one by Rabinak & Waxman (2011) used in A11 does not necessarily apply. It also indicates that the proposed division of Type IIb SNe progenitors in compact and extended ones and the relation between the speed of the shock and the type of progenitor (Chevalier & Soderberg 2010) needs to be revised. It is interesting to note that the two progenitors of Type IIb SNe (1993J and 2011dh) whose nature have been revealed were in both cases extended supergiants. The disappearance of the yellow supergiant in M51 was a major step in achieving one of our main goals, to determine the initial mass of the progenitor star. This mass has now been estimated to ~13 M$_\odot$ by two different methods, the hydrodynamical modelling in B12 and the progenitor analysis in M11, respectively. Both methods use results from stellar evolutionary modelling to relate the He core mass and the progenitor luminosity respectively to the initial mass but are otherwise independent. We note that, contrary to most other types, the initial mass of Type IIb SNe progenitors might be derived from hydrodynamical modelling without any assumptions of uncertain mass-loss rates as the star is essentially a bare He core (although with a thin and extended envelope).

5.5. 4.5 μm excess

As mentioned in Sections 3.1 and 3.3 there is a flux excess in the Spitzer 4.5 μm band as compared to the 2MASS *JHK* and Spitzer 3.6 μm bands developing during the first 100 days. This is most clearly seen in Fig. 9. Whereas other bands redward of *V* are well approximated by the blackbody fits the flux at 4.5 μm is a factor of ~5 in excess at 100 days. Warm dust or CO fundamental band emission are two possible explanations. For day 50-100 the excess is well fitted by a blackbody with T≃400 K, R≃5×10^{16} cm and L≃6×10^{40} erg. A shock speed of ~20000 km s^{-1} (Bietenholz et al. 2012) corresponds to a radius of ~2 × 10^{16} cm at 100 days so it seems like such dust must have formed in the CSM before the explosion where we expect it would have been evaporated by the SN. Therefore we favour CO fundamental band emission as the explanation. There is also a possible excess (as compared to the continuum) developing near the location of the first overtone band at ~23000 Å. NIR spectra from later epochs may help to resolve this issue as we expect first overtone emission to grow stronger as compared to the continuum.

6. Conclusions

We present extensive photometric and spectroscopic optical and NIR observations of SN 2011dh obtained during the first 100 days. The calibration of the photometry is discussed in some detail and we find it to be accurate to the five percent level in all bands. Using our observations as well as SWIFT UV and Spitzer MIR observations we calculate the bolometric UV-MIR lightcurve using both photometric and spectroscopic data. This bolometric lightcurve together with the photospheric velocity as estimated from the absorption minimum of the Fe II 5169 Å line provides the observational basis for the hydrodynamical modelling done in B12.

We derive a distance of 7.8$^{+1.1}_{-0.9}$ Mpc based on all estimates in the literature and find an extinction of $E(B-V)_{\rm T}$=0.07$^{+0.07}_{-0.04}$ mag to be consistent with estimates and constraints presented in the literature and in this paper. The sensitivity of the results in B12 to these uncertainties is discussed and we find that only the derived mass of ejected ^{56}Ni and radius is likely to be affected. We also revise the modelling made in B12 to agree with the values of the distance and extinction adopted in this paper and find that only the derived mass of ejected ^{56}Ni and radius needs to be revised. The uncertainty in the photospheric velocity as estimated from the absorption minimum of the Fe II 5169 Å line is discussed and we find that we can not constrain this velocity very well. This is a potential problem as we are unable to quantify the sensitivity of the results in B12 to this uncertainty.

We present and discuss pre- and post-explosion observations which shows that the yellow supergiant coincident with SN 2011dh has disappeared and indeed was the progenitor as proposed in M11. Furthermore, the results from the progenitor analysis in M11 are consistent with those from the hydrodynamical modelling in B12. Given the revisions in this paper, we find that an almost bare helium core with a mass of 3.3-4.0 M$_{\odot}$ surrounded by a thin hydrogen rich envelope extending to 200-300 R$_{\odot}$ exploded with an energy of 0.6−1.0 ×10^{51} erg ejecting a mass of 1.8-2.5 M$_{\odot}$ of which 0.05-0.10 M$_{\odot}$ consisted of synthesised ^{56}Ni.

The absorption minimum of the hydrogen lines is never seen below ~11000 km s^{-1} but approaches this value when the lines get weaker. Spectral modelling of the hydrogen lines using the B12 He4R270 ejecta model well reproduce this behaviour and the minimum velocity of the absorption minima coincides with

the model interface between the helium core and the hydrogen rich envelope. The good agreement between the modelled and observed minimum velocities gives support to the B12 He4R270 ejecta model and we find it most likely that the interface between the helium core and the hydrogen rich envelope is located at ~11000 km s^{-1}. We note that the minimum velocity of the Hα absorption minimum for SNe 1993J, 2011dh and 2008ax is ~9000, ~11000 and ~13000 km s^{-1} respectively which suggest that the interface between the helium core and the hydrogen rich envelope is located near these progressively higher velocities. By varying the fraction of hydrogen in the envelope we find a hydrogen mass of 0.01-0.04 M$_{\odot}$ to be consistent with the observed evolution of the hydrogen lines. This is in reasonable agreement with the 0.02 M$_{\odot}$ in the original model and the 0.024 M$_{\odot}$ estimated by A11 using spectral modelling similar to the one in this paper. We estimate that the photosphere reaches the interface between the helium core and the hydrogen rich envelope at 5-7 days whereas the He I 10830 and 5876 Å lines appear at ~10 days and the He I 6678, 7065 and 20581 Å lines at ~15 days. They all appear close to the region where we expect the photosphere to be located and then move outward in velocity until ~40 days. This suggests that the early evolution of these lines is driven by increasing non-thermal excitation due to decreasing optical depth for the γ-rays.

The photometric and spectral characteristics of SNe 2011dh, 1993J and 2008ax is compared and we find the colours and luminosities to differ significantly for the distances and extinctions adopted in this paper. However, the errors arising from the distance and extinction are large and a revision of the extinctions, just within the error bars, would bring the colours and luminosities in good agreement. Although a definite conclusion can not be made it is clear that a scenario where all three SNe have similar ejecta masses, explosion energies and ejected masses of ^{56}Ni is possible. As shown in B12 the differences in the early evolution could be explained by differences in the mass and radius of the hydrogen envelope. Progressively higher velocities of the interface between the helium core and the hydrogen rich envelope, as proposed above, would naively correspond to progressively lower masses of this envelope for SNe 1993J, 2011dh and 2008ax respectively. Such a conclusion is supported by the early photometric evolution, the strength and persistence of the Hα line and hydrodynamical as well as spectral modelling of these SNe.

We detect a flux excess in the 4.5 μm Spitzer band as compared to the NIR and the 3.6 μm Spitzer band and discuss possible explanations. As dust emission requires a blackbody radius larger than that of the ejecta and we expect pre-existing CSM dust to have been evaporated by the SN we favour CO fundamental band emission as the explanation.

The high quality dataset presented in this paper provides an ideal base for further modelling of the SN. One of the most interesting issues which remains unsolved is the possible existence of a bluer and more compact companion star as predicted by the binary evolutionary modelling in Benvenuto et al. (2013). It is still not clear which of the single or binary star channels is dominating the production of Type IIb SNe. HST imaging, preferably in the UV, would have a good chance to detect such a companion.

7. Acknowledgements

Appendix A: Photometric calibration

The optical photometry was tied to the Johnson-Cousins (JC) and Sloan Digital Sky Survey (SDSS) systems. The NIR photometry was tied to the 2 Micron All Sky Survey (2MASS) system. Table A.1 lists the filters used at each instrument and the mapping of these to the standard systems. Note that we have used JC-like $UBVRI$ filters and SDSS-like gz filters at NOT whereas we have used JC-like BV filters and SDSS-like $ugriz$ filters at LT and FTN. The JC-like URI and SDSS-like uri photometry were then tied to both the JC and SDSS systems to produce full sets of JC and SDSS photometry. The SWIFT photometry was tied to the natural (photon count based) Vega system although the SWIFT UBV photometry was also tied to the JC system for comparison. The Spitzer photometry was tied to the natural (energy flux based) Vega system.

Appendix A.1: Calibration method

The SN photometry was calibrated using reference stars within the SN field. These reference stars, in turn, were calibrated using standard fields. The calibration was performed using the SNE pipeline. To calibrate the SN photometry we fitted transformation equations of the type $m_i^{sys} = m_i^{ins} + C_{i,jk}(m_j^{sys} - m_k^{sys}) + Z_i$, where m_i^{sys}, m_i^{ins} and Z_i are the system and instrumental magnitudes and the zeropoint for band i respectively and $C_{i,jk}$ is the colour-term coefficient for band i using the colour jk. The magnitudes of the SN was evaluated both using these transformation equations and by the use of S-corrections. In the latter case the linear colour-terms are replaced by the S-corrections as determined from the SN spectra and the filter response functions of the natural systems of the instruments and the standard systems. We will discuss S-corrections in Appendix A.5 and compare the results from the two methods. In the end we have decided to use the S-corrected photometry for all bands except the JC U and SDSS u bands. To calibrate the reference star photometry we fitted transformation equations of the type $m_i^{sys} = m_i^{ins} + C_{i,jk}(m_j^{sys} - m_k^{sys}) + Z_i + e_i X_i$, where X_i and e_i are the airmass and the extinction coefficient for band i respectively. The magnitudes of the reference stars were evaluated using these transformation equations and averaged using a magnitude error limit (0.05 mag) and mild (3 σ) rejection. Both measurement errors and calibration errors in the fitted quantities were propagated using standard methods. The errors in the reference star magnitudes were calculated as the standard deviation of all measurements corrected for the degrees of freedom.

The coefficients of the linear colour terms ($C_{i,jk}$) used to transform from the natural system of the instruments to the JC and SDSS standard systems were determined separately. For each instrument, system and band we determined the coefficient by least-square fitting of a common value to a large number of observations. For the NOT and the LT we also fitted the coefficients of a cross-term between colour and airmass for U and B to correct for the change in the filter response functions due to the variation of the extinction with airmass. However, given the colour and airmass range spanned by our observations, the correction turned out to be at the few-percent level and we decided to drop it. Because of the lower precision in the 2MASS catalogue as compared to the Landolt and SDSS catalogues we could not achieve the desired precision in measured 2MASS colour-term coefficients. Therefore we have used synthetic colour terms computed for a blackbody SED using the NIR filter response functions described in Sect. A.5. The measured JC and SDSS and synthetic 2MASS colour-term coefficients determined for each instrument are listed in Tables A.2-A.4.

Appendix A.2: JC calibration

The optical photometry was tied to the JC system using the reference stars presented in Pastorello et al. (2009, hereafter P09)
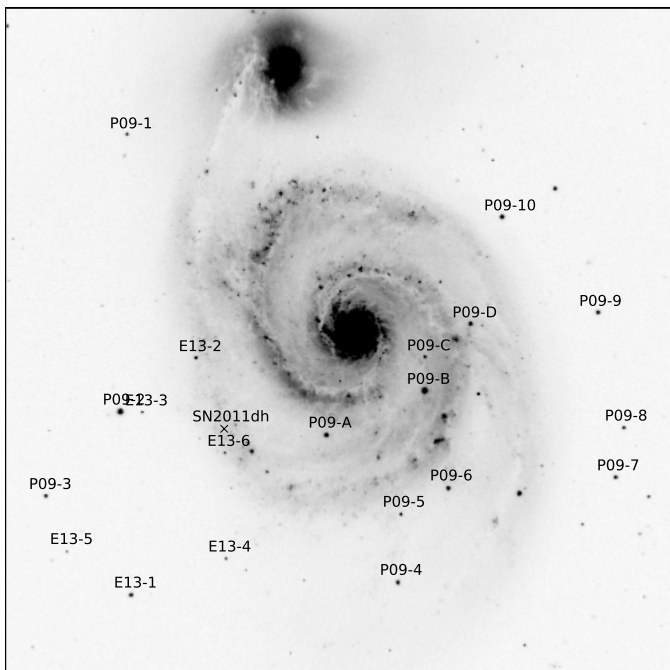
Fig. A.1. Reference stars used for calibration of the optical photometry marked on a SDSS *r* band image.

as well as a number of additional fainter stars close to the SN. In the following the reference stars from P09 will be abbreviated as P09-N and those added in this paper as E13-N. Those reference stars, in turn, have been tied to the JC system using standard fields from Landolt (1983, 1992). Taking advantage of the large number of standard star observations obtained with the LT we have re-measured the magnitudes of the P09 reference stars within the LT field of view (FOV). The mean and root mean square (RMS) of the difference was at the few-percent level for the *B*, *V*, *R* and *I* bands and at the 10-percent level for the *U* band except for P09-3 which differed considerably. We have also re-measured the magnitudes of the Landolt standard stars and the mean and RMS of the difference was at the few-percent level in all bands. This shows that, in spite of the SDSS-like nature of the LT *u*, *r* and *i* filters, the natural LT photometry transform to the JC system with good precision. In the end we chose to keep the P09 magnitudes, except for P09-3, and use the LT observations as confirmation. The magnitudes of the additional reference stars and P09-3 were determined using the remaining P09 reference stars and large number of deep, high quality NOT images of the SN field. The coordinates and magnitudes of the JC reference stars are listed Table A.5 and their positions marked in Fig. A.1.

Appendix A.3: SDSS calibration

The optical photometry was tied to the SDSS system using the subset of the reference stars within the LT FOV. Those reference stars, in turn, have been tied to the SDSS system using fields covered by the SDSS DR8 catalogue (Aihara et al. 2011). The calibration was not straightforward as the SN field and a number of the LT standard fields were not well covered by the catalogue and many of the brighter stars in the fields covered by the catalogue were marked as saturated in the *g*, *r* and *i* bands. The procedure used to calibrate the reference star magnitudes was as follows. First we re-measured the *g*, *r* and *i* magnitudes for all stars marked as saturated using the remaining stars in the

LT standard fields covered by the catalogue. We then measured the magnitudes for the stars in the fields not covered by the catalogue and finally we measured the reference star magnitudes using all the LT standard field observations. For reference, our measured SDSS magnitudes for the LT standard fields are listed in Table A.6. Magnitudes of stars covered by the catalogue and not marked as saturated were adopted from the catalogue. The coordinates and the magnitudes of the SDSS reference stars are listed in Table A.7 and their positions marked in Fig. A.1. The magnitudes of P09-3, E13-1 and E13-5 were adopted from the catalogue. The mean and RMS of the difference between measured and catalogue magnitudes for stars with measured and catalogue errors less than 5 percent was less than 5 percent in all bands.

Appendix A.4: 2MASS calibration

The NIR photometry was tied to the 2MASS system using all stars within 7 arc minutes distance from the SN with *J* magnitude brighter than 18.0 detected in deep UKIRT imaging of the SN field. This includes the optical reference stars as well as ~50 additional stars, although for most observations the small FOV prevented use of more than about 10 of these. Those reference stars, in turn, have been tied to the 2MASS system using all stars from the 2MASS Point Source catalogue (Skrutskie et al. 2006) with *J* magnitude error less than 0.05 mag within the 13.65×13.65 arc minute FOV. The coordinates and magnitudes for the 2MASS reference stars are listed in Table A.8. Magnitudes of stars covered by the catalogue and with errors less than 0.05 were adopted from the catalogue. The mean and RMS of the difference between measured and catalogue magnitudes for stars with measured and catalogue errors less than 5 percent was less than 5 percent in all bands.

Appendix A.5: S-corrections

From the above and the fact that a fair (usually 5-10) number of reference stars were used we conclude that the calibration of the JC, SDSS and 2MASS photometry, with the possible exception of the *U* band, should be good to the few-percent level as long as a linear colour-correction is sufficient to transform to the standard systems. This is known to work well for stars, but is not necessarily true for SNe. Photometry for well monitored SNe as 1987A and 1993J shows significant differences between different datasets and telescopes, in particular at late times, as might be expected by the increasingly line-dominated nature of the spectrum. A more elaborate method to transform from the natural system to the standard system is S-corrections (Stritzinger et al. 2002). Using this method we first transform the reference star magnitudes to the natural system using linear colour-terms and then transform the SN magnitudes to the standard system by replacing the linear colour-terms with S-corrections calculated as the difference of the synthetic magnitudes in the standard and natural systems. Note that this definition differs from the one by Stritzinger et al. (2002) but is the same as used by Taubenberger et al. (2011). Success of the method depends critically on the accuracy of the filter response functions and a well sampled spectral sequence.

For all telescopes we constructed optical filter response functions from filter and CCD data provided by the observatory or the manufacturer and extinction data for the site. Extinction data for Roque de los Muchachos at La Palma where NOT, LT, TNG and WHT are located where obtained from the Isaac Newton Group

of Telescopes (ING). A typical telluric absorption profile, as determined from spectroscopy, was also added to the filter response functions. We have assumed that the optics response functions vary slowly enough not to affect the S-corrections. To test this we constructed optics response functions for a number of telescopes from filter zeropoints, measured from standard star data or provided by the observatories. Except below ~4000 Å they vary slowly as expected and applying them to our data the S-corrections vary at the percent level or less so the assumption seems to be justified. Below ~4000 Å the optics response functions may vary rapidly and because of this and other difficulties in this wavelength region wave have not applied S-corrections to the JC U and SDSS u bands. To test the constructed JC and SDSS filter response functions we compared synthetic colour-term coefficients derived from the STIS NGSL[4] spectra with observed colour-term coefficients and the agreement was generally good. However, for those filters were the synthetic and observed colour-term coefficients deviated the most, we adjusted the response functions by small wavelength shifts (typically between 50 and 100 Å). This method is similar to the one applied by S11 and, in all cases, improved the agreement between S-corrected photometry from different telescopes. As we could not measure the 2MASS colour-term coefficients with sufficient precision this method could not be applied to the NIR filters.

Appendix A.6: Systematic errors

The difference between the S-corrected and colour-corrected JC, SDSS and 2MASS photometry is shown in Figures A.2-A.4. The differences are mostly less than 5 percent but approaches 10 percent in some cases. Most notably, the difference for the late CA 3.5m J band observation is ~30 percent because of the strong He 10830 Å line. So even if the differences are mostly small, S-corrections seems to be needed to achieve 5 percent accuracy in the photometry.

A further check of the precision in the photometry is provided by comparison to the A11, V12, T12, M13 and, in particular, the SWIFT photometry. The SWIFT photometry was transformed to the JC system using S-corrections calculated from the SWIFT filter response functions, which are well known and not affected by the atmosphere. The differences between the JC photometry for all datasets and a spline fit to all but the A11 WISE 1m and M13 datasets is shown in Fig. A.5. The systematic (mean) difference is less than ~5 percent in all bands except for the A11 WISE 1m and M13 datasets which shows systematic (mean) differences of ~20 percent. As seen in Fig. A.5 as well as Fig. 1 the agreement between the NOT, LT and SWIFT B and V band photometry is excellent. This gives confidence in the method used. Except for the early NOT photometry, the agreement between the NOT, LT and SWIFT U band photometry is good as well.

Appendix A.7: Synthetic photometry

Synthetic photometry (used for e.g. S-corrections) was calculated as energy flux based magnitudes in the form $m_i = \int F_\lambda S_{\lambda,i} d\lambda / \int S_{\lambda,i} d\lambda + Z_i$, where $S_{\lambda,i}$ and Z_i is the energy response function (BM12) and zeropoint of band i respectively. Note that filter response functions are commonly given as photon response functions (BM12) and then have to be multiplied with wavelength to give the energy response functions. JC fil-
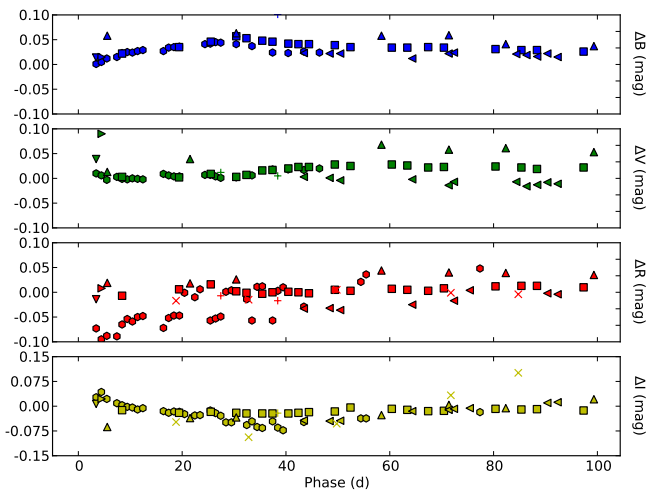
Fig. A.2. Difference between JC colour- and S-corrected photometry for NOT (squares), LT (circles), CA 2.2m (upward triangles), TNG (downward triangles), AS 1.82m (rightward triangles), AS Schmidt (leftward triangles), TJO (pluses) and FTN (crosses).
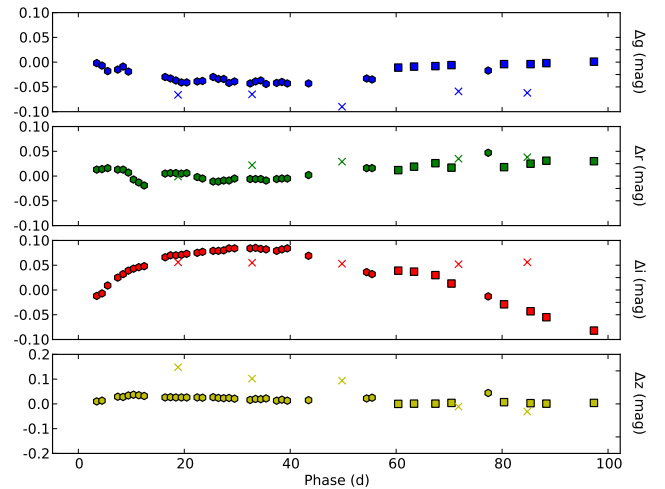
Fig. A.3. Difference between SDSS colour- and S-corrected photometry for NOT (squares), LT (circles) and FTN (crosses).

ter response functions have been adopted from BM12 and zeropoints calculated using the Vega spectrum and JC magnitudes. SDSS filter response functions have been adopted from Doi et al. (2010) and zeropoints calculated using the definition of AB magnitudes (Oke & Gunn 1983) and small corrections following the instructions given at the SDSS site. 2MASS filter response functions have been adopted from Cohen et al. (2003) as provided by the Explanatory Supplement to the 2MASS All Sky Data Release and Extended Mission Products. SWIFT filter response functions have been adopted from Poole et al. (2008) as provided by the SWIFT calibration database. To transform the photon count based SWIFT system into an energy flux based system we have multiplied the response functions with wavelength and re-normalized. The zeropoints were then calculated using the Vega spectrum and SWIFT magnitudes (Poole et al. 2008). Spitzer filter response functions have been adopted from Hora et al. (2008) as provided at the Spitzer web site and zeropoints calculated using the Vega spectrum and Spitzer magnitudes.
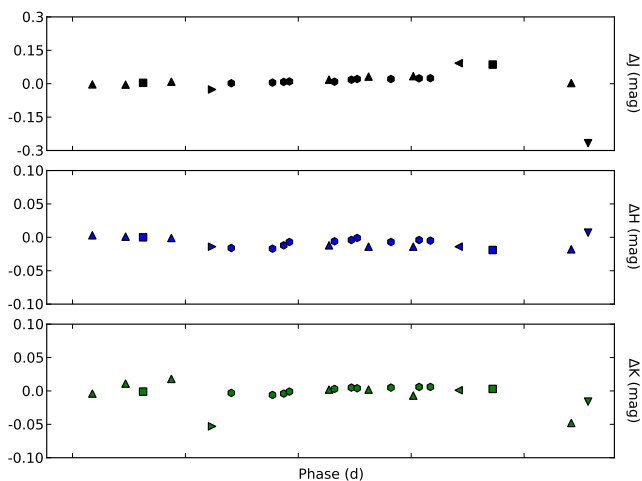
Fig. A.4. Difference between 2MASS colour- and S-corrected photometry for NOT (squares), TCS (circles), TNG (upward triangles), CA 3.5m (downward triangles), WHT (rightward triangles) and LBT (leftward triangles).
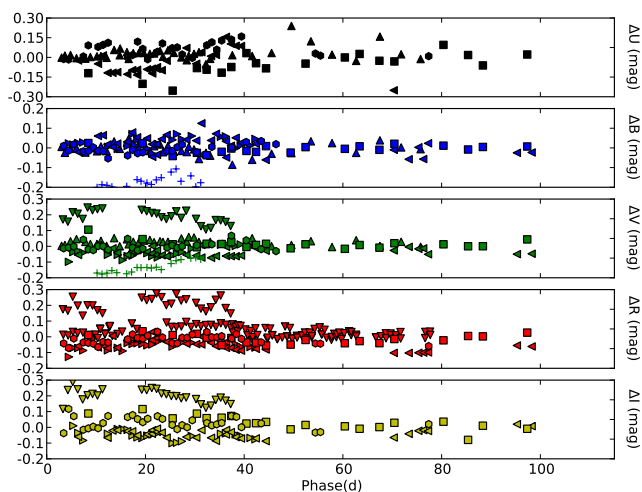
Fig. A.5. Difference between JC photometry for the NOT (squares), LT (circles), SWIFT (upward triangles), A11 (downward triangles), V12 (rightward triangles), T12 (leftward triangles) and M13 (pluses) datasets and a cubic spline fit to all but the A11 WISE 1m and M13 datasets.

Appendix A.8: SWIFT UV read leak

Finally we note that the response functions of the SWIFT $UVW1$ and $UVW2$ filters have a quite strong red tail. If, as is often the case for SNe, there is a strong blueward slope of the spectrum in the UV region this will result in a red leakage that might even dominate the flux in these filters. In Fig. A.6 we quantify this by showing the fractional red leakage defined as the fractional flux more than half the equivalent width redwards of the mean energy wavelengths of the filters. The spectrum was interpolated from the photometry as explained in Sect. 3.3 excluding the $UVW1$ and $UVW2$ filters. After ~20 days the leakage is ~80 and ~60 percent in the $UVW1$ and $UVW2$ filters respectively. Given this the $UVW1$ and $UVW2$ lightcurves do not reflect the evolution of the spectrum at their mean energy wavelengths and we will therefore exclude these from the analysis and when calculating the bolometric lightcurve in Sect. 3.3.
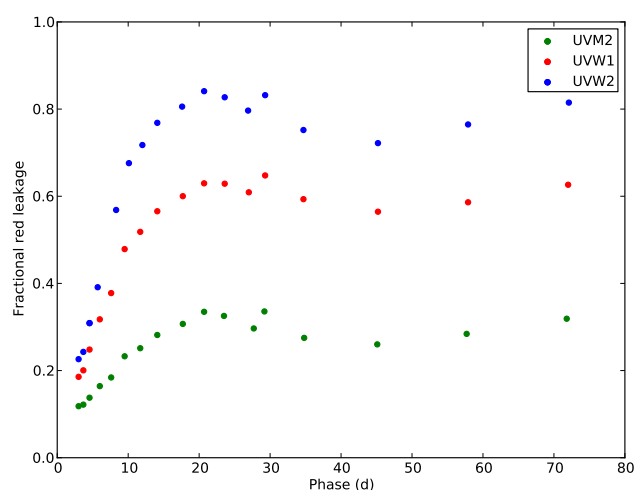
Fig. A.6. Fractional red leakage in the SWIFT $UVW1$, $UVM2$ and $UVW2$ filters.

Appendix B: Progenitor observations

We have obtained high quality pre- and post-explosion B, V and r band images of the SN site with the NOT. The pre-explosion images were obtained on May 26 2008 (B) and May 29 2011 (V and r), the latter just 2 days before the explosion. The post-explosion images were obtained on Jan 20 2013 (V and r), Mar 19 2013 (B) and Apr 14 2013 (V), 601, 659 and 685 days post explosion respectively. In Fig. B.1 we show a colour composite of the pre- and post-explosion B, V and r band images where the RGB values have been scaled to match the number of photons. The photometry presented below have been calibrated to the natural Vega (BV) and AB (r) systems of the NOT using the reference star magnitudes and colour constants presented in this paper (Tables A.5, A.7, A.2 and A.3).

We have used the HOTPANTS package to perform subtractions of the pre- and post-explosion images and aperture photometry to measure the magnitudes of the residuals to $B=23.00\pm0.10$, $V=22.73\pm0.07$ (Jan 20 2013), $V=22.23\pm0.05$ (Apr 14 2013) and $r=22.22\pm0.05$ mag. The positions of the residuals in all bands are within 0.15 arcsec from the position of the SN. The two fainter nearby stars, seen in pre-explosion HST images, that could possibly contaminate the result are ~0.5 arcsec away from the SN so their contribution to the residuals is likely to be small. Using PSF photometry where we have iteratively fitted the PSF subtracted background we measure the magnitudes of the yellow supergiant in the pre-explosion images to $B=22.41\pm0.12$, $V=21.89\pm0.04$ and $r=21.67\pm0.03$ mag. The residuals then corresponds to a reduction of the flux with 58±8, 46±3 (Jan 20 2013), 73±(4) (Apr 14 2013) and 60±3 percent in the B, V and r bands. The remaining flux, at least partly emitted by the SN, corresponds to $B=23.35\pm0.32$, $V=22.56\pm0.10$ (Jan 20 2013), $V=23.32\pm0.20$ (Apr 14 2013) and $r=22.67\pm0.11$ mag.

References

Aihara, H., Allende Prieto, C., An, D., et al. 2011, ApJS, 193, 29
Arcavi, I., Gal-Yam, A., Yaron, O., et al. 2011, ApJ, 742, L18
Arnett, W. D. 1982, ApJ, 253, 785
Baron, E., Branch, D., & Hauschildt, P. H. 2007, ApJ, 662, 1148
Baron, E., Hauschildt, P. H., Branch, D., Kirshner, R. P., & Filippenko, A. V. 1996, MNRAS, 279, 799
Benvenuto, O. G., Bersten, M. C., & Nomoto, K. 2013, ApJ, 762, 74
Bersten, M. C., Benvenuto, O. G., Nomoto, K., et al. 2012, ApJ, 757, 31
Bessell, M. & Murphy, S. 2012, PASP, 124, 140
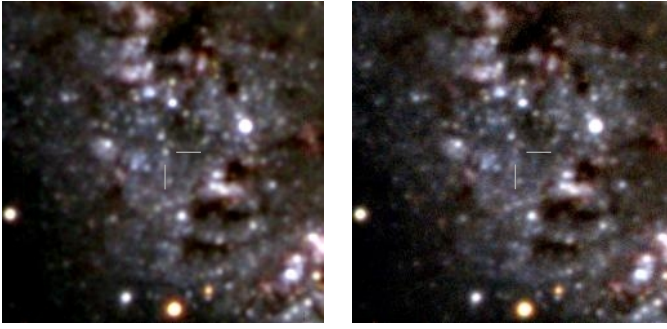
Fig. B.1. Colour composite of the pre- (left panel) and post- (right panel) explosion NOT imaging. The RGB values have been scaled to match the number of photons.

Bietenholz, M. F., Brunthaler, A., Soderberg, A. M., et al. 2012, ApJ, 751, 125

Blinnikov, S. I., Eastman, R., Bartunov, O. S., Popolitov, V. A., & Woosley, S. E. 1998, ApJ, 496, 454

Bowen, D. V., Roth, K. C., Blades, J. C., & Meyer, D. M. 1994, ApJ, 420, L71

Branch, D., Baron, E. A., & Jeffery, D. J. 2003, Supernovae and Gamma-Ray Bursters, 598, 47

Campana, S. & Immler, S. 2012, MNRAS, 427, L70

Cardelli, J. A., Clayton, G. C., & Mathis, J. S. 1989, ApJ, 345, 245

Chevalier, R. A. & Soderberg, A. M. 2010, ApJ, 711, L40

Chornock, R., Filippenko, A. V., Li, W., et al. 2011, ApJ, 739, 41

Ciardullo, R., Feldmeier, J. J., Jacoby, G. H., et al. 2002, ApJ, 577, 31

Cohen, M., Wheaton, W. A., & Megeath, S. T. 2003, AJ, 126, 1090

Crockett, R. M., Eldridge, J. J., Smartt, S. J., et al. 2008, MNRAS, 391, L5

Dessart, L., Blondin, S., Brown, P. J., et al. 2008, ApJ, 675, 644

Doi, M., Tanaka, M., Fukugita, M., et al. 2010, AJ, 139, 1628

Ergon, M., Sollerman, J., Pursimo, T., et al. 2013, The Astronomer's Telegram, 4912, 1

Feldmeier, J. J., Ciardullo, R., & Jacoby, G. H. 1997, ApJ, 479, 231

Fraser, M., Ergon, M., Eldridge, J. J., et al. 2011, MNRAS, 417, 1417

Georgiev, T. B., Getov, R. G., Zamanova, V. I., & Ivanov, G. R. 1990, Pis ma Astronomicheskii Zhurnal, 16, 979

Griga, T., Marulla, A., Grenier, A., et al. 2011, Central Bureau Electronic Telegrams, 2736, 1

Hora, J. L., Carey, S., Surace, J., et al. 2008, PASP, 120, 1233

Horesh, A., Stockdale, C., Fox, D. B., et al. 2012, ArXiv e-prints

Imshennik, V. S. & Popov, D. V. 1992, AZh, 69, 497

Iwamoto, K., Nomoto, K., Hoflich, P., et al. 1994, ApJ, 437, L115

Jerkstrand, A., Fransson, C., & Kozma, C. 2011, A&A, 530, A45

Jerkstrand, A., Fransson, C., Maguire, K., et al. 2012, A&A, 546, A28

Krauss, M. I., Soderberg, A. M., Chomiuk, L., et al. 2012, ApJ, 750, L40

Landolt, A. U. 1983, AJ, 88, 439

Landolt, A. U. 1992, AJ, 104, 340

Lewis, J. R., Walton, N. A., Meikle, W. P. S., et al. 1994, MNRAS, 266, L27

Lucy, L. B. 1991, ApJ, 383, 308

Maeda, K. 2012, ApJ, 758, 81

Maguire, K., Jerkstrand, A., Smartt, S. J., et al. 2012, MNRAS, 420, 3451

Marion, G. H., Vinko, J., Kirshner, R. P., et al. 2013, ArXiv e-prints

Martí-Vidal, I., Tudose, V., Paragi, Z., et al. 2011, A&A, 535, L10

Matthews, K., Neugebauer, G., Armus, L., & Soifer, B. T. 2002, AJ, 123, 753

Maund, J. R., Fraser, M., Ergon, M., et al. 2011, ApJ, 739, L37

Maund, J. R., Smartt, S. J., Kudritzki, R. P., Podsiadlowski, P., & Gilmore, G. F. 2004, Nature, 427, 129

Maurer, I., Mazzali, P. A., Taubenberger, S., & Hachinger, S. 2010, MNRAS, 409, 1441

Mazzali, P. A. & Lucy, L. B. 1993, A&A, 279, 447

Munari, U. & Zwitter, T. 1997, A&A, 318, 269

Murphy, J. W., Jennings, Z. G., Williams, B., Dalcanton, J. J., & Dolphin, A. E. 2011, ApJ, 742, L4

Oke, J. B. & Gunn, J. E. 1983, ApJ, 266, 713

Pastorello, A., Kasliwal, M. M., Crockett, R. M., et al. 2008, MNRAS, 389, 955

Pastorello, A., Valenti, S., Zampieri, L., et al. 2009, MNRAS, 394, 2266

Podsiadlowski, P., Hsu, J. J. L., Joss, P. C., & Ross, R. R. 1993, Nature, 364, 509

Poole, T. S., Breeveld, A. A., Page, M. J., et al. 2008, MNRAS, 383, 627

Poznanski, D., Butler, N., Filippenko, A. V., et al. 2009, ApJ, 694, 1067

Poznanski, D., Ganeshalingam, M., Silverman, J. M., & Filippenko, A. V. 2011, MNRAS, 415, L81

Poznanski, D., Prochaska, J. X., & Bloom, J. S. 2012, MNRAS, 426, 1465

Rabinak, I. & Waxman, E. 2011, ApJ, 728, 63

Richmond, M. W., Treffers, R. R., Filippenko, A. V., & Paik, Y. 1996, AJ, 112, 732

Richmond, M. W., Treffers, R. R., Filippenko, A. V., et al. 1994, AJ, 107, 1022

Ritchey, A. M. & Wallerstein, G. 2012, ApJ, 748, L11

Roming, P. W. A., Pritchard, T. A., Brown, P. J., et al. 2009, ApJ, 704, L118

Rosse, W. P. 1850, Philosophical Transactions of the Royal Society, 499

Sandage, X. & Tammann, X. 1974

Sasaki, M. & Ducci, L. 2012, A&A, 546, A80

Schlafly, E. F. & Finkbeiner, D. P. 2011, ApJ, 737, 103

Schlegel, D. J., Finkbeiner, D. P., & Davis, M. 1998, ApJ, 500, 525

Shigeyama, T., Suzuki, T., Kumagai, S., et al. 1994, ApJ, 420, 341

Skrutskie, M. F., Cutri, R. M., Stiening, R., et al. 2006, AJ, 131, 1163

Smartt, S. J., Eldridge, J. J., Crockett, R. M., & Maund, J. R. 2009, MNRAS, 395, 1409

Soderberg, A. M., Margutti, R., Zauderer, B. A., et al. 2012, ApJ, 752, 78

Stancliffe, R. J. & Eldridge, J. J. 2009, MNRAS, 396, 1699

Stanishev, V. 2007, Astronomische Nachrichten, 328, 948

Stritzinger, M., Hamuy, M., Suntzeff, N. B., et al. 2002, AJ, 124, 2100

Szczygieł, D. M., Gerke, J. R., Kochanek, C. S., & Stanek, K. Z. 2012, ApJ, 747, 23

Takáts, K. & Vinkó, J. 2006, MNRAS, 372, 1735

Taubenberger, S., Navasardyan, H., Maurer, J. I., et al. 2011, MNRAS, 413, 2140

Terry, J. N., Paturel, G., & Ekholm, T. 2002, A&A, 393, 57

Theureau, G., Hanski, M. O., Coudreau, N., Hallet, N., & Martin, J.-M. 2007, A&A, 465, 71

Tonry, J. L., Dressler, A., Blakeslee, J. P., et al. 2001, ApJ, 546, 681

Tsvetkov, D. Y., Volkov, I. M., Baklanov, P., Blinnikov, S., & Tuchin, O. 2009, Peremennye Zvezdy, 29, 2

Tsvetkov, D. Y., Volkov, I. M., Sorokina, E., et al. 2012, Peremennye Zvezdy, 32, 6

Tully, X. 1988

Turatto, M., Benetti, S., & Cappellaro, E. 2003

Valenti, S., Fraser, M., Benetti, S., et al. 2011, MNRAS, 416, 3138

Van Dyk, S. D., Filippenko, A. V., Fox, O., Kelly, P., & Smith, N. 2013, The Astronomer's Telegram, 4850, 1

Van Dyk, S. D., Li, W., Cenko, S. B., et al. 2011, ApJ, 741, L28

Vinkó, J., Takáts, K., Szalai, T., et al. 2012, A&A, 540, A93

Wada, T. & Ueno, M. 1997, AJ, 113, 231

Woosley, S. E., Eastman, R. G., Weaver, T. A., & Pinto, P. A. 1994, ApJ, 429, 300

Yaron, O. & Gal-Yam, A. 2012, PASP, 124, 668

Fig. 2. Optical and NIR (interpolated) spectral evolution for SN 2011dh for days 5−100 with a 5-day sampling. Telluric absorption bands are marked with a ⊕ symbol in the optical and shown as grey regions in the NIR.
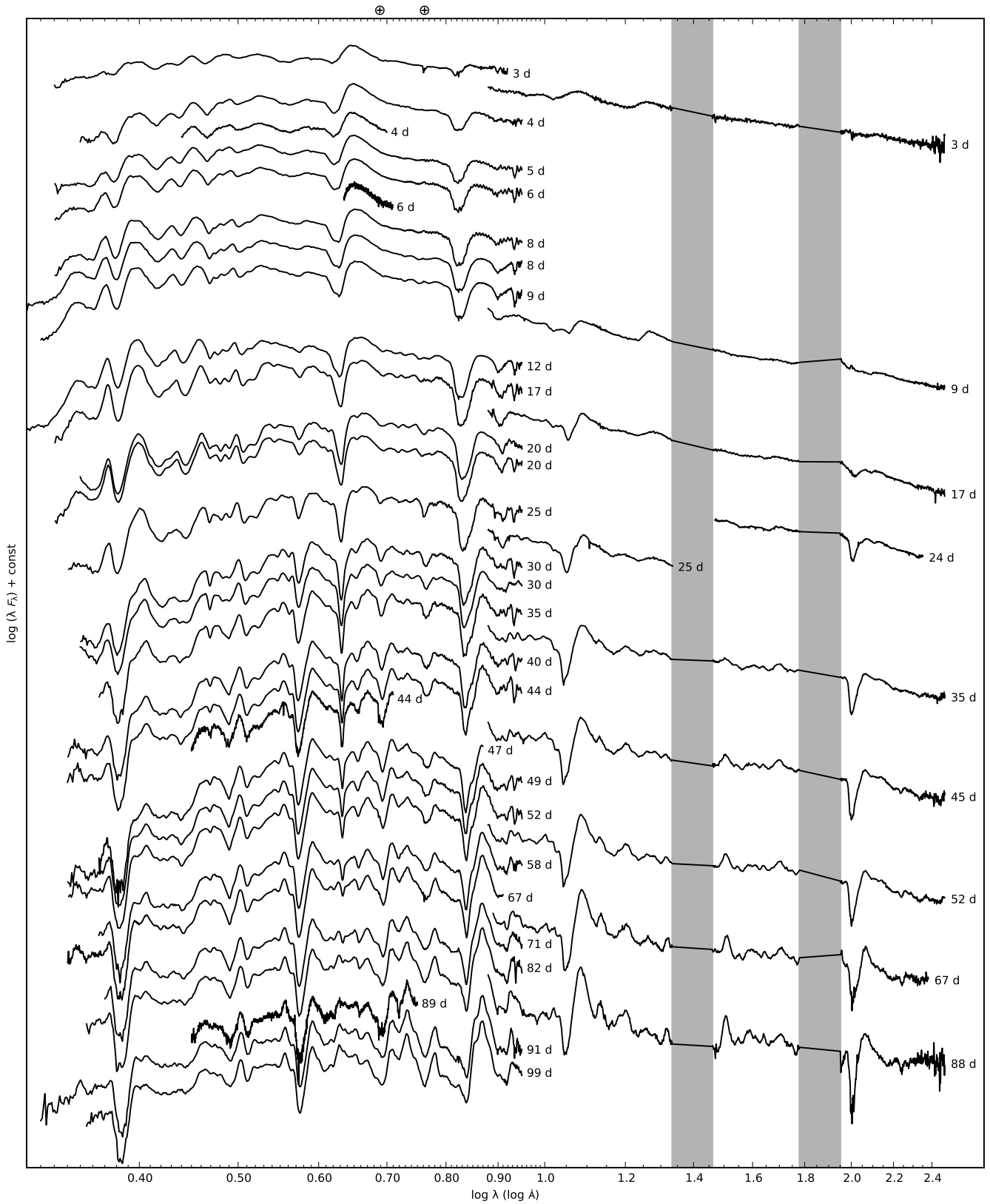
Fig. 3. Sequence of the observed spectra for SN 2011dh. Spectra obtained on the same night using the same telescope and instrument have been combined and each spectra have been labelled with the phase of the SN. Telluric absorption bands are marked with a ⊕ symbol in the optical and shown as grey regions in the NIR.

Table 3. Optical colour-corrected JC *U* and S-corrected JC *BVRI* magnitudes for SN 2011dh. Errors are given in parentheses.

JD (+2400000)	Phase	*U*	*B*	*V*	*R*	*I*	Telescope (Instrument)
(d)	(d)	(mag)	(mag)	(mag)	(mag)	(mag)	
55716.43	3.43	14.99 (0.03)	15.35 (0.02)	14.92 (0.02)	14.54 (0.01)	14.41 (0.02)	LT (RATCam)
55716.43	3.43	15.15 (0.08)	15.39 (0.02)	14.94 (0.02)	14.57 (0.01)	14.46 (0.01)	TNG (LRS)
55717.43	4.43	15.03 (0.03)	15.14 (0.02)	14.67 (0.03)	14.25 (0.01)	14.26 (0.03)	LT (RATCam)
55717.48	4.48	15.17 (0.09)	15.21 (0.03)	14.63 (0.03)	14.24 (0.01)	14.23 (0.02)	AS-1.82m (AFOSC)
55717.48	4.48	...	15.12 (0.03)	14.63 (0.02)	14.27 (0.01)	14.28 (0.02)	CANTAB (BIGST8)
55718.48	5.48	...	14.84 (0.01)	14.28 (0.02)	13.94 (0.01)	13.94 (0.01)	LT (RATCam)
55718.57	5.57	14.68 (0.06)	14.84 (0.02)	14.24 (0.02)	13.91 (0.01)	14.04 (0.01)	CA-2.2m (CAFOS)
55720.42	7.42	14.42 (0.02)	14.25 (0.01)	13.75 (0.03)	13.41 (0.01)	13.43 (0.02)	LT (RATCam)
55721.42	8.42	14.28 (0.10)	14.02 (0.01)	13.48 (0.01)	13.22 (0.01)	13.24 (0.02)	LT (RATCam)
55721.43	8.43	14.07 (0.07)	14.06 (0.01)	13.60 (0.04)	13.27 (0.02)	13.34 (0.02)	NOT (ALFOSC)
55722.42	9.42	...	13.86 (0.01)	13.29 (0.01)	13.05 (0.01)	13.07 (0.01)	LT (RATCam)
55723.41	10.41	13.98 (0.06)	13.71 (0.01)	13.16 (0.01)	12.89 (0.01)	12.90 (0.01)	LT (RATCam)
55724.41	11.41	13.91 (0.08)	13.62 (0.01)	13.03 (0.01)	12.79 (0.01)	12.77 (0.01)	LT (RATCam)
55725.39	12.39	...	...	12.94 (0.02)	12.66 (0.01)	...	MONTCAB (BIGST8)
55725.43	12.43	13.88 (0.07)	13.52 (0.02)	12.92 (0.04)	12.68 (0.01)	12.68 (0.01)	LT (RATCam)
55726.36	13.36	...	13.52 (0.01)	12.91 (0.02)	12.59 (0.01)	...	MONTCAB (BIGST8)
55728.40	15.40	...	13.39 (0.01)	12.77 (0.01)	12.44 (0.01)	...	MONTCAB (BIGST8)
55729.39	16.39	13.65 (0.01)	13.35 (0.01)	12.77 (0.06)	12.39 (0.01)	12.35 (0.02)	LT (RATCam)
55730.40	17.40	13.64 (0.03)	13.33 (0.01)	12.66 (0.01)	12.36 (0.01)	12.32 (0.01)	LT (RATCam)
55731.41	18.41	13.74 (0.09)	13.30 (0.01)	12.60 (0.02)	12.31 (0.01)	12.27 (0.01)	LT (RATCam)
55731.82	18.82	...	...	...	12.33 (0.02)	12.25 (0.01)	FTN (FS02)
55732.40	19.40	...	13.35 (0.03)	12.61 (0.01)	12.27 (0.01)	12.21 (0.01)	CANTAB (BIGST8)
55732.41	19.41	13.44 (0.06)	13.36 (0.02)	12.64 (0.02)	12.33 (0.02)	12.31 (0.02)	NOT (ALFOSC)
55732.46	19.46	13.71 (0.07)	13.32 (0.01)	12.58 (0.01)	12.28 (0.02)	12.22 (0.01)	LT (RATCam)
55733.45	20.45	13.67 (0.07)	...	...	12.26 (0.01)	12.20 (0.02)	LT (RATCam)
55734.52	21.52	13.37 (0.05)	13.33 (0.01)	12.58 (0.01)	12.25 (0.01)	12.29 (0.01)	CA-2.2m (CAFOS)
55735.44	22.44	13.91 (0.04)	...	...	12.26 (0.01)	12.16 (0.01)	LT (RATCam)
55736.44	23.44	14.13 (0.08)	...	...	12.26 (0.01)	12.16 (0.01)	LT (RATCam)
55737.39	24.39	...	13.65 (0.01)	12.72 (0.01)	...	...	LT (RATCam)
55738.42	25.42	14.50 (0.04)	13.79 (0.02)	12.81 (0.01)	12.32 (0.02)	12.22 (0.01)	LT (RATCam)
55738.51	25.51	14.20 (0.04)	13.77 (0.02)	12.82 (0.01)	12.38 (0.01)	12.26 (0.01)	NOT (ALFOSC)
55739.43	26.43	14.73 (0.04)	13.95 (0.02)	12.88 (0.01)	12.38 (0.01)	12.23 (0.01)	LT (RATCam)
55740.36	27.36	...	14.09 (0.04)	12.93 (0.01)	12.45 (0.01)	12.29 (0.01)	MONTCAB (BIGST8)
55740.43	27.43	14.91 (0.03)	14.12 (0.01)	12.97 (0.01)	12.48 (0.01)	12.30 (0.01)	LT (RATCam)
55740.44	27.44	...	...	12.97 (0.01)	12.47 (0.01)	...	TJO (MEIA)
55741.44	28.44	...	...	...	12.54 (0.01)	12.32 (0.01)	LT (RATCam)
55742.49	29.49	15.33 (0.01)	...	...	12.62 (0.01)	12.40 (0.01)	LT (RATCam)
55743.41	30.41	...	14.53 (0.01)	13.27 (0.02)	...	...	LT (RATCam)
55743.42	30.42	15.18 (0.05)	14.51 (0.02)	...	12.65 (0.01)	12.53 (0.01)	CA-2.2m (CAFOS)
55743.42	30.42	15.43 (0.05)	14.53 (0.01)	13.26 (0.03)	12.68 (0.01)	12.49 (0.01)	NOT (ALFOSC)
55745.39	32.39	15.74 (0.03)	14.74 (0.01)	13.44 (0.01)	12.77 (0.01)	12.56 (0.01)	NOT (ALFOSC)
55745.44	32.44	15.93 (0.04)	...	...	12.81 (0.01)	12.53 (0.01)	LT (RATCam)
55745.80	32.80	...	...	...	12.80 (0.01)	12.51 (0.01)	FTN (FS02)
55746.45	33.45	16.07 (0.04)	14.87 (0.03)	13.51 (0.01)	12.83 (0.01)	12.55 (0.02)	LT (RATCam)
55747.44	34.44	16.12 (0.04)	...	...	12.89 (0.01)	12.59 (0.01)	LT (RATCam)
55748.43	35.43	16.02 (0.02)	14.97 (0.01)	13.62 (0.01)	12.88 (0.01)	12.65 (0.01)	NOT (ALFOSC)
55748.44	35.44	16.27 (0.04)	...	...	12.94 (0.01)	12.62 (0.01)	LT (RATCam)
55750.40	37.40	16.20 (0.04)	15.10 (0.01)	13.73 (0.01)	13.03 (0.01)	12.73 (0.01)	NOT (ALFOSC)
55750.42	37.42	16.41 (0.14)	15.11 (0.02)	13.78 (0.03)	13.03 (0.01)	12.73 (0.02)	LT (RATCam)
55751.41	38.41	...	15.14 (0.01)	13.81 (0.01)	13.08 (0.01)	12.73 (0.01)	TJO (MEIA)
55751.43	38.43	...	...	...	13.11 (0.01)	12.77 (0.01)	LT (RATCam)
55752.45	39.45	16.54 (0.16)	...	...	13.13 (0.01)	12.75 (0.01)	LT (RATCam)

Table 3. Continued.

JD (+2400000) (d)	Phase (d)	U (mag)	B (mag)	V (mag)	R (mag)	I (mag)	Telescope (Instrument)
55753.42	40.42	...	15.29 (0.01)	13.90 (0.02)	...	...	LT (RATCam)
55753.46	40.46	16.45 (0.05)	15.24 (0.01)	13.86 (0.01)	13.15 (0.01)	12.81 (0.01)	NOT (ALFOSC)
55755.40	42.40	16.42 (0.04)	15.30 (0.01)	13.96 (0.01)	13.23 (0.01)	12.89 (0.01)	NOT (ALFOSC)
55756.44	43.44	...	15.28 (0.02)	13.98 (0.02)	13.28 (0.02)	12.86 (0.01)	AS-Schmidt (SBIG)
55756.45	43.45	...	15.38 (0.02)	13.98 (0.01)	13.27 (0.03)	12.92 (0.01)	LT (RATCam)
55757.43	44.43	16.42 (0.04)	15.38 (0.01)	14.05 (0.01)	13.29 (0.01)	12.97 (0.01)	NOT (ALFOSC)
55759.45	46.45	...	15.44 (0.01)	14.06 (0.02)	...	...	LT (RATCam)
55761.40	48.40	...	15.44 (0.01)	14.17 (0.01)	13.44 (0.01)	13.02 (0.01)	AS-Schmidt (SBIG)
55762.41	49.41	...	15.45 (0.01)	14.16 (0.01)	13.44 (0.01)	13.06 (0.01)	NOT (ALFOSC)
55762.78	49.78	...	...	...	13.44 (0.01)	13.03 (0.01)	FTN (FS02)
55763.44	50.44	...	15.47 (0.01)	14.22 (0.01)	13.47 (0.01)	13.09 (0.01)	AS-Schmidt (SBIG)
55765.43	52.43	16.44 (0.03)	15.52 (0.01)	14.26 (0.01)	13.55 (0.01)	13.17 (0.01)	NOT (ALFOSC)
55767.43	54.43	16.50 (0.05)	...	...	13.58 (0.01)	13.16 (0.02)	LT (RATCam)
55768.45	55.45	16.48 (0.04)	...	...	13.60 (0.02)	13.19 (0.02)	LT (RATCam)
55771.40	58.40	16.37 (0.03)	15.58 (0.01)	14.32 (0.01)	13.62 (0.01)	13.28 (0.01)	CA-2.2m (CAFOS)
55773.39	60.39	16.45 (0.04)	15.60 (0.01)	14.38 (0.01)	13.71 (0.01)	13.32 (0.01)	NOT (ALFOSC)
55776.38	63.38	16.47 (0.04)	15.64 (0.01)	14.46 (0.01)	13.77 (0.01)	13.36 (0.01)	NOT (ALFOSC)
55777.33	64.33	...	15.52 (0.03)	14.46 (0.02)	13.78 (0.02)	13.34 (0.02)	AS-Schmidt (SBIG)
55780.40	67.40	16.42 (0.03)	15.65 (0.01)	14.50 (0.01)	13.85 (0.01)	13.43 (0.01)	NOT (ALFOSC)
55783.43	70.43	16.41 (0.03)	15.71 (0.01)	14.58 (0.01)	13.94 (0.01)	13.51 (0.01)	NOT (ALFOSC)
55784.33	71.33	...	15.66 (0.02)	14.59 (0.01)	...	13.43 (0.02)	AS-Schmidt (SBIG)
55784.39	71.39	16.45 (0.04)	15.66 (0.01)	14.52 (0.02)	13.90 (0.01)	13.47 (0.02)	CA-2.2m (CAFOS)
55784.77	71.77	...	...	...	13.93 (0.02)	13.45 (0.01)	FTN (FS02)
55785.36	72.36	...	15.70 (0.02)	14.61 (0.01)	13.96 (0.01)	13.45 (0.01)	AS-Schmidt (SBIG)
55788.41	75.41	...	...	...	14.02 (0.02)	13.52 (0.01)	AS-Schmidt (SBIG)
55790.38	77.38	16.45 (0.09)	...	...	14.03 (0.01)	13.61 (0.01)	LT (RATCam)
55793.37	80.37	16.55 (0.07)	15.80 (0.01)	14.74 (0.01)	14.13 (0.01)	13.67 (0.01)	NOT (ALFOSC)
55795.35	82.35	16.40 (0.04)	15.78 (0.01)	14.76 (0.01)	14.12 (0.01)	13.68 (0.01)	CA-2.2m (CAFOS)
55797.37	84.37	...	15.83 (0.02)	14.82 (0.01)	...	...	AS-Schmidt (SBIG)
55797.76	84.76	...	...	...	14.22 (0.01)	13.68 (0.01)	FTN (FS02)
55798.36	85.36	16.50 (0.03)	15.84 (0.01)	14.84 (0.01)	14.25 (0.01)	13.65 (0.02)	NOT (ALFOSC)
55799.33	86.33	...	15.82 (0.01)	14.86 (0.01)	...	...	AS-Schmidt (SBIG)
55801.36	88.36	16.44 (0.04)	15.89 (0.01)	14.90 (0.01)	14.31 (0.01)	13.80 (0.01)	NOT (ALFOSC)
55801.40	88.40	...	15.80 (0.02)	14.90 (0.01)	...	...	AS-Schmidt (SBIG)
55803.35	90.35	...	15.88 (0.02)	14.91 (0.01)	14.32 (0.01)	13.79 (0.01)	AS-Schmidt (SBIG)
55805.33	92.33	...	15.87 (0.02)	14.97 (0.02)	14.37 (0.01)	13.83 (0.01)	AS-Schmidt (SBIG)
55810.34	97.34	16.68 (0.06)	16.00 (0.01)	15.11 (0.01)	14.52 (0.01)	14.02 (0.01)	NOT (ALFOSC)
55812.33	99.33	16.51 (0.03)	16.02 (0.01)	15.05 (0.01)	14.49 (0.01)	14.00 (0.01)	CA-2.2m (CAFOS)

Table 4. Optical S-corrected SWIFT JC *UBV* magnitudes for SN 2011dh. Errors are given in parentheses.

JD (+2400000)	Phase	U	B	V	Telescope (Instrument)
(d)	(d)	(mag)	(mag)	(mag)	
55716.01	3.01	14.92 (0.02)	15.35 (0.02)	14.96 (0.02)	SWIFT (UVOT)
55716.68	3.68	15.05 (0.02)	15.29 (0.02)	14.90 (0.01)	SWIFT (UVOT)
55717.82	4.82	15.03 (0.04)	15.03 (0.03)	14.57 (0.03)	SWIFT (UVOT)
55719.03	6.03	14.77 (0.03)	14.65 (0.02)	14.14 (0.02)	SWIFT (UVOT)
55720.83	7.83	14.31 (0.03)	14.15 (0.02)	13.65 (0.01)	SWIFT (UVOT)
55721.84	8.84	14.11 (0.02)	13.96 (0.02)	13.43 (0.01)	SWIFT (UVOT)
55723.18	10.18	13.93 (0.02)	13.73 (0.02)	13.20 (0.01)	SWIFT (UVOT)
55723.98	10.98	13.85 (0.02)	13.68 (0.02)	13.12 (0.01)	SWIFT (UVOT)
55725.13	12.13	13.77 (0.02)	13.57 (0.02)	12.97 (0.01)	SWIFT (UVOT)
55726.66	13.66	13.78 (0.02)	13.57 (0.02)	12.91 (0.01)	SWIFT (UVOT)
55727.79	14.79	13.71 (0.02)	13.48 (0.02)	12.80 (0.01)	SWIFT (UVOT)
55727.87	14.87	13.76 (0.05)	...	...	SWIFT (UVOT)
55729.25	16.25	13.69 (0.02)	13.42 (0.02)	12.77 (0.01)	SWIFT (UVOT)
55729.60	16.60	13.63 (0.02)	13.42 (0.02)	12.72 (0.01)	SWIFT (UVOT)
55730.53	17.53	13.66 (0.02)	13.36 (0.02)	12.69 (0.01)	SWIFT (UVOT)
55731.65	18.65	13.66 (0.02)	13.35 (0.02)	12.64 (0.01)	SWIFT (UVOT)
55732.67	19.67	13.69 (0.02)	13.37 (0.02)	12.62 (0.01)	SWIFT (UVOT)
55733.89	20.89	13.74 (0.02)	13.37 (0.02)	12.63 (0.01)	SWIFT (UVOT)
55734.75	21.75	13.82 (0.02)	13.44 (0.02)	12.63 (0.01)	SWIFT (UVOT)
55735.95	22.95	13.99 (0.03)	13.53 (0.02)	12.68 (0.01)	SWIFT (UVOT)
55736.55	23.55	14.05 (0.03)	13.55 (0.02)	12.71 (0.01)	SWIFT (UVOT)
55737.55	24.55	14.30 (0.03)	13.70 (0.02)	12.77 (0.01)	SWIFT (UVOT)
55738.76	25.76	14.54 (0.03)	13.83 (0.02)	12.84 (0.02)	SWIFT (UVOT)
55740.28	27.28	14.85 (0.03)	14.07 (0.02)	13.01 (0.03)	SWIFT (UVOT)
55741.37	28.37	15.08 (0.05)	14.23 (0.03)	13.09 (0.02)	SWIFT (UVOT)
55741.77	28.77	15.20 (0.05)	14.32 (0.03)	13.16 (0.02)	SWIFT (UVOT)
55742.84	29.84	15.43 (0.05)	14.46 (0.03)	13.26 (0.02)	SWIFT (UVOT)
55743.84	30.84	15.63 (0.05)	14.55 (0.03)	13.33 (0.02)	SWIFT (UVOT)
55745.25	32.25	15.76 (0.05)	14.74 (0.03)	13.43 (0.02)	SWIFT (UVOT)
55746.12	33.12	15.91 (0.06)	14.80 (0.03)	13.50 (0.02)	SWIFT (UVOT)
55750.60	37.60	16.30 (0.06)	15.03 (0.03)	13.74 (0.02)	SWIFT (UVOT)
55754.62	41.62	16.46 (0.07)	15.24 (0.03)	13.97 (0.02)	SWIFT (UVOT)
55758.55	45.55	16.54 (0.08)	15.37 (0.03)	14.07 (0.02)	SWIFT (UVOT)
55762.57	49.57	16.75 (0.10)	15.45 (0.04)	14.19 (0.02)	SWIFT (UVOT)
55766.52	53.52	16.60 (0.08)	15.57 (0.04)	14.30 (0.02)	SWIFT (UVOT)
55770.80	57.80	16.48 (0.07)	15.61 (0.04)	14.35 (0.02)	SWIFT (UVOT)
55775.69	62.69	16.42 (0.07)	15.60 (0.04)	14.48 (0.03)	SWIFT (UVOT)
55780.50	67.50	16.60 (0.08)	15.70 (0.04)	14.52 (0.03)	SWIFT (UVOT)
55784.80	71.80	16.46 (0.07)	15.71 (0.04)	14.61 (0.03)	SWIFT (UVOT)
55788.74	75.74	16.43 (0.06)	15.73 (0.04)	14.64 (0.03)	SWIFT (UVOT)

Table 5. Optical colour-corrected SDSS *u* and S-corrected SDSS *griz* magnitudes for SN 2011dh. Errors are given in parentheses.

JD (+2400000)	Phase	*u*	*g*	*r*	*i*	*z*	Telescope (Instrument)
(d)	(d)	(mag)	(mag)	(mag)	(mag)	(mag)	
55716.47	3.47	15.90 (0.03)	15.08 (0.01)	14.68 (0.01)	14.80 (0.01)	14.76 (0.02)	LT (RATCam)
55717.46	4.46	16.01 (0.03)	14.80 (0.01)	14.38 (0.01)	14.61 (0.01)	14.58 (0.02)	LT (RATCam)
55718.53	5.53	...	14.44 (0.04)	14.06 (0.01)	14.27 (0.01)	...	LT (RATCam)
55720.44	7.44	15.39 (0.02)	13.97 (0.01)	13.53 (0.01)	13.73 (0.02)	13.87 (0.01)	LT (RATCam)
55721.44	8.44	15.09 (0.01)	13.78 (0.01)	13.33 (0.01)	13.52 (0.01)	13.64 (0.01)	LT (RATCam)
55722.44	9.44	...	13.59 (0.01)	13.18 (0.01)	13.35 (0.01)	13.49 (0.01)	LT (RATCam)
55723.41	10.41	14.82 (0.03)	...	13.02 (0.01)	13.16 (0.01)	13.34 (0.01)	LT (RATCam)
55724.41	11.41	14.72 (0.02)	...	12.93 (0.01)	13.05 (0.01)	13.22 (0.01)	LT (RATCam)
55725.43	12.43	14.74 (0.04)	...	12.83 (0.01)	12.94 (0.01)	13.09 (0.01)	LT (RATCam)
55729.39	16.39	14.56 (0.03)	13.10 (0.01)	12.56 (0.01)	12.62 (0.01)	12.81 (0.01)	LT (RATCam)
55730.40	17.40	14.45 (0.03)	13.07 (0.01)	12.51 (0.01)	12.56 (0.01)	12.77 (0.01)	LT (RATCam)
55731.41	18.41	14.54 (0.03)	13.02 (0.01)	12.46 (0.01)	12.51 (0.01)	12.71 (0.01)	LT (RATCam)
55731.82	18.82	...	13.07 (0.01)	12.46 (0.01)	12.50 (0.01)	12.65 (0.01)	FTN (FS02)
55732.46	19.46	14.56 (0.01)	13.00 (0.03)	12.42 (0.01)	12.48 (0.01)	12.67 (0.01)	LT (RATCam)
55733.45	20.45	14.52 (0.05)	13.03 (0.01)	12.41 (0.01)	12.45 (0.01)	12.65 (0.01)	LT (RATCam)
55735.44	22.44	14.75 (0.04)	13.12 (0.01)	12.43 (0.01)	12.41 (0.01)	12.60 (0.01)	LT (RATCam)
55736.44	23.44	14.96 (0.03)	13.19 (0.02)	12.45 (0.01)	12.42 (0.01)	12.59 (0.02)	LT (RATCam)
55738.45	25.45	15.37 (0.02)	13.43 (0.01)	12.55 (0.01)	12.47 (0.01)	12.65 (0.01)	LT (RATCam)
55739.44	26.44	15.55 (0.02)	13.50 (0.03)	12.59 (0.01)	12.50 (0.01)	12.65 (0.01)	LT (RATCam)
55740.44	27.44	15.80 (0.01)	13.66 (0.01)	12.66 (0.01)	12.55 (0.01)	12.70 (0.01)	LT (RATCam)
55741.44	28.44	...	13.75 (0.02)	12.76 (0.01)	12.59 (0.02)	12.76 (0.01)	LT (RATCam)
55742.49	29.49	16.20 (0.02)	13.92 (0.01)	12.84 (0.01)	12.65 (0.01)	12.80 (0.01)	LT (RATCam)
55745.44	32.44	16.71 (0.05)	14.20 (0.02)	13.04 (0.01)	12.79 (0.01)	12.87 (0.03)	LT (RATCam)
55745.80	32.80	...	14.35 (0.04)	13.00 (0.01)	12.79 (0.01)	12.94 (0.01)	FTN (FS02)
55746.45	33.45	16.83 (0.04)	14.32 (0.01)	13.09 (0.01)	12.82 (0.01)	12.94 (0.01)	LT (RATCam)
55747.44	34.44	16.90 (0.04)	14.40 (0.02)	13.13 (0.01)	12.86 (0.01)	12.95 (0.01)	LT (RATCam)
55748.44	35.44	17.09 (0.04)	14.42 (0.02)	13.19 (0.01)	12.90 (0.01)	13.01 (0.01)	LT (RATCam)
55750.44	37.44	17.20 (0.10)	14.55 (0.02)	13.29 (0.01)	13.02 (0.02)	13.04 (0.04)	LT (RATCam)
55751.43	38.43	17.14 (0.03)	14.64 (0.03)	13.36 (0.01)	13.04 (0.01)	13.11 (0.01)	LT (RATCam)
55752.45	39.45	17.24 (0.07)	14.66 (0.01)	13.39 (0.01)	13.04 (0.01)	13.09 (0.01)	LT (RATCam)
55756.46	43.46	...	14.79 (0.01)	13.55 (0.01)	13.22 (0.01)	13.19 (0.01)	LT (RATCam)
55762.78	49.78	...	15.00 (0.02)	13.68 (0.01)	13.37 (0.01)	13.28 (0.01)	FTN (FS02)
55767.43	54.43	17.30 (0.02)	15.03 (0.01)	13.84 (0.01)	13.52 (0.01)	13.38 (0.02)	LT (RATCam)
55768.45	55.45	17.29 (0.02)	15.03 (0.01)	13.86 (0.01)	13.56 (0.01)	13.41 (0.01)	LT (RATCam)
55773.39	60.39	17.27 (0.04)	15.07 (0.01)	13.99 (0.01)	13.72 (0.01)	13.54 (0.02)	NOT (ALFOSC)
55776.38	63.38	17.36 (0.03)	15.13 (0.01)	14.03 (0.01)	13.76 (0.01)	13.56 (0.01)	NOT (ALFOSC)
55780.41	67.41	17.33 (0.03)	15.16 (0.01)	14.09 (0.01)	13.84 (0.01)	13.61 (0.01)	NOT (ALFOSC)
55783.44	70.44	17.26 (0.04)	15.18 (0.01)	14.19 (0.01)	13.93 (0.01)	13.67 (0.01)	NOT (ALFOSC)
55784.77	71.77	...	15.23 (0.02)	14.16 (0.01)	13.88 (0.01)	13.64 (0.01)	FTN (FS02)
55790.38	77.38	17.29 (0.03)	15.35 (0.04)	14.28 (0.01)	14.04 (0.01)	13.69 (0.02)	LT (RATCam)
55793.37	80.37	17.32 (0.03)	15.30 (0.01)	14.39 (0.01)	14.16 (0.01)	13.84 (0.01)	NOT (ALFOSC)
55797.76	84.76	...	15.38 (0.01)	14.42 (0.01)	14.18 (0.01)	13.82 (0.01)	FTN (FS02)
55798.37	85.37	17.35 (0.03)	15.38 (0.01)	14.50 (0.01)	14.26 (0.01)	13.87 (0.01)	NOT (ALFOSC)
55801.36	88.36	17.34 (0.01)	15.42 (0.01)	14.53 (0.01)	14.31 (0.01)	13.89 (0.01)	NOT (ALFOSC)
55810.34	97.34	17.49 (0.02)	15.55 (0.01)	14.75 (0.01)	14.56 (0.01)	14.10 (0.02)	NOT (ALFOSC)

Table 6. NIR S-corrected 2MASS *JHK* magnitudes for SN 2011dh. Errors are given in parentheses.

JD (+2400000)	Phase	J	H	K	Telescope (Instrument)
(d)	(d)	(mag)	(mag)	(mag)	
55716.51	3.51	14.09 (0.01)	13.90 (0.01)	13.68 (0.02)	TNG (NICS)
55722.40	9.40	12.89 (0.01)	12.87 (0.01)	12.67 (0.01)	TNG (NICS)
55725.50	12.50	12.61 (0.04)	12.54 (0.01)	12.43 (0.02)	NOT (NOTCAM)
55730.51	17.51	12.12 (0.01)	12.08 (0.01)	11.94 (0.01)	TNG (NICS)
55737.72	24.72	11.96 (0.01)	11.90 (0.01)	11.72 (0.03)	LBT (LUCIFER)
55741.13	28.13	11.94 (0.01)	11.90 (0.02)	11.70 (0.05)	TCS (CAIN)
55748.43	35.43	12.14 (0.01)	12.00 (0.02)	11.77 (0.01)	TCS (CAIN)
55750.42	37.42	12.19 (0.01)	12.00 (0.01)	11.84 (0.04)	TCS (CAIN)
55751.42	38.42	12.29 (0.01)	12.01 (0.01)	11.84 (0.03)	TCS (CAIN)
55758.45	45.45	12.55 (0.01)	12.22 (0.01)	12.06 (0.01)	TNG (NICS)
55759.41	46.41	12.49 (0.03)	12.22 (0.03)	12.11 (0.04)	TCS (CAIN)
55762.41	49.41	12.57 (0.01)	12.26 (0.01)	12.17 (0.03)	TCS (CAIN)
55763.42	50.42	12.62 (0.02)	12.27 (0.04)	12.25 (0.06)	TCS (CAIN)
55765.45	52.45	12.79 (0.01)	12.38 (0.01)	12.23 (0.01)	TNG (NICS)
55769.41	56.41	12.77 (0.01)	12.48 (0.06)	12.40 (0.03)	TCS (CAIN)
55773.37	60.37	12.94 (0.03)	12.58 (0.01)	12.42 (0.02)	TNG (NICS)
55774.40	61.40	12.90 (0.01)	12.55 (0.03)	12.43 (0.04)	TCS (CAIN)
55776.40	63.40	13.00 (0.01)	12.64 (0.01)	12.53 (0.02)	TCS (CAIN)
55781.41	68.41	13.23 (0.01)	12.76 (0.01)	12.66 (0.01)	WHT (LIRIS)
55787.44	74.44	13.56 (0.03)	13.03 (0.02)	12.95 (0.02)	NOT (NOTCAM)
55801.36	88.36	13.90 (0.02)	13.41 (0.02)	13.17 (0.01)	TNG (NICS)
55804.34	91.34	14.10 (0.01)	13.50 (0.01)	13.26 (0.01)	CA-3.5m (O2000)

Table 7. MIR Spitzer 3.6 μm and 4.5 μm magnitudes for SN 2011dh. Errors are given in parentheses.

JD (+2400000)	Phase	3.6 μm	4.5 μm	Telescope (Instrument)
(d)	(d)	(mag)	(mag)	
55731.21	18.21	11.83 (0.02)	11.48 (0.02)	SPITZER (IRAC)
55737.06	24.06	11.66 (0.02)	11.31 (0.02)	SPITZER (IRAC)
55744.32	31.32	11.66 (0.02)	11.30 (0.02)	SPITZER (IRAC)
55751.46	38.46	11.68 (0.02)	11.30 (0.02)	SPITZER (IRAC)
55758.75	45.75	11.79 (0.02)	11.32 (0.02)	SPITZER (IRAC)
55766.45	53.45	11.96 (0.02)	11.34 (0.02)	SPITZER (IRAC)
55772.33	59.33	12.11 (0.03)	11.38 (0.02)	SPITZER (IRAC)
55779.12	66.12	12.30 (0.03)	11.43 (0.02)	SPITZER (IRAC)
55785.60	72.60	12.50 (0.03)	11.50 (0.02)	SPITZER (IRAC)
55798.28	85.28	12.84 (0.04)	11.66 (0.03)	SPITZER (IRAC)

Table 8. UV SWIFT *UVW*1, *UVM*2 and *UVW*2 magnitudes for SN 2011dh. Errors are given in parentheses.

JD (+2400000) (d)	Phase (d)	*UVW*1 (mag)	*UVM*2 (mag)	*UVW*2 (mag)	Telescope (Instrument)
55716.01	3.01	15.40 (0.04)	15.99 (0.04)	16.40 (0.04)	SWIFT (UVOT)
55716.68	3.68	15.56 (0.04)	16.27 (0.05)	16.69 (0.04)	SWIFT (UVOT)
55717.55	4.55	15.80 (0.05)	16.59 (0.08)	16.91 (0.08)	SWIFT (UVOT)
55718.90	5.90	15.85 (0.04)	16.77 (0.04)	16.98 (0.05)	SWIFT (UVOT)
55720.60	7.60	15.75 (0.04)	16.89 (0.09)	...	SWIFT (UVOT)
55721.30	8.30	...	...	16.95 (0.07)	SWIFT (UVOT)
55722.50	9.50	15.62 (0.04)	17.28 (0.08)	...	SWIFT (UVOT)
55723.10	10.10	...	...	17.02 (0.13)	SWIFT (UVOT)
55724.80	11.80	15.66 (0.04)	17.37 (0.08)	17.00 (0.05)	SWIFT (UVOT)
55727.10	14.10	15.59 (0.04)	17.61 (0.09)	17.11 (0.05)	SWIFT (UVOT)
55730.66	17.66	15.56 (0.03)	17.72 (0.06)	17.00 (0.04)	SWIFT (UVOT)
55733.70	20.70	15.65 (0.03)	17.93 (0.07)	17.14 (0.04)	SWIFT (UVOT)
55736.57	23.57	15.87 (0.04)	18.16 (0.09)	17.32 (0.05)	SWIFT (UVOT)
55739.95	26.95	16.42 (0.04)	...	17.82 (0.08)	SWIFT (UVOT)
55740.70	27.70	...	18.49 (0.19)	...	SWIFT (UVOT)
55742.27	29.27	16.67 (0.06)	19.06 (0.26)	18.36 (0.13)	SWIFT (UVOT)
55747.73	34.73	17.18 (0.06)	19.11 (0.20)	19.03 (0.19)	SWIFT (UVOT)
55758.17	45.17	17.64 (0.08)	19.37 (0.25)	19.47 (0.25)	SWIFT (UVOT)
55770.83	57.83	17.67 (0.08)	19.74 (0.33)	19.97 (0.40)	SWIFT (UVOT)
55784.97	71.97	17.77 (0.09)	20.22 (0.58)	19.91 (0.40)	SWIFT (UVOT)

Table 9. List of optical and NIR spectroscopic observations.

JD (+2400000) (d)	Phase (d)	Grism	Range (Å)	Resolution	Resolution (Å)	Telescope (Instrument)
55716.41	3.41	LRB	3300-8000	585	10.0	TNG (LRS)
55716.41	3.41	LRR	5300-9200	714	10.4	TNG (LRS)
55716.47	3.47	IJ	9000-14500	333	...	TNG (NICS)
55716.49	3.49	HK	14000-25000	333	...	TNG (NICS)
55717.37	4.37	b200	3300-8700	....	12.0	CA-2.2m (CAFOS)
55717.37	4.37	r200	6300-10500	...	12.0	CA-2.2m (CAFOS)
55717.49	4.49	Grism 4	3500-8450	613	...	AS 1.82m (AFOSC)
55718.42	5.42	Grism 4	3200-9100	355	16.2	NOT (ALFOSC)
55718.44	5.44	Grism 5	5000-10250	415	16.8	NOT (ALFOSC)
55719.40	6.40	Grism 4	3200-9100	355	16.2	NOT (ALFOSC)
55719.42	6.42	Grism 5	5000-10250	415	16.8	NOT (ALFOSC)
55719.47	6.47	VPH4	6350-7090	...	3.7	AS-1.82m (AFOSC)
55721.39	8.39	Grism 4	3200-9100	355	16.2	NOT (ALFOSC)
55721.40	8.40	Grism 5	5000-10250	415	16.8	NOT (ALFOSC)
55721.45	8.45	R300B	3200-5300	...	4.1	WHT (ISIS)
55721.45	8.45	R158R	5300-10000	...	7.7	WHT(ISIS)
55722.57	9.57	R300B	3200-5300	...	4.1	WHT (ISIS)
55722.57	9.57	R158R	5300-10000	...	7.7	WHT (ISIS)
55722.42	9.42	IJ	9000-14500	333	...	TNG (NICS)
55722.46	9.48	HK	14000-25000	333	...	TNG (NICS)
55723.61	10.61	VHRV	4752-6698	2181	2.6	TNG (LRS)
55725.38	12.38	R300B	3200-5300	...	4.1	WHT (ISIS)
55725.38	12.38	R158R	5300-10000	...	7.7	WHT (ISIS)
55730.45	17.45	Grism 4	3200-9100	355	16.2	NOT (ALFOSC)
55730.46	17.46	Grism 5	5000-10250	415	16.8	NOT (ALFOSC)
55730.52	17.52	IJ	9000-14500	333	...	TNG (NICS)
55730.57	17.57	HK	14000-25000	333	...	TNG (NICS)
55733.37	20.37	b200	3300-8700	...	12.0	CA-2.2m (CAFOS)
55733.37	20.37	r200	6300-10500	...	12.0	CA-2.2m (CAFOS)
55733.42	20.42	Grism 4	3200-9100	355	16.2	NOT (ALFOSC)
55733.43	20.43	Grism 5	5000-10250	415	16.8	NOT (ALFOSC)
55737.68	20.43	200 H+K	14900-24000	1881(H)/2573(K)	...	LBT (LUCIFER)
55738.49	25.49	Grism 4	3200-9100	355	16.2	NOT (ALFOSC)
55738.50	25.50	Grism 5	5000-10250	415	16.8	NOT (ALFOSC)
55738.41	25.41	IJ	9000-14500	333	...	TNG (NICS)
55743.40	30.40	Grism 4	3200-9100	355	16.2	NOT (ALFOSC)
55743.44	30.44	Grism 5	5000-10250	415	16.8	NOT (ALFOSC)
55743.43	30.43	b200	3300-8700	...	12.0	CA-2.2m (CAFOS)
55743.43	30.43	r200	6300-10500	...	12.0	CA-2.2m (CAFOS)
55748.40	35.40	Grism 4	3200-9100	355	16.2	NOT (ALFOSC)
55748.41	35.41	Grism 5	5000-10250	415	16.8	NOT (ALFOSC)
55748.39	35.39	IJ	9000-14500	333	...	TNG (NICS)
55748.42	35.42	HK	14000-25000	333	...	TNG (NICS)
55753.41	40.41	Grism 4	3200-9100	355	16.2	NOT (ALFOSC)
55753.43	40.43	Grism 5	5000-10250	415	16.8	NOT (ALFOSC)
55757.39	44.39	Grism 4	3200-9100	355	16.2	NOT (ALFOSC)
55757.41	44.41	Grism 5	5000-10250	415	16.8	NOT (ALFOSC)
55757.41	44.41	gt300	3200-7700	555	9.0	AS-1.22m (DU440)
55758.39	45.39	IJ	9000-14500	333	...	TNG (NICS)
55758.42	45.42	HK	14000-25000	333	...	TNG (NICS)
55760.38	47.38	b200	3300-8700	...	12.0	CA-2.2m (CAFOS)
55762.39	49.39	Grism 4	3200-9100	355	16.2	NOT (ALFOSC)
55762.40	49.40	Grism 5	5000-10250	415	16.8	NOT (ALFOSC)
55765.40	52.40	Grism 4	3200-9100	355	16.2	NOT (ALFOSC)
55765.42	52.42	Grism 5	5000-10250	415	16.8	NOT (ALFOSC)

Table 9. Continued.

JD (+2400000) (d)	Phase (d)	Grism	Range (Å)	Resolution	Resolution (Å)	Telescope (Instrument)
55765.39	52.39	IJ	9000-14500	333	...	TNG (NICS)
55765.42	52.42	HK	14000-25000	333	...	TNG (NICS)
55771.41	58.41	b200	3300-8700	...	12.0	CA-2.2m (CAFOS)
55771.41	58.41	r200	6300-10500	...	12.0	CA-2.2m (CAFOS)
55780.39	67.39	Grism 4	3200-9100	355	16.2	NOT (ALFOSC)
55780.43	67.43	zJ	8900-15100	700	...	WHT (LIRIS)
55780.40	67.40	HK	14000-23800	700	...	WHT (LIRIS)
55784.40	71.40	b200	3300-8700	...	12.0	CA-2.2m (CAFOS)
55784.40	71.40	r200	6300-10500	...	12.0	CA-2.2m (CAFOS)
55795.39	82.39	b200	3300-8700	...	12.0	CA-2.2m (CAFOS)
55795.39	82.39	r200	6300-10500	...	12.0	CA-2.2m (CAFOS)
55801.37	88.37	IJ	9000-14500	333	...	TNG (NICS)
55801.40	88.40	HK	14000-25000	333	...	TNG (NICS)
55802.37	89.37	gt300	3200-7700	396	12.6	AS-1.22m (AFOSC)
55804.36	91.36	R300B	3200-5300	...	4.1	WHT (ISIS)
55804.36	91.36	R158R	5300-10000	...	7.7	WHT (ISIS)
55812.36	99.36	b200	3300-8700	...	12.0	CA-2.2m (CAFOS)
55812.36	99.36	r200	6300-10500	...	12.0	CA-2.2m (CAFOS)

Table 10. Pseudo-bolometric UV-MIR lightcurve for SN 2011dh calculated from spectroscopic and photometric data. Random errors are given in the first parentheses and systematic lower and upper errors (arising from the distance and extinction) respectively in the second parentheses.

JD (+2400000) (d)	Phase (d)	L (10^{41} erg s^{-1})	JD (+2400000) (d)	Phase (d)	L (10^{41} erg s^{-1})
55717.00	4.00	2.93 (0.01) (0.66,1.24)	55765.00	52.00	5.62 (0.02) (1.20,2.05)
55718.00	5.00	3.63 (0.01) (0.81,1.50)	55766.00	53.00	5.51 (0.02) (1.18,2.01)
55719.00	6.00	4.63 (0.02) (1.03,1.90)	55767.00	54.00	5.39 (0.02) (1.15,1.97)
55720.00	7.00	5.79 (0.02) (1.29,2.37)	55768.00	55.00	5.28 (0.02) (1.13,1.93)
55721.00	8.00	7.02 (0.02) (1.57,2.87)	55769.00	56.00	5.17 (0.02) (1.11,1.89)
55722.00	9.00	8.26 (0.03) (1.84,3.37)	55770.00	57.00	5.07 (0.02) (1.08,1.86)
55723.00	10.00	9.49 (0.03) (2.12,3.86)	55771.00	58.00	4.97 (0.02) (1.06,1.82)
55724.00	11.00	10.66 (0.03) (2.37,4.32)	55772.00	59.00	4.88 (0.02) (1.04,1.79)
55725.00	12.00	11.75 (0.03) (2.61,4.75)	55773.00	60.00	4.78 (0.02) (1.02,1.75)
55726.00	13.00	12.73 (0.03) (2.83,5.13)	55774.00	61.00	4.69 (0.02) (1.00,1.72)
55727.00	14.00	13.62 (0.04) (3.02,5.47)	55775.00	62.00	4.60 (0.02) (0.98,1.69)
55728.00	15.00	14.41 (0.04) (3.19,5.77)	55776.00	63.00	4.51 (0.02) (0.97,1.66)
55729.00	16.00	15.10 (0.04) (3.34,6.04)	55777.00	64.00	4.43 (0.02) (0.95,1.63)
55730.00	17.00	15.75 (0.05) (3.49,6.29)	55778.00	65.00	4.35 (0.02) (0.93,1.60)
55731.00	18.00	16.33 (0.05) (3.61,6.51)	55779.00	66.00	4.26 (0.02) (0.91,1.57)
55732.00	19.00	16.78 (0.06) (3.71,6.67)	55780.00	67.00	4.18 (0.02) (0.90,1.54)
55733.00	20.00	17.06 (0.06) (3.77,6.77)	55781.00	68.00	4.10 (0.02) (0.88,1.51)
55734.00	21.00	17.15 (0.06) (3.78,6.78)	55782.00	69.00	4.02 (0.02) (0.86,1.48)
55735.00	22.00	16.97 (0.08) (3.73,6.68)	55783.00	70.00	3.95 (0.02) (0.85,1.46)
55736.00	23.00	16.53 (0.07) (3.63,6.46)	55784.00	71.00	3.87 (0.02) (0.83,1.43)
55737.00	24.00	15.89 (0.06) (3.48,6.17)	55785.00	72.00	3.80 (0.02) (0.81,1.40)
55738.00	25.00	15.12 (0.05) (3.30,5.83)	55786.00	73.00	3.72 (0.02) (0.80,1.38)
55739.00	26.00	14.27 (0.05) (3.10,5.46)	55787.00	74.00	3.65 (0.02) (0.78,1.35)
55740.00	27.00	13.41 (0.04) (2.91,5.09)	55788.00	75.00	3.58 (0.02) (0.77,1.32)
55741.00	28.00	12.59 (0.04) (2.72,4.75)	55789.00	76.00	3.52 (0.02) (0.75,1.30)
55742.00	29.00	11.84 (0.04) (2.55,4.44)	55790.00	77.00	3.45 (0.02) (0.74,1.28)
55743.00	30.00	11.18 (0.04) (2.41,4.17)	55791.00	78.00	3.38 (0.01) (0.73,1.25)
55744.00	31.00	10.60 (0.03) (2.28,3.94)	55792.00	79.00	3.30 (0.01) (0.71,1.22)
55745.00	32.00	10.10 (0.03) (2.17,3.74)	55793.00	80.00	3.24 (0.01) (0.70,1.20)
55746.00	33.00	9.66 (0.03) (2.07,3.56)	55794.00	81.00	3.17 (0.01) (0.68,1.18)
55747.00	34.00	9.26 (0.03) (1.98,3.41)	55795.00	82.00	3.11 (0.01) (0.67,1.16)
55748.00	35.00	8.91 (0.03) (1.91,3.27)	55796.00	83.00	3.05 (0.01) (0.66,1.13)
55749.00	36.00	8.59 (0.03) (1.84,3.15)	55797.00	84.00	2.99 (0.01) (0.64,1.11)
55750.00	37.00	8.31 (0.03) (1.78,3.04)	55798.00	85.00	2.93 (0.01) (0.63,1.09)
55751.00	38.00	8.05 (0.03) (1.72,2.94)	55799.00	86.00	2.87 (0.01) (0.62,1.07)
55752.00	39.00	7.80 (0.02) (1.67,2.85)	55800.00	87.00	2.81 (0.01) (0.60,1.05)
55753.00	40.00	7.57 (0.02) (1.62,2.77)	55801.00	88.00	2.75 (0.01) (0.59,1.03)
55754.00	41.00	7.35 (0.02) (1.57,2.68)	55802.00	89.00	2.70 (0.01) (0.58,1.01)
55755.00	42.00	7.14 (0.02) (1.52,2.60)	55803.00	90.00	2.64 (0.01) (0.57,0.99)
55756.00	43.00	6.93 (0.02) (1.48,2.53)	55804.00	91.00	2.59 (0.01) (0.56,0.97)
55757.00	44.00	6.74 (0.02) (1.44,2.46)	55805.00	92.00	2.54 (0.01) (0.55,0.95)
55758.00	45.00	6.57 (0.02) (1.40,2.40)	55806.00	93.00	2.49 (0.01) (0.54,0.93)
55759.00	46.00	6.42 (0.02) (1.37,2.34)	55807.00	94.00	2.43 (0.01) (0.53,0.91)
55760.00	47.00	6.27 (0.02) (1.34,2.29)	55808.00	95.00	2.38 (0.01) (0.51,0.89)
55761.00	48.00	6.13 (0.02) (1.31,2.24)	55809.00	96.00	2.33 (0.01) (0.50,0.88)
55762.00	49.00	6.00 (0.02) (1.28,2.19)	55810.00	97.00	2.29 (0.01) (0.49,0.86)
55763.00	50.00	5.87 (0.02) (1.25,2.14)	55811.00	98.00	2.24 (0.01) (0.48,0.84)
55764.00	51.00	5.74 (0.02) (1.23,2.10)	55812.00	99.00	2.20 (0.01) (0.47,0.83)

Table A.1. Mapping of natural systems to standard systems.

Telescope (Instrument)	Natural system	Standard system
NOT (ALFOSC)	Bessel U #7	JC U, SDSS u
NOT (ALFOSC)	Bessel B #74	JC B
NOT (ALFOSC)	Bessel V #75	JC V
NOT (ALFOSC)	Bessel R #76	JC R, SDSS r
NOT (ALFOSC)	Interference i #12	JC I, SDSS i
NOT (ALFOSC)	SDSS g #120	SDSS g
NOT (ALFOSC)	SDSS z #112	SDSS z
LT (RATCam)	Sloan u'	SDSS u, JC U
LT (RATCam)	Sloan g'	SDSS g
LT (RATCam)	Sloan r'	SDSS r, JC R
LT (RATCam)	Sloan i'	SDSS i, JC I
LT (RATCam)	Sloan z'	SDSS z
LT (RATCam)	Bessel B	JC B
LT (RATCam)	Bessel V	JC V
CA (CAFOS)	Johnson U 370/47b	JC U
CA (CAFOS)	Johnson B 451/73	JC B
CA (CAFOS)	Johnson V 534/97b	JC V
CA (CAFOS)	Cousins R 641/158	JC R
CA (CAFOS)	Johnson I 850/150b	JC I
ASIAGO (AFOSC)	Bessel U	JC U
ASIAGO (AFOSC)	Bessel B	JC B
ASIAGO (AFOSC)	Bessel V	JC V
ASIAGO (AFOSC)	Bessel R	JC R
ASIAGO (AFOSC)	Gunn i	JC I
ASIAGO (SCHMIDT)	B	JC B
ASIAGO (SCHMIDT)	V	JC V
ASIAGO (SCHMIDT)	R	JC R
ASIAGO (SCHMIDT)	I	JC I
FTN (FS02)	SDSS G	SDSS g
FTN (FS02)	SDSS R	SDSS r, JC R
FTN (FS02)	SDSS I	SDSS i, JC I
FTN (FS02)	Pann Starrs Z	SDSS z
MONTSEC (CCD)	B	JC B
MONTSEC (CCD)	V	JC V
MONTSEC (CCD)	R	JC R
MONTSEC (CCD)	I	JC I
TNG (LRS)	Johnson U	JC U
TNG (LRS)	Johnson B	JC B
TNG (LRS)	Johnson V	JC V
TNG (LRS)	Cousins R	JC R
TNG (LRS)	Cousins I	JC I
TNG (NICS)	J	2MASS J
TNG (NICS)	H	2MASS H
TNG (NICS)	K	2MASS K
TCS (CAIN)	J	2MASS J
TCS (CAIN)	H	2MASS H
TCS (CAIN)	Kshort	2MASS K
WHT (LIRIS)	j	2MASS J
WHT (LIRIS)	h	2MASS H
WHT (LIRIS)	ks	2MASS K
NOT (NOTCAM)	J	2MASS J
NOT (NOTCAM)	H	2MASS H
NOT (NOTCAM)	Ks	2MASS K
CA (O2000)	J	2MASS J
CA (O2000)	H	2MASS H
CA (O2000)	KS	2MASS K
LBT (LUCIFER)	J	2MASS J
LBT (LUCIFER)	H	2MASS H
LBT (LUCIFER)	Ks	2MASS K

Table A.2. JC *UBVRI* colour terms for all telescope/instrument combinations. Errors are given in parentheses.

CT	NOT (ALFOSC)	LT (RATCam)	FTN (FS02)	CA-2.2m (CAFOS)	AS-Schmidt (SBIG)	AS-1.82m (AFOSC)	TNG (LRS)	TJO (MEIA)
$C_{U,UB}$	0.127 (0.005)	0.018 (0.006)	...	0.186 (0.025)	...	0.179 (0.048)	0.181 (0.020)	...
$C_{U,UR}$	...	0.009 (0.003)	...	0.089 (0.012)	...	...	...	...
$C_{U,UV}$	...	...	...	...	...	0.106 (0.028)	0.107 (0.011)	...
$C_{B,BV}$	0.039 (0.005)	0.059 (0.005)	...	0.135 (0.010)	0.133 (0.041)	0.035 (0.014)	0.071 (0.004)	0.237 (0.016)
$C_{B,UB}$	...	0.039 (0.004)	...	0.095 (0.007)	...	0.024 (0.010)	0.050 (0.006)	...
$C_{B,BR}$	...	...	...	...	0.086 (0.026)	...	...	...
$C_{B,BI}$	...	...	...	...	0.065 (0.020)	...	...	...
$C_{V,BV}$	-0.048 (0.007)	-0.058 (0.006)	...	-0.036 (0.009)	-0.075 (0.043)	0.034 (0.016)	-0.053 (0.009)	-0.038 (0.008)
$C_{V,VR}$	...	-0.103 (0.009)	...	-0.060 (0.016)	-0.083 (0.069)	0.064 (0.029)	-0.096 (0.018)	-0.072 (0.014)
$C_{R,VR}$	-0.064 (0.010)	-0.180 (0.006)	...	0.051 (0.014)	-0.054 (0.050)	0.043 (0.032)	-0.031 (0.015)	-0.061 (0.020)
$C_{R,RI}$	...	-0.183 (0.011)	-0.324 (0.014)	0.043 (0.011)	-0.050 (0.036)	0.048 (0.032)	-0.029 (0.015)	-0.066 (0.020)
$C_{I,VI}$	-0.021 (0.004)	-0.085 (0.006)	...	0.072 (0.020)	0.024 (0.018)	-0.012 (0.015)	0.061 (0.018)	0.041 (0.010)
$C_{I,RI}$	...	-0.168 (0.012)	-0.231 (0.019)	0.128 (0.038)	0.039 (0.031)	-0.021 (0.030)	0.122 (0.034)	0.082 (0.022)
$C_{I,BI}$	...	...	...	...	0.013 (0.011)	...	...	...

Table A.3. SDSS *ugriz* colour terms for all telescope/instrument combinations. Errors are given in parentheses.

CT	NOT (ALFOSC)	LT (RATCam)	FTN (FS02)
$C_{u,ug}$	0.043 (0.027)	0.032 (0.024)	...
$C_{u,ur}$	0.029 (0.018)	0.021 (0.015)	...
$C_{g,gr}$	0.009 (0.011)	0.102 (0.012)	0.200 (0.038)
$C_{g,ug}$	0.007 (0.008)	0.056 (0.010)	...
$C_{r,gr}$	0.077 (0.019)	0.023 (0.016)	0.032 (0.014)
$C_{r,ri}$	0.162 (0.016)	0.057 (0.020)	0.045 (0.014)
$C_{i,ri}$	0.185 (0.027)	0.094 (0.009)	0.045 (0.011)
$C_{i,iz}$	0.310 (0.038)	0.159 (0.015)	0.082 (0.018)
$C_{z,iz}$	-0.094 (0.046)	-0.081 (0.065)	-0.119 (0.023)
$C_{z,rz}$	-0.027 (0.019)	-0.024 (0.028)	...

Table A.4. Synthetic 2MASS *JHK* colour terms for all telescope/instrument combinations.

CT	TNG (NICS)	NOT (NOTCAM)	TCS (CAIN)	LBT (LUCIFER)	WHT (LIRIS)	CA-3.5m (O2000)
$C_{J,JH}$	0.028	0.039	0.026	-0.032	0.056	-0.092
$C_{J,JK}$	0.017	0.024	0.016	-0.020	0.034	-0.055
$C_{H,JH}$	-0.006	-0.008	0.051	0.021	-0.011	0.019
$C_{H,HK}$	-0.008	-0.011	0.077	0.032	-0.016	0.028
$C_{K,JK}$	0.025	-0.005	0.027	0.001	-0.003	-0.007
$C_{K,HK}$	0.062	-0.012	0.067	0.001	-0.007	-0.018

Table A.5. JC *UBVRI* magnitudes of local reference stars used to calibrate the photometry. Errors are given in parentheses.

ID	RA	DEC	U	B	V	R	I
	(h m s)	(° ′ ″)	(mag)	(mag)	(mag)	(mag)	(mag)
P09-1	13 30 14.2	+47 14 55	...	17.01 (0.18)	16.27 (0.03)	15.81 (0.08)	15.44 (0.06)
P09-2	13 30 14.9	+47 10 27	14.62 (0.04)	14.32 (0.02)	13.60 (0.01)	13.19 (0.01)	12.81 (0.01)
P09-3	13 30 21.9	+47 09 05	16.63 (0.01)	16.55 (0.01)	15.92 (0.01)	15.48 (0.01)	15.10 (0.01)
P09-4	13 29 48.5	+47 07 42	16.15 (0.05)	16.23 (0.02)	15.66 (0.02)	15.23 (0.01)	14.91 (0.03)
P09-5	13 29 48.2	+47 08 48	18.88 (0.07)	18.25 (0.07)	17.36 (0.01)	16.75 (0.02)	16.28 (0.01)
P09-6	13 29 43.7	+47 09 14	15.51 (0.02)	15.85 (0.01)	15.39 (0.02)	15.05 (0.01)	14.74 (0.01)
P09-7	13 29 27.9	+47 09 23	17.13 (0.19)	16.73 (0.01)	16.06 (0.02)	15.54 (0.01)	15.10 (0.05)
P09-8	13 29 27.1	+47 10 12	19.76 (0.02)	18.72 (0.05)	17.41 (0.04)	15.82 (0.03)	14.38 (0.03)
P09-9	13 29 29.5	+47 12 03	18.01 (0.23)	16.66 (0.03)	15.68 (0.01)	14.97 (0.01)	14.36 (0.04)
P09-10	13 29 38.6	+47 13 36	16.74 (0.04)	16.20 (0.03)	15.29 (0.01)	14.75 (0.02)	14.20 (0.02)
P09-A	13 29 55.3	+47 10 05	17.77 (0.03)	16.34 (0.01)	15.11 (0.01)	14.33 (0.01)	13.68 (0.01)
P09-B	13 29 45.9	+47 10 47	14.12 (0.02)	14.01 (0.01)	13.43 (0.01)	13.06 (0.01)	12.73 (0.01)
P09-C	13 29 45.9	+47 11 20	17.19 (0.04)	17.15 (0.02)	16.67 (0.01)	16.29 (0.01)	15.94 (0.01)
P09-D	13 29 41.6	+47 11 52	15.76 (0.03)	15.77 (0.01)	15.24 (0.01)	14.85 (0.01)	14.52 (0.01)
E13-1	13 30 13.8	+47 07 30	17.35 (0.01)	16.59 (0.01)	15.70 (0.01)	15.12 (0.01)	14.67 (0.01)
E13-2	13 30 07.6	+47 11 19	17.76 (0.01)	17.26 (0.01)	16.48 (0.01)	16.02 (0.01)	15.63 (0.01)
E13-3	13 30 12.8	+47 10 27	18.94 (0.02)	18.58 (0.01)	17.82 (0.01)	17.29 (0.01)	16.84 (0.01)
E13-4	13 30 04.8	+47 08 05	20.57 (0.03)	19.46 (0.01)	17.99 (0.01)	16.98 (0.01)	15.61 (0.01)
E13-5	13 30 19.9	+47 08 12	19.79 (0.03)	19.17 (0.01)	18.34 (0.01)	17.76 (0.01)	17.31 (0.01)
E13-6	13 30 04.9	+47 09 47	20.98 (0.06)	19.61 (0.01)	18.20 (0.01)	17.28 (0.01)	16.41 (0.01)

Table A.6. SDSS *ugriz* magnitudes for the standard fields PG0231+051, PG1047+003, PG1525-071, PG2331+046 and Mark-A. Errors are given in parentheses.

ID	RA	DEC	u	g	r	i	z
	(h m s)	(° ′ ″)	(mag)	(mag)	(mag)	(mag)	(mag)
PG0231+051E	02 33 28.8	+05 19 48	15.56 (0.01)	...	...	...	13.41 (0.02)
PG0231+051D	02 33 34.0	+05 19 30	17.00 (0.02)	14.59 (0.02)	13.62 (0.01)	13.24 (0.02)	13.04 (0.02)
PG0231+051A	02 33 40.0	+05 17 40	14.63 (0.02)	13.07 (0.02)	12.55 (0.01)	12.39 (0.01)	12.31 (0.02)
PG0231+051	02 33 41.3	+05 18 43	15.36 (0.01)	15.80 (0.02)	16.30 (0.02)	16.61 (0.02)	16.96 (0.02)
PG0231+051B	02 33 45.5	+05 17 33	18.28 (0.02)	15.54 (0.02)	14.16 (0.01)	13.36 (0.01)	12.93 (0.02)
PG0231+051C	02 33 48.1	+05 20 26	15.33 (0.01)	13.97 (0.02)	13.49 (0.01)	13.33 (0.01)	13.29 (0.02)
PG1047+003	10 50 02.8	−00 00 36	...	13.23 (0.02)	13.68 (0.01)	14.06 (0.02)	14.40 (0.03)
PG1047+003A	10 50 05.6	−00 01 10	15.22 (0.01)	13.86 (0.02)	13.32 (0.01)	13.13 (0.01)	13.00 (0.03)
PG1047+003B	10 50 07.9	−00 02 04	16.45 (0.01)	15.02 (0.02)	14.54 (0.02)	14.45 (0.01)	14.36 (0.03)
PG1047+003C	10 50 13.6	−00 00 31	14.04 (0.01)	12.72 (0.02)	12.27 (0.01)	12.14 (0.01)	12.20 (0.03)
PG1525-071	15 28 11.5	−07 16 32	14.44 (0.01)	14.84 (0.01)	15.24 (0.01)	15.56 (0.01)	15.90 (0.01)
PG1525-071D	15 28 12.0	−07 16 39	17.84 (0.03)	16.64 (0.01)	16.12 (0.01)	15.96 (0.01)	15.89 (0.01)
PG1525-071A	15 28 13.4	−07 16 01	15.38 (0.01)	13.88 (0.01)	13.29 (0.01)	13.09 (0.01)	13.01 (0.01)
PG1525-071B	15 28 14.3	−07 16 13	18.01 (0.04)	16.73 (0.01)	16.17 (0.01)	15.98 (0.01)	15.88 (0.01)
PG1525-071C	15 28 16.5	−07 14 30	16.57 (0.02)	14.10 (0.01)	13.20 (0.01)	12.90 (0.01)	12.74 (0.01)
PG2331+055	23 33 44.4	+05 46 39	15.43 (0.02)	15.04 (0.02)	15.30 (0.02)	15.52 (0.02)	15.70 (0.02)
PG2331+055A	23 33 49.3	+05 46 52	14.85 (0.02)	13.36 (0.01)	12.85 (0.01)	12.65 (0.01)	12.56 (0.02)
PG2331+055B	23 33 51.1	+05 45 08	16.79 (0.02)	15.10 (0.02)	14.47 (0.02)	14.21 (0.02)	14.07 (0.02)
MarkA4	20 43 53.5	−10 45 05	16.53 (0.02)	15.14 (0.01)	14.53 (0.01)	14.25 (0.01)	14.10 (0.01)
MarkA2	20 43 54.9	−10 45 31	16.10 (0.01)	14.82 (0.01)	14.37 (0.01)	14.21 (0.01)	14.15 (0.01)
MarkA1	20 43 58.4	−10 47 12	17.26 (0.02)	16.16 (0.01)	15.73 (0.01)	15.57 (0.01)	15.51 (0.01)
MarkA	20 43 59.2	−10 47 41	12.61 (0.01)	12.97 (0.01)	13.47 (0.01)	13.78 (0.01)	14.12 (0.01)
MarkA3	20 44 03.8	−10 45 37	17.20 (0.02)	15.28 (0.01)	14.48 (0.01)	14.17 (0.01)	13.99 (0.01)

Table A.7. SDSS *ugriz* magnitudes of local reference stars used to calibrate the photometry. Errors are given in parentheses.

ID	RA	DEC	u	g	r	i	z
	(h m s)	(° ′ ″)	(mag)	(mag)	(mag)	(mag)	(mag)
P09-1	13 30 14.2	+47 14 55	17.99 (0.02)	16.64 (0.02)	16.09 (0.01)	15.86 (0.02)	15.77 (0.02)
P09-2	13 30 14.9	+47 10 27	15.59 (0.01)	13.96 (0.02)	13.42 (0.01)	13.31 (0.02)	13.21 (0.02)
P09-3	13 30 21.9	+47 09 05	...	16.15 (0.02)	15.69 (0.02)	15.52 (0.01)	15.39 (0.02)
P09-4	13 29 48.5	+47 07 42	17.07 (0.02)	15.90 (0.01)	15.45 (0.01)	15.30 (0.01)	15.25 (0.01)
P09-5	13 29 48.2	+47 08 48	19.33 (0.17)	17.84 (0.02)	17.00 (0.01)	16.71 (0.01)	16.53 (0.02)
P09-6	13 29 43.7	+47 09 14	16.41 (0.01)	15.55 (0.01)	15.24 (0.01)	15.13 (0.01)	15.10 (0.01)
P09-7	13 29 27.9	+47 09 23	...	...	...	...	...
P09-8	13 29 27.1	+47 10 12	...	...	...	...	...
P09-9	13 29 29.5	+47 12 03	...	...	...	...	...
P09-10	13 29 38.6	+47 13 36	...	...	...	...	...
P09-A	13 29 55.3	+47 10 05	18.52 (0.03)	15.86 (0.01)	14.65 (0.01)	14.22 (0.01)	13.99 (0.01)
P09-B	13 29 45.9	+47 10 47	14.95 (0.02)	13.71 (0.01)	13.26 (0.01)	13.15 (0.01)	13.12 (0.01)
P09-C	13 29 45.9	+47 11 20	17.88 (0.11)	16.88 (0.01)	16.48 (0.01)	16.38 (0.01)	16.33 (0.05)
P09-D	13 29 41.6	+47 11 52	16.64 (0.04)	15.49 (0.01)	15.09 (0.01)	14.99 (0.01)	14.95 (0.02)
E13-1	13 30 13.8	+47 07 30	18.03 (0.02)	16.12 (0.02)	15.32 (0.02)	15.08 (0.01)	14.93 (0.02)
E13-2	13 30 07.6	+47 11 19	...	16.86 (0.03)	16.23 (0.03)	16.04 (0.01)	15.96 (0.03)
E13-3	13 30 12.8	+47 10 27	...	18.23 (0.02)	17.53 (0.01)	17.32 (0.04)	17.04 (0.02)
E13-4	13 30 04.8	+47 08 05	...	18.76 (0.02)	17.37 (0.01)	16.27 (0.01)	15.61 (0.01)
E13-5	13 30 19.9	+47 08 12	20.54 (0.06)	18.67 (0.02)	17.95 (0.02)	17.72 (0.02)	17.56 (0.03)
E13-6	13 30 04.9	+47 09 47	...	18.96 (0.03)	17.59 (0.01)	16.90 (0.01)	16.48 (0.02)

Table A.8. 2MASS *JHK* magnitudes of local reference stars used to calibrate the photometry. Errors are given in parentheses.

ID	RA	DEC	J	H	K
	(h m s)	(° ′ ″)	(mag)	(mag)	(mag)
P09-1	13 30 14.3	+47 14 55	14.87 (0.01)	14.43 (0.01)	14.36 (0.01)
P09-2	13 30 14.8	+47 10 27	12.35 (0.01)	12.02 (0.01)	11.96 (0.01)
P09-3	13 30 21.9	+47 09 05	14.55 (0.01)	14.13 (0.01)	14.09 (0.01)
P09-4	13 29 48.5	+47 07 42	14.38 (0.01)	14.04 (0.01)	13.99 (0.01)
P09-5	13 29 48.2	+47 08 48	15.52 (0.01)	14.96 (0.01)	14.87 (0.01)
P09-6	13 29 43.7	+47 09 13	14.28 (0.01)	13.99 (0.01)	13.93 (0.01)
P09-7	13 29 27.8	+47 09 23	14.46 (0.01)	14.00 (0.01)	13.91 (0.01)
P09-8	13 29 27.0	+47 10 10	12.90 (0.01)	12.38 (0.01)	12.12 (0.01)
P09-9	13 29 29.4	+47 12 03	13.52 (0.01)	12.91 (0.01)	12.79 (0.01)
P09-10	13 29 38.6	+47 13 35	13.46 (0.01)	12.93 (0.01)	12.79 (0.01)
P09-A	13 29 55.3	+47 10 04	12.84 (0.01)	12.24 (0.01)	12.12 (0.01)
P09-B	13 29 46.0	+47 10 47	12.25 (0.01)	11.96 (0.01)	11.90 (0.01)
P09-C	13 29 45.9	+47 11 20	15.49 (0.01)	15.16 (0.01)	15.10 (0.01)
P09-D	13 29 41.6	+47 11 52	14.06 (0.01)	13.72 (0.01)	13.66 (0.01)
E13-1	13 30 13.8	+47 07 30	13.96 (0.01)	13.46 (0.01)	13.39 (0.01)
E13-2	13 30 07.7	+47 11 19	15.00 (0.01)	14.59 (0.01)	14.52 (0.01)
E13-3	13 30 12.8	+47 10 26	16.14 (0.01)	15.64 (0.01)	15.56 (0.01)
E13-4	13 30 04.8	+47 08 05	14.30 (0.01)	13.64 (0.01)	13.41 (0.01)
E13-5	13 30 19.9	+47 08 11	16.62 (0.01)	16.09 (0.01)	16.03 (0.01)
E13-6	13 30 04.9	+47 09 47	15.31 (0.01)	14.66 (0.01)	14.48 (0.01)
E13-7	13 29 31.0	+47 08 38	16.54 (0.01)	16.12 (0.03)	16.05 (0.01)
E13-8	13 29 31.8	+47 09 20	17.47 (0.01)	16.85 (0.03)	16.71 (0.03)
E13-9	13 29 33.6	+47 14 03	12.73 (0.01)	12.13 (0.01)	11.89 (0.01)
E13-10	13 29 36.5	+47 06 41	15.31 (0.01)	14.68 (0.01)	14.47 (0.01)
E13-11	13 29 36.9	+47 09 07	11.96 (0.01)	11.39 (0.01)	11.15 (0.01)
E13-12	13 29 39.5	+47 14 30	15.43 (0.01)	14.85 (0.01)	14.58 (0.01)
E13-13	13 29 40.9	+47 10 44	14.22 (0.01)	13.57 (0.01)	13.37 (0.01)
E13-14	13 29 42.3	+47 15 00	17.61 (0.02)	17.07 (0.02)	16.99 (0.01)
E13-15	13 29 44.4	+47 12 32	13.57 (0.01)	13.09 (0.01)	12.80 (0.01)
E13-16	13 29 49.2	+47 14 21	17.19 (0.01)	16.72 (0.03)	16.48 (0.02)
E13-17	13 29 49.3	+47 06 36	15.45 (0.01)	14.78 (0.01)	14.54 (0.01)
E13-18	13 29 50.2	+47 10 28	17.91 (0.01)	17.38 (0.01)	17.21 (0.10)
E13-19	13 29 51.6	+47 14 14	17.28 (0.01)	16.67 (0.01)	16.27 (0.01)
E13-20	13 29 51.6	+47 09 08	17.92 (0.01)	17.34 (0.04)	17.05 (0.02)
E13-21	13 29 54.0	+47 10 57	16.19 (0.01)	15.50 (0.01)	15.37 (0.02)
E13-22	13 29 55.5	+47 13 05	17.88 (0.02)	17.25 (0.01)	17.12 (0.06)
E13-23	13 29 56.2	+47 14 53	16.11 (0.01)	15.73 (0.01)	15.67 (0.01)
E13-24	13 29 57.4	+47 07 44	16.37 (0.01)	15.78 (0.01)	15.55 (0.01)
E13-25	13 29 58.0	+47 04 54	16.84 (0.01)	16.46 (0.02)	16.45 (0.01)
E13-26	13 29 59.7	+47 08 38	17.00 (0.01)	16.40 (0.01)	16.20 (0.03)
E13-27	13 30 01.7	+47 14 30	17.64 (0.02)	17.02 (0.01)	16.84 (0.05)
E13-28	13 30 02.9	+47 07 54	17.19 (0.01)	16.57 (0.01)	16.48 (0.03)
E13-29	13 30 04.3	+47 09 13	17.84 (0.01)	17.37 (0.06)	17.27 (0.03)
E13-30	13 30 04.4	+47 09 50	17.20 (0.01)	16.63 (0.07)	16.38 (0.01)
E13-31	13 30 05.7	+47 15 38	14.70 (0.01)	14.13 (0.01)	13.88 (0.01)
E13-32	13 30 06.1	+47 14 25	17.31 (0.02)	16.68 (0.02)	16.45 (0.02)
E13-33	13 30 07.3	+47 10 01	17.72 (0.02)	17.24 (0.06)	17.12 (0.03)
E13-34	13 30 07.9	+47 05 18	13.67 (0.01)	13.30 (0.01)	13.27 (0.01)
E13-35	13 30 08.0	+47 04 09	17.75 (0.01)	17.13 (0.02)	16.80 (0.04)
E13-36	13 30 10.0	+47 14 21	17.94 (0.07)	17.46 (0.03)	17.21 (0.04)
E13-37	13 30 11.4	+47 05 11	16.04 (0.01)	15.50 (0.01)	15.18 (0.01)

Table A.8. Continued.

ID	RA	DEC	*J*	*H*	*K*
	(h m s)	(° ′ ″)	(mag)	(mag)	(mag)
E13-38	13 30 15.4	+47 11 01	17.68 (0.01)	17.11 (0.04)	16.88 (0.02)
E13-39	13 30 17.4	+47 06 14	15.79 (0.01)	15.16 (0.01)	14.98 (0.01)
E13-40	13 30 18.4	+47 12 14	17.81 (0.03)	17.29 (0.02)	17.04 (0.01)
E13-41	13 30 21.6	+47 10 09	16.41 (0.01)	15.78 (0.01)	15.53 (0.01)
E13-42	13 30 23.1	+47 06 39	16.75 (0.01)	16.12 (0.01)	15.99 (0.01)
E13-43	13 30 26.7	+47 07 26	15.39 (0.01)	14.79 (0.01)	14.57 (0.01)
E13-44	13 30 30.2	+47 12 34	16.34 (0.01)	15.70 (0.01)	15.44 (0.01)
E13-45	13 30 31.8	+47 12 44	17.61 (0.01)	16.99 (0.01)	16.71 (0.06)
E13-46	13 30 33.2	+47 06 39	15.50 (0.01)	14.93 (0.01)	14.67 (0.01)
E13-47	13 30 33.8	+47 14 03	15.78 (0.01)	15.10 (0.01)	15.01 (0.01)
E13-48	13 30 34.8	+47 13 35	16.12 (0.01)	15.72 (0.01)	15.68 (0.03)
E13-49	13 30 34.8	+47 12 29	15.08 (0.01)	14.47 (0.01)	14.26 (0.01)
E13-50	13 30 35.9	+47 07 19	17.98 (0.03)	17.63 (0.04)	17.50 (0.01)
E13-51	13 30 36.6	+47 09 17	15.42 (0.01)	14.80 (0.01)	14.58 (0.01)
E13-52	13 30 39.8	+47 11 19	17.96 (0.01)	17.43 (0.04)	17.21 (0.04)
E13-53	13 30 42.4	+47 10 11	14.71 (0.01)	14.03 (0.01)	13.93 (0.01)
E13-54	13 30 46.2	+47 10 04	16.58 (0.01)	15.96 (0.01)	15.72 (0.03)